SLAC-R-1025

Monte Carlo analysis of the Flavour Changing Neutral Current b \to s gamma at BaBar

by

Daniel Smith

September 2001

SLAC National Accelerator Laboratory, Stanford University, Stanford CA 94309

Work funded in part by DOE Contract DE-AC02-76SF00515

Monte-Carlo analysis of the Flavour Changing Neutral Current b$\rightarrow$ s gamma at BaBar.

D. Smith.

Imperial College of Science Technology and Medicine.

A thesis submitted for the degree of Doctor of Philosophy
at The University of London.

September, 2001

Monte-Carlo analysis of the Flavour Changing Neutral Current b→ s gamma at BaBar.

D. Smith
Imperial College of Science Technology and Medicine.

Submitted for the degree of Doctor of Philosophy
The University of London.
September, 2001

ABSTRACT

The main theme of this thesis is a Monte-Carlo analysis of the rare Flavour Changing Neutral Current (FCNC) decay $b \to s\gamma$. The analysis develops techniques that could be applied to real data, to discriminate between signal and background events in order to make a measurement of the branching ratio of this rare decay using the BaBar detector.

Also included in this thesis is a description of the BaBar detector and the work I have undertaken in the development of the electronic data aquistion system for the Electromagnetic Calorimeter (EMC), a subsystem of the BaBar detector.

To my wife Sandrine.

Acknowledgements

I would like to thank Peter Dornan for inviting me to join the High Energy Physics group as a Ph.D student. I would also like to thank both Jordan Nash and Paul Dauncey for their guidance and their patience.

Contents

List of Figures

List of Tables

Chapter 1

Introduction.

1.1 Prelude.

One thousand years ago a physics PhD student, if such a thing had existed then, would very probably have begun his thesis with a general overview of the state of knowledge at that time, perhaps eluding to the elemental theory which described the basic building blocks of matter in terms of the four "elements", Earth, Wind, Air and Fire. It was then supposed that all matter was composed of varying proportions of these building blocks. One thousand years later after a millennium of scientific endeavour, mankind has painted quite a different picture of the world in which he inhabits; that picture of reality is well known to physicists today as the Standard Model.

1.2 The Standard Model.

The Standard Model [1] is the modern day theory of the fundamental "building blocks" of matter. Within the Standard Model the elementary particles are divided into distinct classes; quarks, leptons, gauge bosons and the Higgs. The Standard Model is concerned with the relationship between these particles and the fundamental forces that cause them to interact.

1.2.1 Forces and Fields.

It is thought that all interactions can be described in terms of the action of forces. The action of all forces can in turn be reduced to the effect of, or the combined effect

of, the fundamental forces of nature; gravity, electromagnetism, the strong force and the weak force. The Standard Model describes the interactions of the elementary particles in terms of the last three. The effects of gravity, although important on macroscopic scales, are negligible in comparison to the effects of the other forces on the elementary particle scale.

The action of the fundamental forces are best understood by considering the forces as the interaction of particles and abstract entities known as fields. Fields were first conceived of by Faraday in an attempt to describe the workings of electric and magnetic forces. The property of a particle that determines whether or not it is affected by a particular field is the particle's "charge". The force exerted on an object in a field depends upon the shape of the field, the position of the particle within the field and the charge of that particle in relation to the field in question.

Particles interacting via the electromagnetic force carry electrical charge, whereas strongly interacting particles carry colour charge. Electrical charges are labelled as positive or negative, like charges repelling each other and unlike charges attracting. Electrical charge is quantized and the charge on the electron is defined to be unity. The strong force is more complicated; colour charge is labelled Red(r), Anti-Red($\overline{r}$), Green(g), Anti-Green($\overline{g}$), Blue(b), Anti-Blue($\overline{b}$). States of rgb or $r\overline{r}$, $b\overline{b}$, $g\overline{g}$ combinations can be colour neutral and are the only observed combinations in nature.

1.2.2 Quarks and Leptons.

Quarks and leptons are the basic constituents of all matter present in the universe. They are distinguished by their properties under the influence of the fundamental forces. The interactions of quarks are mediated by all the known forces of nature, leptons interact gravatationally, weakly and electromagnetically but are immune to the effects of the strong force.

Quarks exist only as bound states of colour neutral pairs and triplets due to the large field strength of the strong force at short distances. The pairs and triplets are known as mesons and baryons respectively. There are six different 'flavours' of

quarks; the up, down, charm, strange, bottom and top, labelled u, d, c, s, b and t respectively. Quarks have fractional electric charge; u, c and t have $+2/3$ while d,s and b have $-1/3$. However bound states of quarks are always of integral charge.

Leptons also differ from quarks in the respect that they have integral rather than fractional charge. There are six types of leptons; the electron, muon, tau, electron neutrino, muon neutrino, and tau neutrino, labelled e, μ, τ, ν_e, ν_μ, ν_τ respectively, where the neutrinos are neutral and the others are of charge -1.

1.2.3 The weak force and parity violation.

The weak force has a unique property that distinguishes it from the other forces of nature, namely that it differentiates between left and right handedness. This phenomenon results in parity violation. Parity is a discrete symmetry which leaves the wave function unchanged by a spatial inversion. Parity violation was first postulated to explain the decays of $K^+ \to 2\pi, 3\pi$. The pion final states have different parity eigenvalues $+1$, -1 respectively. Initially, it was believed that two different types of particle were needed to explain these decays. Experimental verification of parity violation was confirmed through a number of experiments, perhaps the most notable being the study of the beta decay of cobalt 60 [2]. One consequence of parity violation is that right handed neutrinos and left handed anti-neutrinos do not exist in nature.

An example of parity violation is the existence of the process, $\pi^+ \to e^+\nu_{eL}$ and the non-existence of its parity conjugate process $\pi^+ \to e^+\nu_{eR}$.

The weak interaction also violates charge conjugation. Charge conjugation is another discrete symmetry, transforming particles to their antiparticles and vice versa. To take an example, the process $\pi^- \to e^-\overline{\nu}_{eR}$ exists in nature, the charge conjugate process, $\pi^+ \to e^+\nu_{eR}$, does not.

The combined operation of parity and charge conjugation, CP, transforms $\pi^+ \to$

$e^+\nu_{eL}$ to $\pi^- \rightarrow e^-\overline{\nu}_{eR}$, a process that does exist in nature. Although the CP conjugation process exists in the above example, CP has also been shown to be violated in weak interactions.

1.2.4 CP violation and the CKM matrix.

The first evidence of CP violation was also first observed in the kaon system. It was discovered experimentally that the neutral kaons produced in strong interactions decayed with two different lifetimes to two different final states.

$$\tau(K_S^0 \rightarrow 2\pi) = 0.9 \times 10^{-10} sec$$
$$\tau(K_L^0 \rightarrow 3\pi) = 0.5 \times 10^{-7} sec.$$

This phenomenon was initially explained by introducing two different types of neutral kaon, the K_S^0 and the K_L^0. After the discovery of parity violation, these two particles were identified as the admixture states,

$$|K_S^0> = \sqrt{\tfrac{1}{2}}(|K^0> + |\overline{K^0}>)$$
$$|K_L^0> = \sqrt{\tfrac{1}{2}}(|K^0> - |\overline{K^0}>),$$

which allow CP to be conserved. However, in 1964, it was demonstrated that $K_L^0 \rightarrow \pi^+\pi^-$ can occur with a branching ratio of $\sim 10^{-3}$,thus demonstrating CP violation. In the Standard Model, CP violation is encapsulated in the Cabbibo-Kobayashi-Maskawa (CKM) matrix [3]. The CKM matrix is a unitary complex matrix, containing the 3×3 elements that represent the mixing terms that imply CP violation.

1.2.5 Quantum Field Theory (QFT)

The Standard Model is an example of a Quantum Field Theory, where the energy associated with each field is quantized at each point in space-time. The gauge bosons represent the field quanta and can be considered as the mediators of the fundamental forces. There are associated gauge particles for each force: for electromagnetism,

photons; for strong interactions, gluons; for weak interactions, the Z^0, W^+ and W^-. The Standard Model can be subdivided into theories that describe the interactions of individual forces; weak theory, Quantum Electrodynamics (QED), and Quantum Chromodynamics (QCD), all of which are examples of field theories.

The use of symmetries has proved to be a valuable tool in understanding the underlying physics of the Standard Model. A symmetry in nature corresponds to a conservation law and vice-versa. For example, it can be shown that the rotational invariance of a system leads to the conservation of angular momentum and the invariance of the laws of physics in time leads to the conservation of energy. Particular symmetries, namely local gauge symmetries, underpin QFT. A local gauge symmetry describes the situation where there exists an arbitrary phase in the wave function that can be transformed at each point in space-time without affecting the underlying physics.

In order to construct a QFT one proceeds by first choosing a Lagrangian which is both Lorentz invariant and invariant under the operation of a particular gauge symmetry. It turns out that when the requirement of a local gauge symmetry is imposed upon the Lagrangian, one is naturally led to the introduction of interaction terms which describe the underlying force. For example, by choosing the simplest Lagrangian which is both Lorentz invariant and invariant under a U(1) local gauge transformation, one is naturally lead to the equations of electromagnetism. Similarly a SU(3) local gauge symmetry leads to the equations of the strong force. However the weak force does not exhibit local gauge invariance and requires the introduction of electroweak theory and the Higgs mechanism in order to yield to symmetry analysis. Electroweak theory unites the electromagnetic and weak forces, showing that they result from the mixing of two other forces. The electroweak Lagrangian can be combined with that of the strong force to produce the full Standard Model Lagrangian, which transforms according to the symmetry group $SU(3) \times SU(2) \times U(1)$.

1.2.6 Feynman diagrams.

In QFT the interaction cross sections of fundamental processes are calculated using a time ordered perturbation series, each term of which can be pictorially represented

by a Feynman diagram of which figure 1.1 is an example. The simplest diagrams known as "tree level" generally represent the first term in an expansion series and describe the exchange of a virtual gauge boson. More complicated higher order diagrams contain many virtual intermediate states, such as virtual particle loops. Energy and momentum must be the same in the initial and final states and must be conserved at each vertex. However virtual intermediary states can contain loops of infinite momentum.

1.2.7 Renormalization and the Higgs mechanism.

Renormalization is the method by which terms with infinite divergences arising in perturbative corrections containing infinite momentum loops are removed by absorbing them into a redefinition of the particle masses, coupling constants and field normalizations. Without renormalization, the results of calculations beyond the tree level would be rendered meaningless. It can be shown that, in order for a field theory to be renormalizable, it must be gauge invariant [4] and it can also be shown that, in order for a field theory to be gauge invariant, it must have massless gauge particles. In strong and electromagnetic interactions the force mediators, the gluon and the photon, are both massless whereas in weak interactions the three gauge particles, the Z^0, W^+ and W^- are all massive. In order to save the theory of weak interactions the concept of the Higgs field and broken symmetry is introduced. The Higgs particle is postulated as a way of allowing effective masses to be introduced into the theory without destroying the underlying gauge symmetry and therefore allowing the theory to be renormalized.

1.2.8 Successes and failures of the Standard Model.

The Standard Model has been heavily scrutinised but as yet no experiment has been performed that contradicts its predictions. The only aspect of the Standard Model that is not yet experimentally verified is the existence of the elusive Higgs boson which is fundamental to the unification of the electromagnetic and weak forces. This fact does not detract from physicists' faith in the theory as the Standard Model

does not demand that the mass of the Higgs should be within the energies currently probed by experiment. It is expected to have a mass in the range of 110-200 GeV/c^2 [5].

Despite the successes of the Standard Model there are a number of reasons to believe that the Standard Model is an incomplete theory and some way off the mark of being the ultimate theory of everything.

The Standard Model does not predict fundamental parameters such as the particle masses or coupling constants which are crucial for making any predictive calculations within the Standard Model framework. There are a total of 18 independent parameters needed by the Standard Model. These parameters have to be measured experimentally and then "plugged back" into the theory.

Another reason to believe in the inadequacy of the Standard Model is the "gauge hierarchy problem". The gauge hierarchy problem is essentially an issue of renormalisability. The Higgs particle, which ironically was introduced to make electroweak theory renormalizable, has a mass term which is difficult to renormalize. The Higgs mass (m_H) is modified from the bare mass appearing in the Higgs potential by enormous radiative corrections from the virtual effects of all particles that couple directly or indirectly to the Higgs field. For example, a correction from a loop containing a Dirac fermion f with mass m_f to the Higgs mass gives rise to quadratic divergences of the form,

$$\Delta m_H^2 \simeq -\frac{|\lambda_f|^2}{8\pi^2}\Lambda_{UV}^2 \tag{1.1}$$

where λ_f is the coupling term and Λ_{UV} is an ultraviolet momentum cutoff used to regulate the loop integral and is interpreted as the energy scale at which new physics alters the high energy behaviour of the theory. If Λ_{UV} is of the order of the Planck scale, the energy where gravity becomes significant, then corrections to m_H^2 are 30 orders of magnitude greater than the expected $\sim (100GeV)^2$. Setting Λ_{UV} lower

requires the concoction of new physics at that energy. Removing these divergences requires a degree of "fine tuning" that is considered unphysical.

Perhaps the biggest problem with the Standard Model is that the theory of gravity, namely Einstein's theory of General Relativity, is not easily reconcilable with the Standard Model. General Relativity describes gravity in terms of the distortions of space and time in the presence of matter whereas the Standard Model describes forces in terms of Quantum Fields. At the energies at which physicists can probe experimentally, the Standard Model provides an adequate description of the fundamental particles without having to incorporate gravity but at higher energies, where gravity becomes significant, a model that incorporates gravity is a necessity.

1.3 Supersymmetry (SUSY).

There are many theories describing possible new physics beyond the Standard Model, one of the most promising of which is Supersymmetry (SUSY) [6]. There are a number of different competing SUSY models, however they all share the essential ingredient that each fermion has a corresponding boson partner of the same mass. The result is that SUSY models introduce a plethora of new particles,

The squarks (spin 0): $\widetilde{d}_L$, $\widetilde{u}_L$, $\widetilde{s}_L$, $\widetilde{c}_L$, $\widetilde{b}_1$, $\widetilde{t}_1$, $\widetilde{d}_R$, $\widetilde{u}_R$, $\widetilde{s}_R$, $\widetilde{c}_R$, $\widetilde{b}_2$, $\widetilde{t}_2$
The sleptons (spin 0): $\widetilde{e}_L$, $\widetilde{\nu}_{eL}$, $\widetilde{\mu}_L$, $\widetilde{\nu}_{\mu L}$, $\widetilde{\tau}_1$, $\widetilde{\nu}_{\tau 1}$, $\widetilde{e}_R$, $\widetilde{\mu}_R$, $\widetilde{\tau}_2$
The charginos (spin 1/2): $\widetilde{\chi}_1^{\pm}$, $\widetilde{\chi}_2^{\pm}$
The neutralinos (spin 1/2): $\widetilde{\chi}_1^0$, $\widetilde{\chi}_2^0$, $\widetilde{\chi}_3^0$, $\widetilde{\chi}_4^0$
The gluino (spin 1/2): $\widetilde{g}$
Higgs boson: (spin 0): h, H, A, $H^{\pm}$

As there is no present evidence of SUSY particles and since SUSY counterparts of Standard Model particles are required to have the same mass, then if it exists the symmetry must be broken and instead the SUSY masses must be greater than the energies of current particle accelerators.

One of the most attractive features of SUSY theories is that cancellations of the divergences in the Higgs mass perturbation series are an unavoidable consequence of the theory. Loops with fermions and loops with bosons have a relative minus sign and the contributions neatly cancel out. SUSY also paves the way for possibilities of uniting gravity with the other three forces. Grand Unified Theories (GUTs) such as string theories rely crucially on the idea of SUSY.

1.4 Probing beyond the Standard Model.

The Large Hadron Collider under construction at CERN is the most promising location in the next decade to directly discover physics beyond the Standard Model. With a centre of mass energy of 14 TeV the proton, proton interaction can produce particles of masses up to $\simeq 1$ TeV and new particles such as SUSY particles can be searched for directly. The current B physics experiments in operation, such as the BaBar detector at the Stanford Linear Accelerator Center (SLAC), can also indicate physics beyond the Standard Model. BaBar is primarily designed to make precision measurements of elements of the CKM matrix, a task which could itself lead to the discovery of new physics. Other B physics studies such as measurements of some rare B decay can provide hints of theories such as SUSY.

1.5 Introduction to $b \to s\gamma$.

The decay $b \to s\gamma$ is an example of a Flavour Changing Neutral Current (FCNC). FCNCs describe interactions where a quark changes flavour to another quark with the same charge. In the Standard Model FCNCs, such as $b \to s\gamma$, are forbidden at the tree level but are not excluded in higher order interactions. While Flavour Changing Charged Currents do exist through weak interactions at tree level in the form of a W coupling to up and down type quarks from different quark generations, the corresponding neutral current $b \to sZ^0$ does not exist[1]. The simplest example of an allowed $b \to s\gamma$ interaction is the Feynman loop diagram illustrated in figure 1.1, where the b quark transmutes to a s quark via the virtual W and up-type quark

[1]The vector potential associated with the Z^0 meson is diagonalized in flavour space and is therefore invariant under similarity transformations.

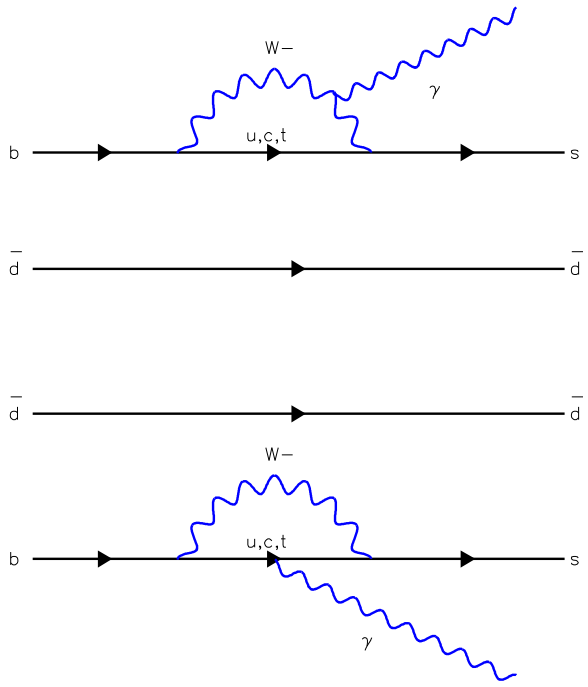

Figure 1.1: Examples of $b \to s\gamma$ Feynman diagrams.

loop. The photon can be radiated from either virtual particle and a gluon can also be exchanged between the quarks.

There has been much theoretical interest in this decay channel as non-Standard Model physics can manifest itself through virtual particles running in the loop.

1.6 SUSY in a FCNC loop.

FCNCs are sensitive to the effects of virtual particles in loops other than Ws and up-type quarks. In fact this is one of the most interesting properties of inclusive $b \to s\gamma$ as the measured branching ratio allows much of the parameter space of SUSY models, in particular the electroweak Radiative breaking Minimal Supersymmetric Model (RMSSM) [6]. There are four different classes of Feynman diagrams corresponding to the four possible RMSSM contributions to $b \to s\gamma$;

A charged Higgs and up-type quark loop

A chargino and up-type squark loop

A neutralino and down-type squark loop

A gluino and down-type squark loop

The possible RMSSM contributions add constructively, enhancing the $b \to s\gamma$ decay rate. $b \to s\gamma$ can also provide indirect evidence for models where two Higgs doublets are present in the scalar field such as the left-right symmetric model[7].

1.7 Theoretical considerations.

In order to make meaningful comparisons between experimental results and Standard Model predictions, theoretical calculations must be reliable and of high enough precision. The nonperturbative nature of b quarks bound in colour neutral hadron states makes such calculations non-trivial. Specific problems require the use of a variety of different techniques available to theorists. The inclusive $b \to s\gamma$ branching ratio is evaluated using the effective operator product expansion technique in conjunction with Renormalization Group Transformations (RGTs). Effective operator product expansions are a means of separating out the processes associated with different energy scales. The effective Hamiltonian for $b \to s\gamma$ is given by

$$H^{eff} = -\frac{4G_f}{\sqrt{2}} V_{tb} V_{ts}^* \sum_{j=1}^{8} C_j(\mu) O_j(\mu) \tag{1.2}$$

where G_f is the Fermi constant coupling, V_{ij} are the CKM matrix elements, $C_j(\mu)$ are the Wilson coefficients[8] evaluated at the scale μ and O_j are the operators that represent the different processes that contribute to the interaction. The Wilson coefficients represent the relevant short distance physics. They are evaluated at the electroweak scale and are evolved down to the scale $\mu \sim m_b$ by RGT[9]. Using this method the inclusive branching ratio of $b \to s\gamma$ has been calculated theoretically to be 3.28×10^{-4}[10].

1.8 $b \to s\gamma$ exclusive measurements.

In a non-resonant $b \to s\gamma$ decay observed as $B \to X_s\gamma$ the product, X_s, is not a single resonant kaon but rather a hadronization containing a kaon and multiple pions, so the mass distribution for X_s is a continuum. When $b \to s\gamma$ is a two body decay, the photon energy for each exclusive mode is a fixed function of the mass of X_s.

All of the exclusive $b \to s\gamma$ modes accessible at BaBar produce a kaon meson reflecting the fact that the B mesons produced at BaBar only contain u, d quarks. To date only the branching ratio of $B \to K^*(892)\gamma$ has been measured. Other exclusive modes have had their branching ratios constrained within limits. $K^*(892)$ is the lightest meson produced as K^0's are inaccessible as they do not conserve angular momentum (see Appendix A). Table 1.1 lists examples of exclusive modes, their theoretical Branching Rations (BR) and their measured limits.

Decay mode	Theoretical BR	Ratio (%)	Measured BR
B $\to K^*(892)\gamma$	$(1.4 - 4.9) \times 10^{-5}$	3.5-12.2	$(4.0 \pm 1.9) \times 10^{-5}$
B $\to K_1(1270)\gamma$	$(4.5 - 10.1) \times 10^{-5}$	1.8-4.0	$< 7.0 \times 10^{-3}$
B $\to K_1(1400)\gamma$	$(6.0 - 13.0) \times 10^{-5}$	2.4-5.2	$< 4.3 \times 10^{-3}$
B $\to K_2^*(1430)\gamma$	$(17.3 - 37.1) \times 10^{-5}$	6.9-14.8	$< 4.0 \times 10^{-4}$
B $\to K_3^*(1780)\gamma$	-	-	$< 7.0 \times 1.0\%$

Table 1.1: Examples of exclusive $b \to s\gamma$ decay modes with limits.[11]

Chapter 2

PEP-II and the BaBar detector.

2.1 Introduction.

The BaBar detector is designed primarily for studies of CP violation in the decays of B mesons. The B mesons are produced by the PEP-II B-factory which is an asymmetric e^+e^- collider. It is expected that BaBar will be able to make measurements of the angles α, β and γ of the unitarity triangle [12] with greater accuracy than previously. Measurements of α are accessible through decays such as $B^0 \rightarrow \pi^+\pi^-$, $B^0 \rightarrow \pi^+\pi^-\pi^0$, $B^0 \rightarrow \alpha_1\pi$, while β is accessible through $B^0 \rightarrow J/\psi {K_S}^0$, $B^0 \rightarrow J/\psi {K_L}^0$, $B^0 \rightarrow J/\psi K^{*0}$, $B^0 \rightarrow D^+D^-$ and $B^0 \rightarrow D^{*+}D^{*-}$. Other studies that BaBar is capable of are general non-CP violating B physics studies, such as rare semi-leptonic decays, physics of charm, tau leptons and two photon physics.

2.2 Measuring CP violation at BaBar.

As the detector design was driven by measurements of CP violation there are many features of the detector that are specific to this aim. This section is motivated to bring the reader's attention to the important implications of CP violating measurements on the detector design.

To first order approximation CP violation can be observed in the channels BaBar

intends to study by the evaluation of equation 2.1.

$$a_{fcp} = \frac{\Gamma(B^0_{phys}(t) \to f_{cp}) - \Gamma(\overline{B}^0_{phys}(t) \to f_{cp})}{\Gamma(B^0_{phys}(t) \to f_{cp}) + \Gamma(\overline{B}^0_{phys}(t) \to f_{cp})} \tag{2.1}$$

Essentially the equation compares the partial decay rates (Γ) of B^0 and $\overline{B}^0$ mesons to the same CP final state (f_{cp}). More specifically the equation requires measurements of the partial decay rates of the B mesons to the same final state, at a time t, after being able to identify (tag) the flavour of the other B meson in the event. Neutral B mesons exist as a time dependent superposition of B^0 and $\overline{B}^0$ states. This added complexity is due to interactions between the B mesons constituent quarks which allow B^0 mesons to transmute into their counterparts. This mechanism is illustrated by means of a Feynman diagram in figure 2.1. The wave function collapses into either a B^0 or $\overline{B}^0$ state at the time of its decay. As the identity of the B meson at its production does not correspond to the identity at the time of decay it is impossible to know precisely the B meson's production identity. Fortunately there are circumstances where a B meson's identity, at a time previous to its decay, can be inferred.

A good source of neutral B mesons is the Υ(4s) (see Appendix B for a description of the Υ resonance sector) which produces neutral B's in a coherent state[1]. The consequence of coherency is that at any particular time the two B meson states are in anti-phase with each other. If the state of one of the B mesons is determined then the other must be in the opposite state. This property can be exploited experimentally on the occasion when one of the Bs decays into a state where there is a signature of its constituent b quark and the other B (denoted B_{phys}) decays as a potential CP violating channel.

For example if one B decays via $B^0 \to \mu^+ \nu_\mu X$, the charge on the μ identifies the B^0 's constituent $\bar{b}$ quark and also identifies the other meson as a $\overline{B}^0$ at that particular moment in time. The B_{phys} can now mix before decaying but crucially to equation

[1]The coherency property of the Υ(4s) is a consequence of the fact that the Υ(4s) is bosonic with J=1.

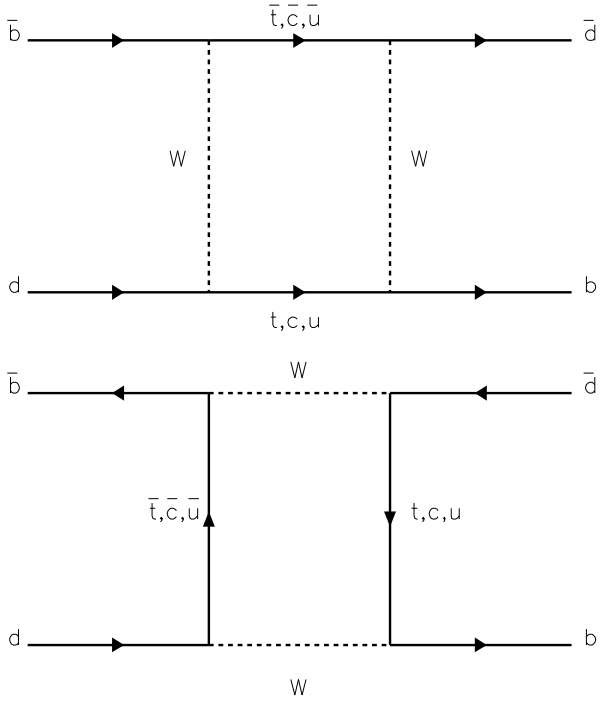

Figure 2.1: Neutral B mixing.

2.1, the decay time after being in a known state, in this example a $\overline{B}^0$ (denoted $\overline{B}^0_{phys}$), can be measured. The sequence of events of a such a decay is illustrated in figure 2.2.

Clearly the time in equation 2.1 is the difference in the decay times between the two B mesons and can be found by measuring the B vertex separation. However due to the short B lifetime $\sim 1.56\times10^{-12}s$ and the small amount of residual energy in the Υ(4s) rest frame, the B's decay vertex separation in the CM frame is too small to make a measurement feasible. In order to increase the vertex separation to

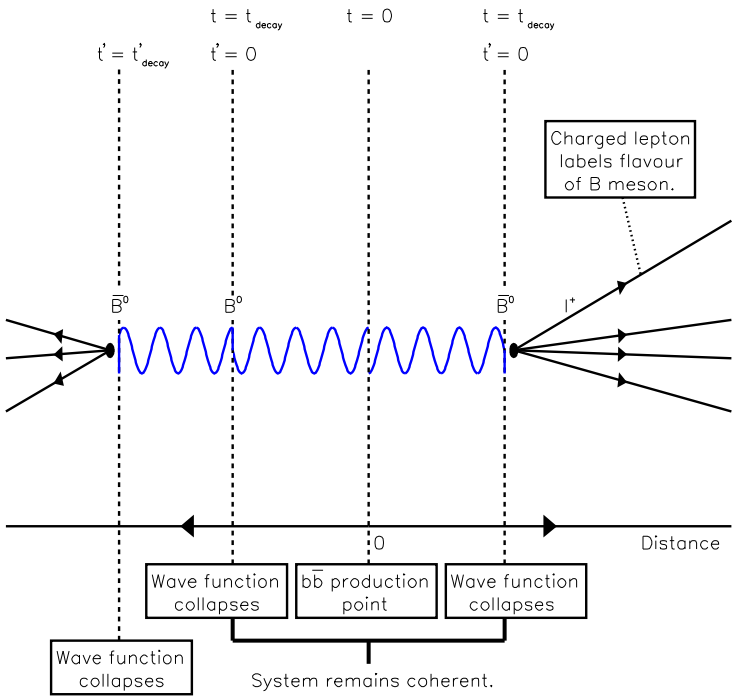

Figure 2.2: Example of neutral B production and decay in the $\Upsilon(4s)$ CM.

a measurable distance, one must apply a boost to the $\Upsilon(4s)$ in the laboratory frame.

In summary, in order to measure CP violation in the B meson system at BaBar a boosted $\Upsilon(4s)$ is used as a source of B's, a means of tagging the charge of primary leptons is needed, and the ability to measure the B decay vertex separation. Further requirements include the ability to reconstuct π^0's which have a high multiplicity in the final states of many of the CP channels and the ability to distinguish between pions and kaons, since kaons are used for tagging and also appear in the final states of some rare B processes.

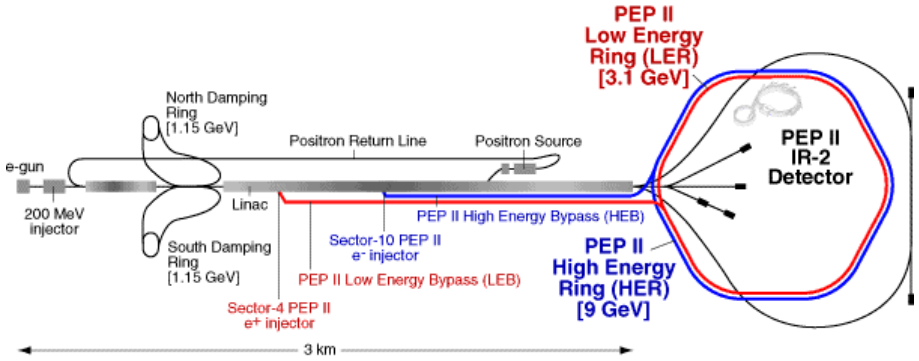

Figure 2.3: PEP-II and the linac at SLAC.

2.3 The PEP-II B-factory.

The PEP-II B-factory[13] is an asymmetric electron, positron collider which collides 9.0 GeV electron and 3.1 GeV positron beams. The centre of mass energy of the beams is 10.58 GeV, the mass of the $\Upsilon(4s)$ resonance. PEP-II operates with an RF frequency of 476 MHz which is an integral fraction of the linac RF frequency. PEP-II is composed of two storage rings, the High Energy Ring (HER) containing the 9 GeV electrons and the Low Energy Ring (LER) containing the 3.1 GeV positrons. A hexagonal tunnel accommodates the two rings which have a circumference of 2200 m and consists of six straight sections connected by six arcs. The LER is held $\simeq$1m vertically above the HER by means of a support structure, except in the Interaction Region (IR) where the two beams collide head on. PEP-II and the linac are illustrated in figure 2.3. The two beams are focussed by a combination of quadropole magnets and are directed and separated from each other at the interaction point by dipole magnets. These are within the detector, but further from the collision point, than the central tracking subsystem. The beams crossing time interval 4.2 ns. Table 2.1 shows the production cross sections at the $\Upsilon(4s)$ CM energy.

The $\Upsilon(4s)$ $(b\bar{b})$ production cross section is 1.05 nb, and the $\Upsilon(4s)$ can decay to $B^0\ \overline{B}^0$ or $B^+\ B^-$ pairs with equal probability. A luminosity of the order of $3{\times}10^{33} cm^{-2} s^{-1}$ is needed to provide the necessary number of B mesons to conduct the CP violation studies within the intended time scales. At this luminosity the total event rate is $\simeq$100 Hz and the physics rate 10 Hz.

$e^+e^- \rightarrow$	Cross-section (nb)
$b\overline{b}$	1.05
$c\overline{c}$	1.30
$s\overline{s}$	0.35
$u\overline{u}$	1.39
$d\overline{d}$	0.35
$\tau^+\tau^-$	0.94
$\mu^+\mu^-$	1.16
e^+e^-	40

Table 2.1: Cross section at the Υ(4s) resonance.

The storage rings are topped up once per hour in a period of approximately three minutes. The electrons and positrons are injected into the storage rings by a 3 km long linac. The electrons are initially produced by an electron gun and injected into the linac. Damping rings are used to collimate the beams and a series of klystrons generate the 2856 MHz RF wave accelerating the particles. The electrons and positrons are extracted at different lengths of the linac at points corresponding to the required energies of the beams. The positrons are created by directing accelerated electrons at a tungsten target, the electrons emit bremsstrahlung radiation in the tungsten material which in turn produce e^+ e^- pairs. The positrons are extracted by means of a magnetic field and returned to the positron return line.

There are three sources of machine background: synchrotron radiation photons produced in the machine elements, off-energy electrons and photons produced in bremsstrahlung interactions with background gas molecules and electrons that have been elastically scattered in interactions with background gas molecules. The IR has been designed to reduce the effects of these backgrounds and ensures that most of the synchrotron radiation which would enter the detector is absorbed by the collimators.

2.4 The BaBar detector.

The BaBar detector [14] is composed of 5 distinct subsystems which make up concen-

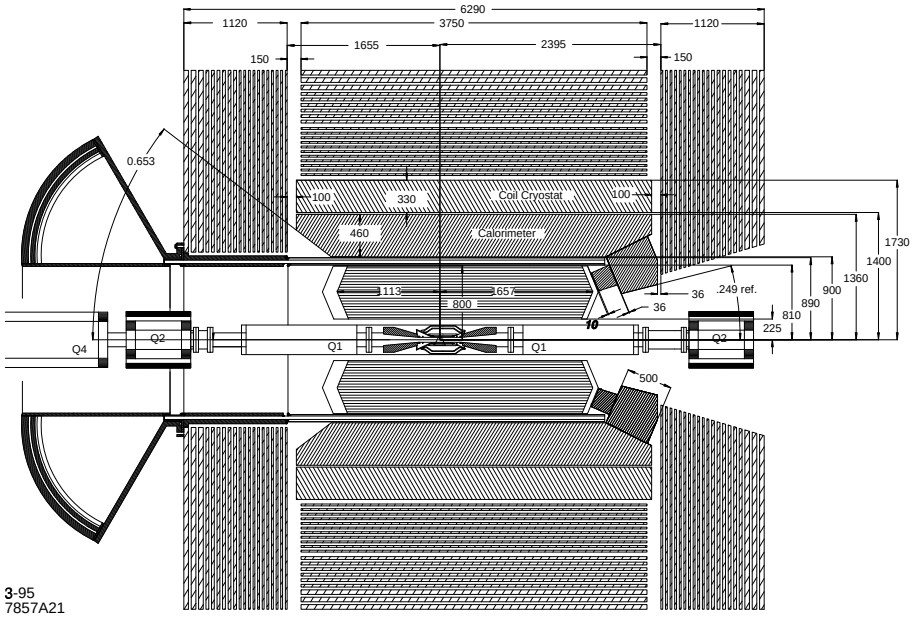

Figure 2.4: BaBar Detector.

tric layers about the beam pipe. Each of the subsystem design specifications have CP violating studies in mind and play crucial roles in reconstructing the physics events produced. The BaBar detector is illustrated in figure 2.4.

Moving radially outwards from the centre of the detector, the first subsystem is the Silicon Vertex Tracker (SVT). The SVT is used primarily for vertex determination but also provides tracking for charged particles with momentum less than 100 MeV/c. The Drift CHamber (DCH) is necessary for the tracking of charged particles and capable of giving some particle identification. The DIRC (Detector of Internally Reflected Cherenkov light) has the sole purpose of particle identification. The ElectroMagnetic Calorimeter (EMC) measures the electromagnetic energy and spatial location of particles. Finally the Instrumented Flux Return (IFR) is a muon and neutral hadron detector. The superconducting solenoid which provides a 1.5 T magnetic field is situated inside the IFR.

2.5 The Silicon Vertex Tracker (SVT)

The SVT has the dual purpose of measurement of vertex separation and providing tracking for particles with a low transverse momentum ($\sim$100 MeV/c and less).

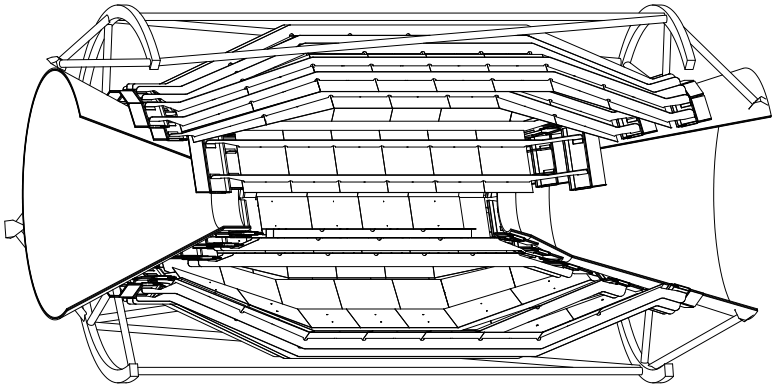

Figure 2.5: Silicon Vertex detector.

The goals of the CP violating physics studies require that the detector vertex resolution must be better than half the mean vertex separation, an average of $\sim$250μm, corresponding to a single vertex resolution of better than 80μm. This degree of vertex resolution contributes no more than a 10% loss in precision in the CP asymmetry measurements.

Meeting the tracking criteria enables the SVT to measure the tracks of charged particles not energetic enough to reach the Drift Chamber (DCH). It also complements the tracking information from the DCH for particles of higher momentum, especially in the region up to 180 MeV/c where the drift chamber has not yet reached its full efficiency.

The SVT is composed of 5 layers of double sided microstrip detectors as illustrated in figure 2.5. Three inner layers are in a barrel-like structure and divided into six detector modules. Each of the two outer layers forms a novel arch structure, the layers are divided into 16 and 18 detector modules respectively. The arch both increases the solid angle coverage and reduces the track incidence angles. The modules in the outer layers alternate between two slightly different radii to allow them to overlap. The double sided detector strips have a stereo angle of 90 degrees. The strips facing on to the detector are perpendicular to the beam direction and measure the position in z, whereas the strips facing outwards measure the position in ϕ.

The SVT's resolution is slightly better than the CP physics requirements, aiding in vertex reconstruction, background rejection and pattern recognition. The inner layers achieve resolutions of 10-15 μm, whereas the outer layers achieve resolutions of the order of 30-40 μm. However the uncertainty caused by multiple scattering dominates over these resolutions. The SVT covers a polar angle of $20.1° \leq \theta \leq 150.2°$. The coverage in the forward direction is maximized by keeping components such as the cooling systems, cabling and the readout electronics for the ~150,000 different channels to the backward region. The solid angle coverage is limited by the beam bending magnets at 17.2° in the forward and backward directions.

2.6 The Drift CHamber (DCH).

The DCH is primarily used for tracking but is also important for particle identification and is used alongside the EMC for the input of the Level 1 trigger.

The DCH must provide spatial resolutions averaged in the R-ϕ plane of better

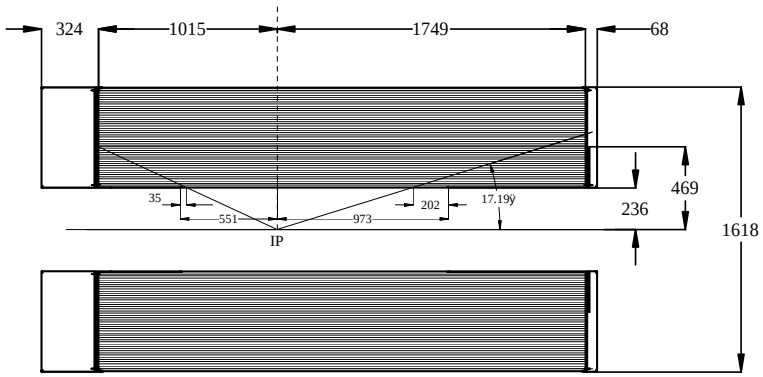

Figure 2.6: Drift chamber side view.

than 140μm in order to obtain the required momentum resolution. It also allows reconstruction of secondary vertices within the the DCH volume. The DCH solid angle must cover the polar angle range down to 300mr (the beam pipe); anything less would result in an extremely unsatisfactory B reconstruction efficiency due to missing tracks. The DCH also provides particle identification at a resolution of 7% for low momentum dE/dx tracks, allowing π/K separation up to 700 MeV/c. This

particle identification complements the DIRC in the barrel region and is extremely useful for tracks in the extreme backward region where the DIRC offers no information. The side view of the DCH is illustrated with dimensions in figure 2.6.

The DCH is filled with a helium-isobutane gas mixture (80%:20%). The gas was chosen for properties that include low multiple scattering, good spatial and dE/dx resolution and reasonably short drift time. A short drift time is important to eliminate dead time and for that same reason a small-cell cylindrical chamber design was chosen. The drift cells are hexagonal, arranged in a series of concentric layers. In the middle of each cell is a sense wire held at a voltage of $\sim 1270V$, while the wires at the points of the hexagon are field wires held at $0V$. There are 40 layers, 10 superlayers of 4 layers each. The super layers are arranged in an axial, stereo combination, A, U, V, A etc. In the axial superlayer the wires run parallel to the z direction, while in the stereo super layers the wires are at angles, alternating in direction for U and V. The stereo wires vary from an angle of 40 mrad in the innermost layers to a maximum angle of 70 mrad in the outermost layer. The order of the layers is illustrated in figure 2.7.

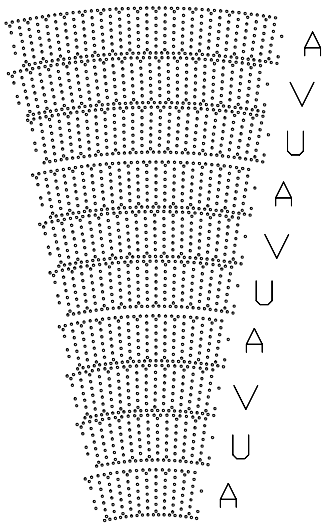

Figure 2.7: Drift chamber cell layout.

2.7 Detection of Internally Reflected Cherenkov light (DIRC)

The DIRC is a particle identification device used for π/K separation and also for muon identification (typically below $\sim$750 MeV/c). The DIRC is designed to pro-

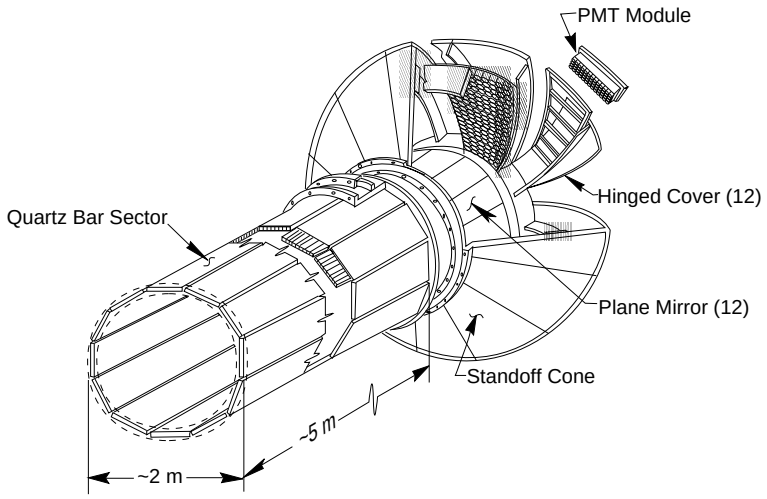

Figure 2.8: DIRC.

vide identification for kaons of momentum up to $\sim$2.0 GeV/c for tagging purposes, and also for higher momentum kaons to study rare B meson decays.

The DIRC is composed of 12 sheets of quartz crystal machined into strips. The strips form a 12 sided barrel between the DCH and the EMC. Particles that traverse the bar with velocities greater than the speed of light in that medium radiate Cherenkov light, which is totally internally reflected inside the bars. At the rear of the detector there is a stand off box which allows the rays to separate. The Cherenkov pattern is detected by an array of photomultiplier tubes at the rear of the stand off box. The stand off box is filled with water which has a similar refractive index to that of quartz and therefore reduces total internal reflection at the quartz, water junction. Only the rear end of the quartz is instrumented, mirrors at the front end of the quartz bars reflect rays traveling in the forward direction. The DIRC is illustrated in figure 2.8.

The DIRC has an acceptance of 87% of the solid polar angle in the CM frame and 93% in the azimuthal solid angle, the missing 7% is due to gaps in the bars. The threshold transverse momentum to reach the DIRC is $\sim$250 MeV/c. The DIRC particle hypothesis is 95% of the time correctly consistent with being a kaon, from the Cherenkov threshold $\sim$460 MeV/c right up until $\sim$4 GeV/c where the efficiency drops to 90%. The DIRCs hypothesis is correctly consistent with being a muon 80% of the time below 750 MeV/c and 95% of the time at 500 MeV/c.

2.8 The ElectroMagnetic Calorimeter(EMC)

The fundamental role of the EMC is to measure the electromagnetic energy deposited in each event but it is also used to provide some particle identification and also as an input to the Level 1 trigger.

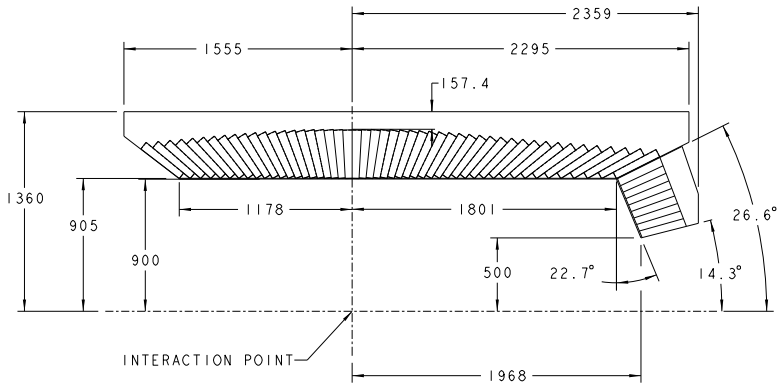

Figure 2.9: Electromagnetic Calorimeter barrel crystal arrangement.

Many of the channels of interest for CP violating studies contain neutral pions in their final state, for example J/ψ K^0_S, J/ψ K^{*0}, $D^{*+}D^{*-}$, $\rho^{\pm}\pi^{\pm}$. The efficiency of reconstruction of the exclusive B mass is very sensitive to the resolution of π^0 reconstruction. The calorimeter needs to have good energy resolution over a wide energy range, it should be able to reconstruct energies from 20 MeV up to about 5 GeV as decay modes such as $B^0 \to \rho^{\pm}\pi^{\pm}, \rho^{\pm} \to \pi^{\pm}\pi^0$ have π^0s with momentum that varies up to $\sim$2.5 GeV in the CM. The EMC is also used for tagging by separating e/π and e/μ.

The EMC is a scintillation calorimeter constructed from 6580 thallium doped CsI scintillating crystals held in a carbon fibre structure. The EMC consists of two distinct sections, the barrel and forward end cap. There are 5760 crystals in the barrel, 48 rings of 120 crystals, there are 820 crystals in the endcap arranged in 8 rings. The crystals vary in size across the detector. In the backward half of the barrel the size is constant 16.1 X_0 (29.76 cm), at the front of the barrel crystal lengths increase in 0.5 X_0 steps per 7 crystals up to 17.6 X_0(32.55 cm). In the end cap the crystals have a constant length of 32.55cm except for the two innermost rings where space limitations force the length to be reduced by 1 X_0. The crystal arrangement in the barrel is illustrated in figure 2.9. The scintillation light produced is read out by two photodiodes mounted directly on the rear face of each crystal. The Molière radius[2] of an electromagnetic shower in CsI is 3.8 cm, whereas the crystal faces have typical dimensions of 4.7 x 4.7 cm, hence the electromagnetic energy is never deposited in a single crystal but rather clusters of crystals.

The calorimeter covers a solid angle in the laboratory frame of $-0.775 \leq \cos\theta \leq 0.962$ corresponding to a solid angle coverage of $-0.916 \leq \cos\theta \leq 0.895$ in the centre of mass frame. The target energy resolution for a polar angle of 90° is given by equation 2.2.

$$\frac{\sigma_E}{E} = \frac{1\%}{\sqrt[4]{E(GeV)}} \oplus 1.2\% \tag{2.2}$$

The constant term includes front and rear leakage, inter-calibration errors and light collection uniformity. The $E^{\frac{1}{4}}$ energy dependence is a parametrization of various effects but is dominated by shower leakage. The equation does not include electronic noise.

The target angular resolution is given by equation 2.3 and is dependent on the

[2]The Moliere radius is defined as the average lateral deflection of critical energy electrons after a traversal of one radiation length and is parametrized as, $R_m = \frac{21_{MeV} X_0}{\epsilon} \simeq \frac{7A}{Z} g.cm^{-2}$, where ϵ is the critical energy, the energy at which the energy loss due to ionization and radiation are equal.

average distance to the interaction point and the transverse crystal size.

$$\sigma_\theta = \frac{3mr}{\sqrt[2]{E(GeV)}} \oplus 2mr \tag{2.3}$$

2.9 The Instrumented Flux Return (IFR)

The IFR is the outermost subdetector in BaBar. Its purpose is to provide muon

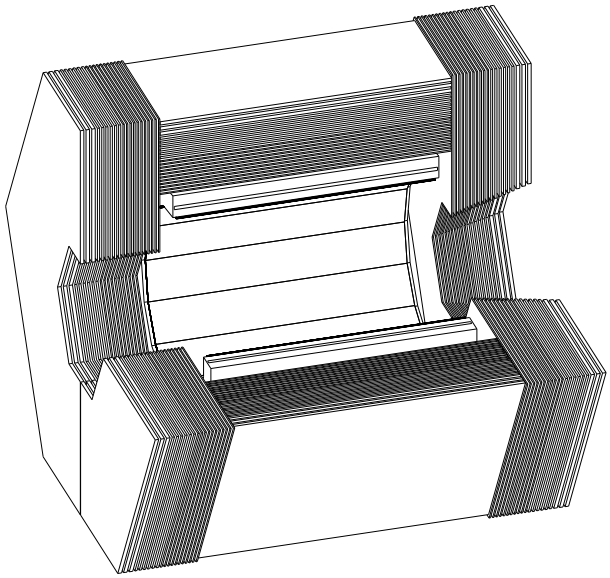

Figure 2.10: Instrument Flux Return barrel.

identification and neutral hadron detection. Muon identification is primarily important for tagging the flavour of the b quark in CP violating studies. Neutral B mesons decay to a state containing a lepton $\simeq 30\%$ of the time, either an electron, muon or tau. Taus decay immediately, only electrons and muons traverse the detector. The majority of electrons are absorbed in the EMC, radiating their energy via bremsstrahlung processes. Muons on the other hand, due to their increased mass, are not significantly effected by this process and penetrate the EMC. Muons from the secondary decay of D mesons can also be used to identify the flavour of the c quark. For these reasons the IFR does not need to provide good energy resolution

but rather just detect the particles and provide some postition information.

The IFR is comprised of a barrel and forward and backward end caps. The IFR forms a large hexagonal iron structure and doubles as a magnet yoke for the superconducting solenoid. The iron structure is segmented and instrumented with Resistive Plate Counters (RPC). The iron segments are graded and vary in thickness from 2 to 10cm, increasing with radial distance from the interaction region. The grading of the iron segments improves the performance of the subdetector without increasing the number of layers. Both low momentum muon identification and K_L^0 detection are benefited by this scheme. The IFR is illustrated in figure 2.10.

There are 18 iron segments in the barrel and a total of 21 active detector layers; 17 RPC layers sandwiched between the iron segments, 1 layer on the outer side of the iron structure, 1 layer between the innermost iron segment and the solenoid coil and 2 cylindrical RPC layers surrounding the EMC. The number of RPC modules in the barrel totals 364. Each cylindrical layer is split into 4 RPC chambers containing 4 RPC modules, while each layer of the IFR barrel has 6 RPC chambers, one chamber per sextant, divided up into 3 RPC modules. In each end cap there are 18 detector layers, each layer contains 6 RPC modules, therefore the number of RPCs in both end caps totals a further 216.

The RPCs use a gas mixture of Argon and Freon in roughly equal proportions, plus a small percentage of Isobutane. The RPCs operate in streamer mode. The RPC are read out by aluminium electrodes that run along the chamber lengthwise and crosswise to produce 3 dimensional information.

2.10 The Trigger System.

The trigger system is not a subsystem in its own right but is an important component of the BaBar detector, designed to select the physics events of interest. The trigger operation is divided into two levels, the Level 1 trigger which operates at the hardware level and the Level 3 trigger which is purely software and executes after

the event assembly.

For asymmetry measurements and searches it is important to select events with a high efficiency whereas for branching ratio and cross section measurements precisely measured efficiencies are important. Therefore the BaBar trigger must be both efficient and have well known efficiencies. The BaBar trigger is 99.0 ± 0.5% efficient for selecting $B\overline{B}$ events that are both CP and non-CP violating. It also has high efficiencies for continuum $q\overline{q}$, τ and $\gamma\gamma$ events, where the efficiencies are precisely known. It also has high efficiency for Bhabhas which are used as a means of measuring the beam luminosity and for calibration.

The Level 1 Trigger is composed of three parts: the DCH trigger, the EMC trigger and the global trigger. The EMC trigger requires a minimum of 2 energy clusters with energy deposits above a threshold efficient for muons. The DCH trigger needs a minimum of 2 charged tracks, with $p_t > 0.18\ GeV/c$ and $p_t > 0.12\ GeV/c$. The global trigger combines the DCH and EMC trigger data to make a final Level 1 trigger decision. If the event is accepted the trigger issues a Level 1 accept command via the Data Acquisition system. The trigger output rate is constrained to a maximum of 2 kHz as the bandwidth of the Data Acquisition system is limited; the actual rate is ∼800 Hz. The trigger latency, the time between the beam crossing and a Level 1 Accept to reach the front end electronics, is 12 μs with a jitter of no more than 1.008 μs.

The Level 3 trigger algorithms use several strategies to discriminate background from physics events and provides a further background rejection ratio of 1:20 reducing the event rate to within 100 Hz , the maximum logging rate for writing events to mass storage.

2.11 $b \to s\gamma$ inclusive measurements.

To date there have been two independent inclusive measurements of the $b \to s\gamma$ branching ratio, made at CLEO[15] and at ALEPH[16]. The CLEO and ALEPH

measurements are in close agreement with each other and the Standard Model prediction. ALEPH measured a branching ratio of $(3.14 \pm 0.83 \pm 0.53) \times 10^{-4}$ and CLEO's latest figure is $(3.15 \pm 0.35 \pm 0.32 \pm 0.26) \times 10^{-4}$, where the first error is statistical, the second is systematic and the third arises due to model dependency.

2.11.1 ALEPH measurement.

The ALEPH measurement is made in an experimental environment very different to that of BaBar, the most fundamental difference being that LEP-I was at a much higher energy than PEP-II, producing Z^0s in the CM with beam energies of $\sim$46 GeV. The consequence is that B mesons are produced in the hadronization of $b\bar{b}$ jets have to be distinguished from the other hadronization products. Another important differing factor, due to the higher energy, is that B_s mesons can be produced at ALEPH, which results in additional $b \to s\gamma$ modes such as $B_s \to \phi\gamma$ or $B_s \to f_2'(1525)\gamma$.

2.11.2 CLEO measurement.

The experimental environment at CLEO is not too dissimilar to that of BaBar. The two experiments both generate B mesons by producing $\Upsilon(4s)$ resonances from electron, positron annihilation. The detectors are also not too dissimilar. The major differences are that at CLEO the $\Upsilon(4s)$ resonances are produced in the CM frame whereas BaBar produces them with a boost in the laboratory frame. Also CLEO uses a time of flight system for particle identification while BaBar uses the DIRC. The luminosity at BaBar is also greater than at CLEO.

2.12 Measuring inclusive $b \to s\gamma$ at BaBar.

A measurement of $b \to s\gamma$ at BaBar not only provides a useful third independent measurement but it also could potentially provide a more accurate one. Comparing BaBar with the CLEO detector, one can imagine that the boost at BaBar makes

matters slightly more complicated, but on the positive side the DIRC at BaBar gives improved kaon, pion discrimination and because of the higher luminosity, BaBar should eventually accumulate a larger data sample of both on-resonance and off-resonance data than CLEO's lifespan allows. Additional on-resonance data reduces the statistical error, while additional off-resonance data improves the systematic errors that arise as a consequence of background subtraction.

Chapter 3

Calibration of the EMC Front End Electronics.

3.1 Introduction

The main theme of this thesis is the Monte Carlo analysis of a $b \to s\gamma$ measurement. However in this chapter I will take a minor detour in order to highlight another aspect of the work I have undertaken as a PhD candidate, namely involvement in the development of the EMC Front End Electronics (FEE). Specifically my work has been in the testing of different prototype stages of the electronics, the installation and testing of the final electronics and the electronic calibration.

In this chapter I will give a detailed description of the function of the EMC electronics, an overview of the BaBar Data Aquisition (DAQ) system and the presentation of the procedure and results of the electronic calibration method that I have attempted.

3.2 The design requirements of the EMC Electronics.

The design requirements of the EMC electronics are as follows:

• The EMC electronics are required to read out energy deposits in a single crystal in the range from 50 keV up to 13 GeV. At the low end of the energy scale this

specification allows for the energy peak from a 6 MeV calibration source to be measured. At the high end of the energy scale, the maximum energy Bhabhas produced at the $\Upsilon(5S)$ energy can be accomodated. The minimum amount of dynamic range that allows these aims to be achieved is 16 bits with the Least Significant Bit (LSB) representing 50 keV. However 18 bits are needed to provide an additional safety factor.

• The EMC energy resolution should be such that for any photon deposited with energy greater than 20 MeV, the total electronic contribution to the energy resolution is less than the intrinsic resolution of the CsI crystals in conditions up to twice nominally expected background. The most dominant effects of the electronics on the overall energy resolution of the EMC are incoherent noise, digitization noise and the signal shaping time. The shaping time can influence the resolution considerably; as background photons are the dominant source of noise, a short shaping time reduces the time interval for an extraneous photon to affect the crystal readout, significantly improving the overall energy resolution; on the negative side a short shaping time also causes an increase in the incoherent noise contribution. The effect of the digitization noise is specifically required to be less than half that of the CsI contribution.

• The FEEs must include a calibration system that allows non-linearities introduced by the electronics to be corrected to the accuracy of the LSB of the digitization. The system should be such that the calibrations can be undertaken frequently enough to correct any time dependent drifts in the electronics.

• As one of the two input sources to the Level 1 trigger, the electronics must also provide a trigger interface. The trigger requires cluster energy sums and these sums must be calculated for each sample by the electronics.

• The FEEs must also integrate into the BaBar DAQ framework. The data rate must be within the DAQ system limits and the FEEs must adhere to the protocols set down by the DAQ group.

It is these design requirements along with budget requirements that motivated the design of the EMC's electronic DAQ system.

3.3 Overview of the BaBar Data Aquisition (DAQ) system.

The BaBar DAQ system [17], is responsible for the readout of the Front End Electronics, the distribution of the trigger, event gathering and timing distribution, The system consists of a networked set of electronics crates, electronic modules and workstations. Figure 3.1 illustrates the IR-2[1] DAQ platform.

The IR-2 platform is comprised of a single Master crate and multiple Slave crates.

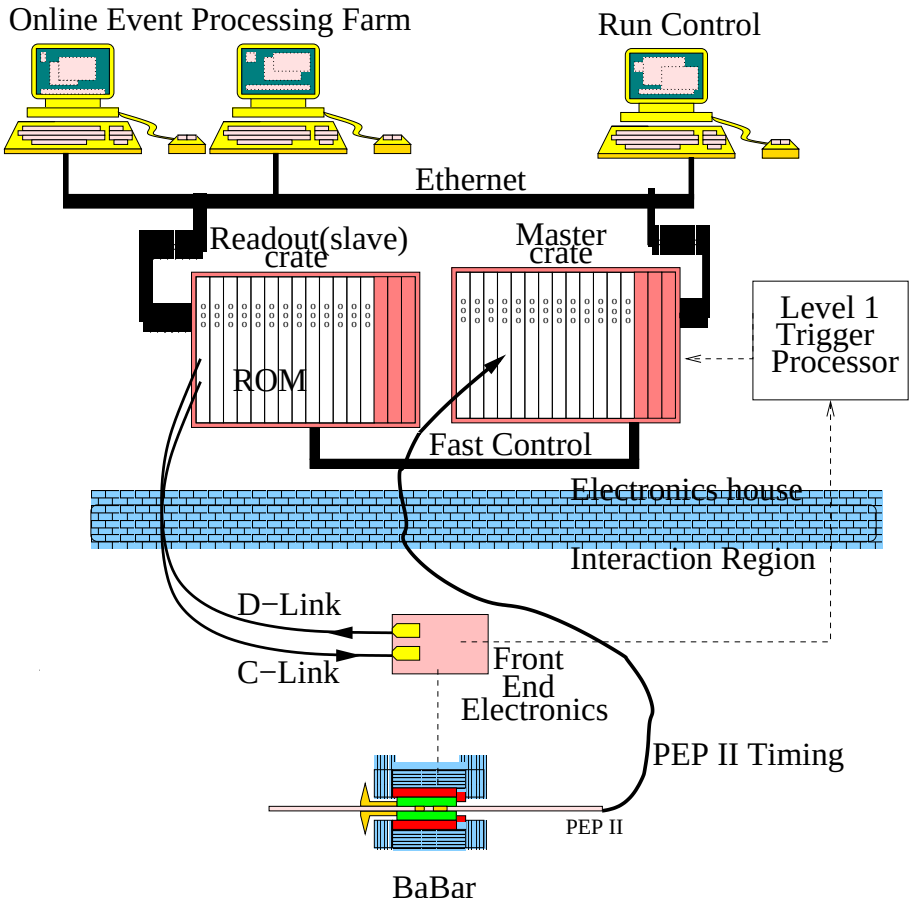

Figure 3.1: BaBar Data Aquisition System.

[1]IR-2 is the name of the BaBar interaction region.

The FEEs communicate, via optical fibres, with Read-Out Modules (ROMs) residing in Slave crates in the electronics house. The ROMs accumulate data on receipt of a Level 1 trigger signal, which is distributed via the Fast Control and Timing System (FCTS). The ROMs perform some inital data processing before passing the data through ethernet to the Online Event Processing Farm, where the Level 3 trigger is applied, online event processing and event gathering. The Run Control provides an interface to the processes executed on each ROM and allows the DAQ platform to be repartitioned.

3.3.1 Electronics crates.

The electronics crates are 9U VME with a custom J3 backplane. The crates can be populated with up to 21 electronics modules. Certain types of modules are constrained to specific slots within the crates. The crates act in either of two distinct roles, as a Master Crate or as a Slave Crate, the nomenclature indicating the relationship between the two. The function of each crate is dependent upon the type of modules it is configured with.

The function of the Master Crate is to act as the point from which the commands and central timing of the DAQ system are distributed. The Master crate houses a set of Fast Control and Timing System (FCTS) modules which allow the simultaneous control of multiple Slave crates in a single platform. The crate also contains a Fast Control Timing Module (FCTM) that interfaces BaBar to PEP-II. The FCTM receives luminosity, "sysclk" and subfiducial signals from PEP-II. The frequency of the luminosity signal is proportional to the beam luminosity which enables dead time calculations to be performed. The BaBar system clock, known as the "sysclk", has a frequency of 59.5 MHz which is derived from the 476 MHz RF clock of PEP-II. The subfiducial is derived from every second fiducial, where the fiducial marks "bunch zero" in the machine.

A Slave Crate houses the electronics modules used to retrieve the data from the FEEs. A slave crate is configured with a Fast Control Distribution Module (FCDM) and up to 17 ROMs. Further electronics modules can be accomodated that allow

the Slave Crate to act independently of the Master Crate. The FCDM is used to distribute common timing and control systems to the ROMs within the crate. The ROMs manage the FEEs, communicating to the FEEs and buffering the data they receive from them. The slot 1 ROM is responsible for accumulating the data from the ROMs within the crate and passing it on to the bulk data processing systems.

3.3.2 Read-Out Modules (ROMs).

A ROM is responsible for the management and accumulation of data from the FEEs.

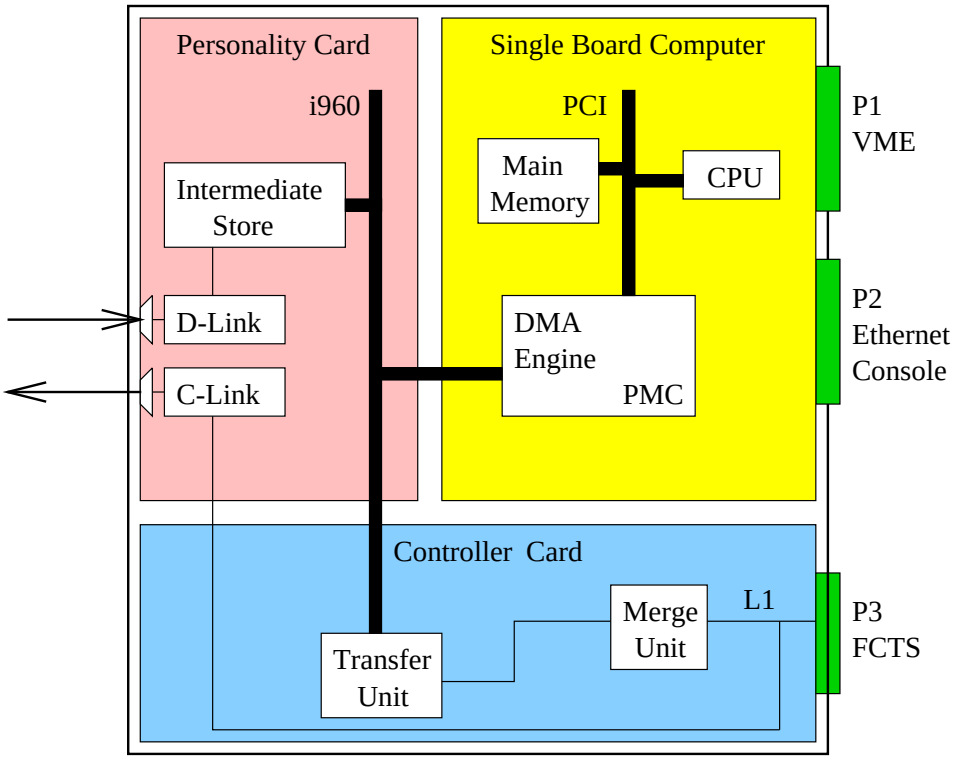

Figure 3.2: Triggered Readout Module.

The ROMs are also responsible for "feature extraction", meaning the operation of extraction, transformation or reduction of the gathered data.

The ROMs are composed of a front panel and 3 distinct electronic cards, a Controller Card (CC), a Single Board Computer (SBC) and a Personality Card (PC).

- The CC receives the sysclk and command packets, and on the receipt of a trigger

Level 1 Accept command, initiates and directs the collection of event data.

• The SBC houses a general purpose processor running the VxWorks real time operating system and allows different algorithms to be loaded and executed on the ROM.

• The PC can be either of two flavours: a Triggered Personality Card (TPC) or an Untriggered Personality Card (UPC). ROMs containing a TPC or a UPC are known as Triggered or Untriggered respectively. A functional diagram of a triggered ROM is illustrated in Figure 3.2. The principle difference between the two cards is that the TPC extracts data from the FEEs only upon the receipt of a Level 1 Accept command, while the UPC continuously buffers the data from the FEEs and extracts the relevant data on a L1 Accept.

The triggered ROMs communicate with the FEEs using a BaBar standard protocol [18], to which each subsystem is required to adhere. Signals are transmitted and received to and from the FEEs by by means of optical fibres. Timing and control signals are sent via high-speed serial Control links (CLINK) while the data are received on high speed serial Data links (DLINK). The signals sent between the ROMs and the different FEE elements are time multiplexed onto the high-speed links. (16×59.5Mbit/s $\times$ 5/4 encoding overhead $\simeq 1.2\ Gbit/s$).

The untriggered ROMs are unique to the EMC DAQ system and are discussed below.

3.4 Description of the EMC Electronics.

3.4.1 Overview.

There are a total of 6580 CsI crystals in the EMC; 5760 in the barrel and 820 in the forward end cap. The crystals in the barrel are arranged into 48 rings in θ of 120 crystals. In the forward end cap there are 8 rings of decreasing size; three of 120 crystals, three of 100 and two of 80 crystals.

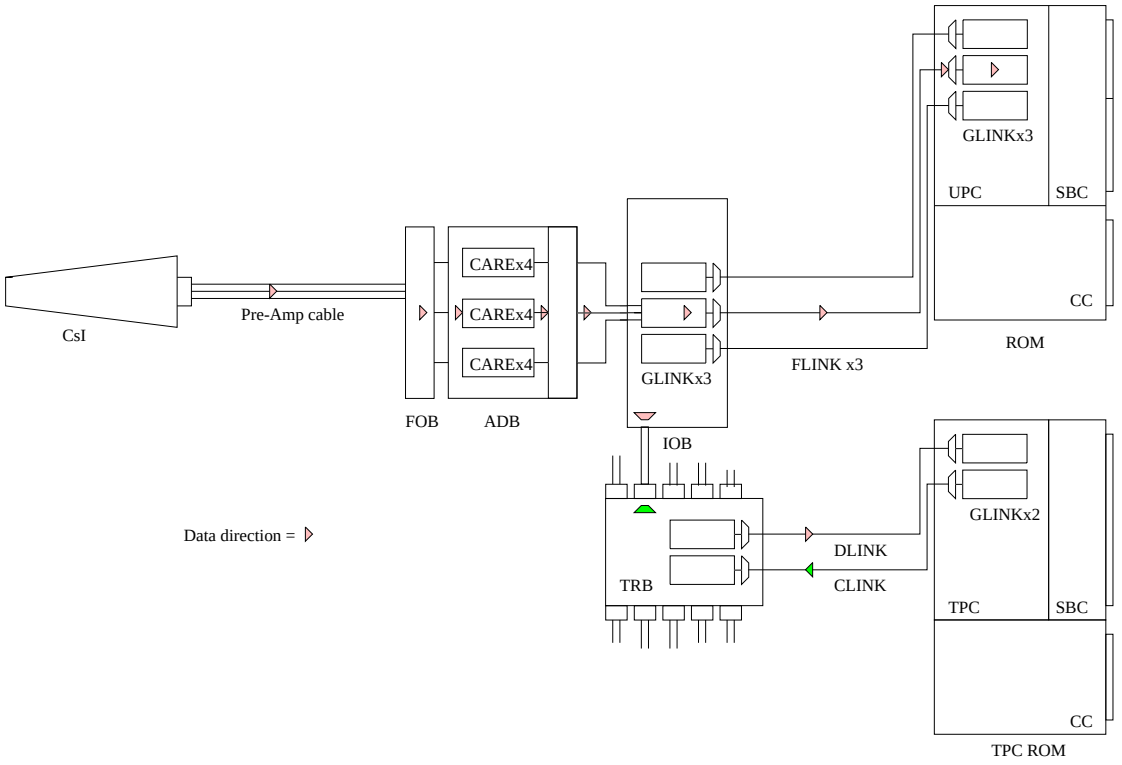

Figure 3.3: The EMC Front End Electronics.

Each crystal is instumented with a channel of electronics. Two photodiodes glued to the rear face of each crystal collect the scintillation light. Two photodiodes are used for common mode rejection and also to reduce the number of dead channels caused by photodiode failure. The signal from each photodiode is amplified by a pre-amplifier which is mounted as close to the photodiode as possible to avoid noise due to extra capacitance. The two pre-amplifiers and some calibration circuitry are integrated onto a small circuit board which is enclosed in a shielded cannister. A shielded ribbon cable connects the pre-Amplifiers to the rest of the electronics chain. In the EMC barrel the pre-amplifier cables run out to mini-crates mounted on each of the annular faces of the barrel. The crystals in the forward 24 rings are read out at the front face, the backward 24 rings are read out at the rear. In the forward endcap the mini-crates are mounted onto the rear side. In the barrel 72 pre-amplifier cables connect to each mini-crate via a Fan-Out Board (FOB), while in the endcap the mini-crates connect to 48 cables.

Each barrel mini-crate houses 6 Analogue-to-Digital Boards (ADB), while the endcap mini-crates house 4 ADBs. Each board containing the circuitry for 12 different channels. The ADB cards contain the Custom AutoRange Encoding (CARE) chip and ADC circuitry. These two components are the basis of a dynamic range sampling system that I will describe in more detail in the next section. There are 3 CARE chips per ADB card, each containing 4 channels. Mounted to the front face of each crate is an Input-Output-Board (IOB). The output of 24 channels (2 ADBs) is time multiplexed on the IOB board and read out serially through an optical fibre (FLINK) to an untriggered ROM in the Electronic house. Each untriggered ROM receives the output from one IOB, which is 2 or 3 fibres depending on whether the ROM is serving the endcap or barrel respectively. The IOB and ADBs contain control registers that can control calibrations and configurations. These registers are written via the CLINK of a TPC ROM. The CLINK is distributed to each IOB board by a Transition Board (TRB). One TPC ROM controls the electronics corresponding to 10 UPCs and each EMC DAQ crate contains these 11 ROMs. The FEE system is illustrated in Figure 3.3.

3.4.2 Pre-amplifier and CARE.

The pre-amplifier and CARE constitute an 18-bit dynamic range sampling system. Although 18 bits are needed to cover the whole energy range a precision on each measurement of only 10 bits is sufficient. As 18 bit ADCs were not commercially available, low cost, low power 10 bit ADCs have driven the CARE design. The pre-amplifier splits the input signal into two amplification ranges x1 and x32 which are sent to the ADB independently. Both these ranges are input to the CARE where they are split into 2 more ranges which provide further amplification. The 4 different amplification ranges have total gains of x1, x4, x32 and x256. The circuit compares the output of all the amplification ranges with a reference voltage, VREF set to 90% of the range saturation. It then selects the highest gain range that has not exceeded this threshold. The amplified signal is then digitised by the 10 bit ADC and output along with a further 2 bits which signify the CARE range that was selected. Figure 3.4 illustrates the CARE function.

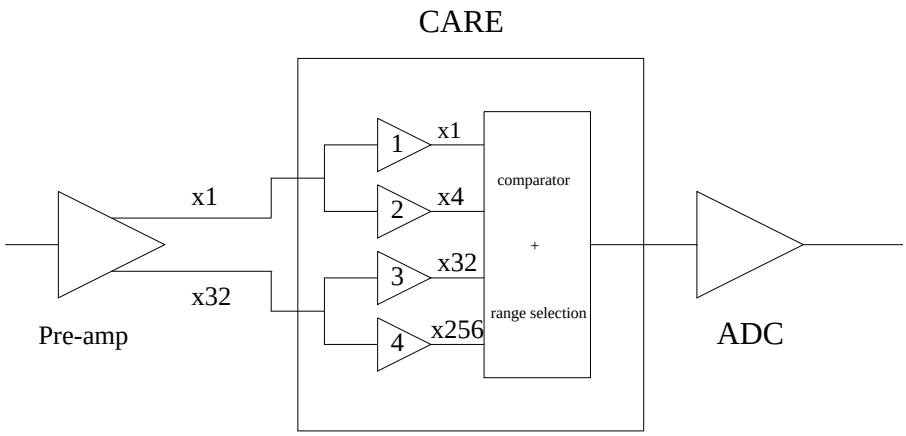

Figure 3.4: Pre-amplifier and CARE.

Figure 3.5 compares the expected contributions to the energy resolution from the digitization error and the intrinsic energy resolution of the CsI crystals, showing clearly that dynamic allocation of the amplification range is a valid method of reducing digitization error.

3.4.3 Electronic Calibration circuitry.

Under normal detector operation the injected charge pulses are produced by the photodiodes on absorption of the scintillated radiation of the CsI crystals. However during an electronic calibration the charge pulses are produced by the use of calibration circuitry, built into the pre-Amplifier and CARE.

The calibration circuitry injects the charge pulses directly into the input of the pre-Amplifiers. The pre-Amplifier contains circuitry that makes the calibration pulse shape similar to a pulse produced from a photodiode.

The charge pulses are created by discharging either of two capacitors. The use of two capacitors ensures that a large enough set of data points can be taken in all 4 CARE ranges. The two capacitors have capacitances of approximately $220fF$ and $1.8pF$ and are selected by means of a CARE control command. The voltage across

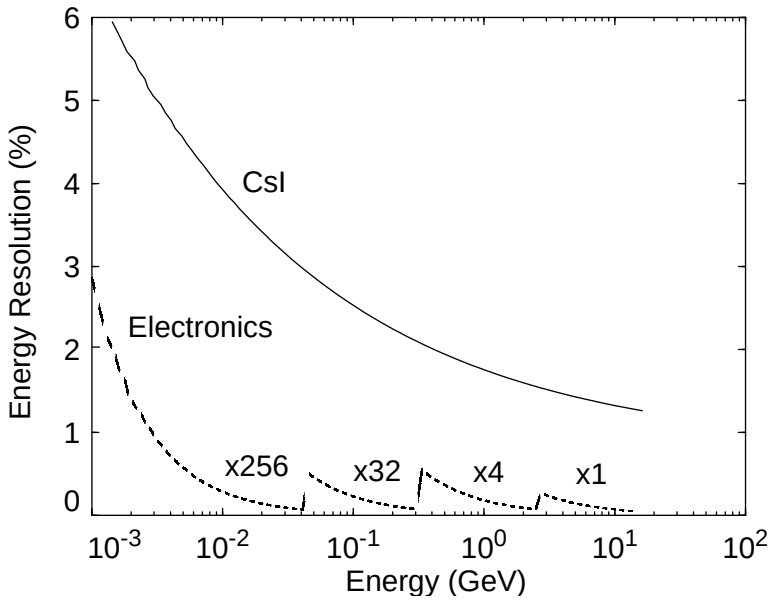

Figure 3.5: Contribution to the EMC energy resolution due to digitization.

the chosen capacitor can be varied between $0 - 2V$ and is set by means of an IOB control command. A 16 bit DAC converts the digital control signal value to the appropriate voltage. The DAC swings both postively and negatively allowing the linearity of each CARE range to be determined down to zero input charge.

An important detail of the operation of the calibration circuitry is the effect of the "Cal Strobe". The "Cal Strobe" is a differential signal AC coupled to the calibration voltage, which is used to signal the calibration capacitors to discharge. The effect of the "Cal Strobe" is to cause a negative offset to the calibration voltage of approximately $0.2V$. This effect must be properly taken into account in the the electronic calibration. Figure 3.6 shows illustrates the Cal Strobe signal.

3.4.4 Untriggered Personality Card.

The UPC is one of 3 cards comprising an untriggered ROM as descibed above. As untriggered ROMs are unique to the EMC DAQ system, the UPC can be considered as the final stage of the EMC electronics. The UPC receives data from the FEEs via the FLINKs. Each FLINK delivers a continuous stream of packets containing

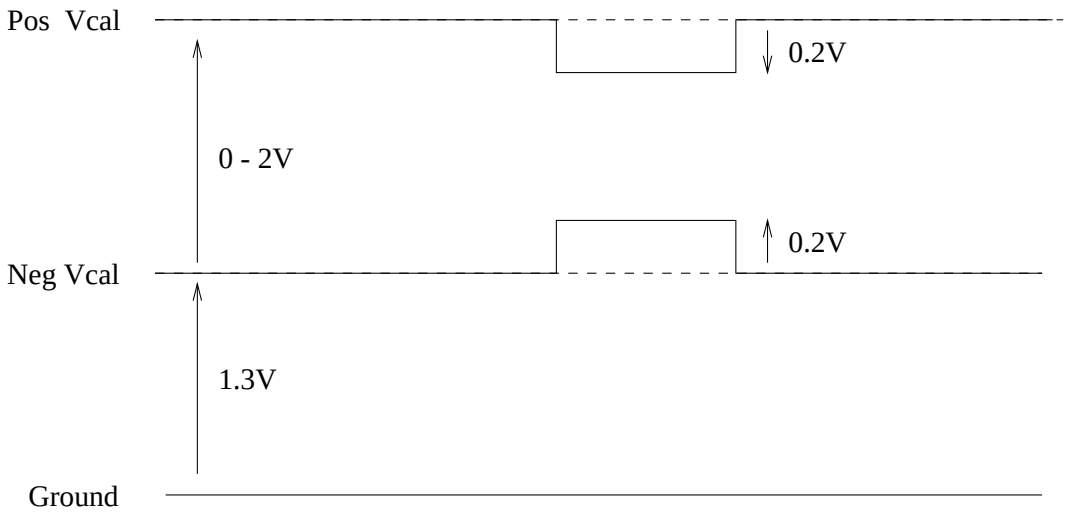

Figure 3.6: Cal Strobe signal.

the digitization result of 24 channels (2 ADBs), bits to signify whether a L1 Accept or Cal Strobe signal was received in the sample period covered by the packet, plus some diagnostic information (i.e wallclock, IOB serial number). On the arrival at the UPC the packets are decoded and the raw digitised 12 bit word from each channel is fed into a Look Up Table (LUT). A 16 bit energy is then selected, corresponding to the CARE range (the first 2 bits) and the 10 bit ADC word.

3.5 Electronic calibration.

3.5.1 Calibration aim.

This section describes a study I undertook with the purpose of showing that the EMC FEEs could be calibrated, to adjust the systematic effects caused by non-linearities in the electronics response.

The response of each channel of electronics to input charge is unique, varying according to the tolerances of a number of components within the electronics circuitry. The variation in the pedestals and gains of different channels and the presence of non-linearities in the electronic's response is considerable enough to impact on the detector resolution if not dealt with adequately. The electronic calibration is undertaken in order to correct for these deviations by accurately determining the param-

eters that characterise the response of each individual channel, across the entirety of its dynamic range. In order for each parametrization to be valid, the residual difference between the parametrization and the actual electronics response must be such that the difference does not deteriorate the EMC resolution beyond that set out in the electronics design specification.

3.5.2 Calibration Method.

The first stage of the calibration procedure was to generate the necessary calibration data to perform the study. The data used were generated directly after the installation of the electronics onto the detector, as as part of the electronics testing procedure.

The data were produced by generating calibration pulses across the DAC range using each of the calibration capacitors. The CARE's auto ranging feature was disabled and each of the CARE ranges was manually selected in order to allow the entirety of each range to be sampled. Each DAC point chosen was pulsed ten times. It is important to note at this point that the calibratrion relys on the fact that all the non-linearity results from the CARE/ADC system and that the charge injection system can be considered to be completetly linear.

Figures 3.7 and 3.8 show the raw ADC output of each CARE range of a typical electronics channel, using the $220fF$ and $1.8pf$ capacitors to generate the charge pulses respectively. As the ADC is 10 bit the saturation point of each CARE range is 1023 ADC counts, which is evident in both figures. When the $220fF$ capacitor is used with CARE ranges $\times 1$ and $\times 4$ the voltage supplied to the DAC is at a maximum before the ADC reaches its maximum value, as seen in figures 3.8(a) and (b).

The next step was to select the data points suitable for fitting, i.e, removing the points at which the ADC had saturated and points about the pedestal value. The

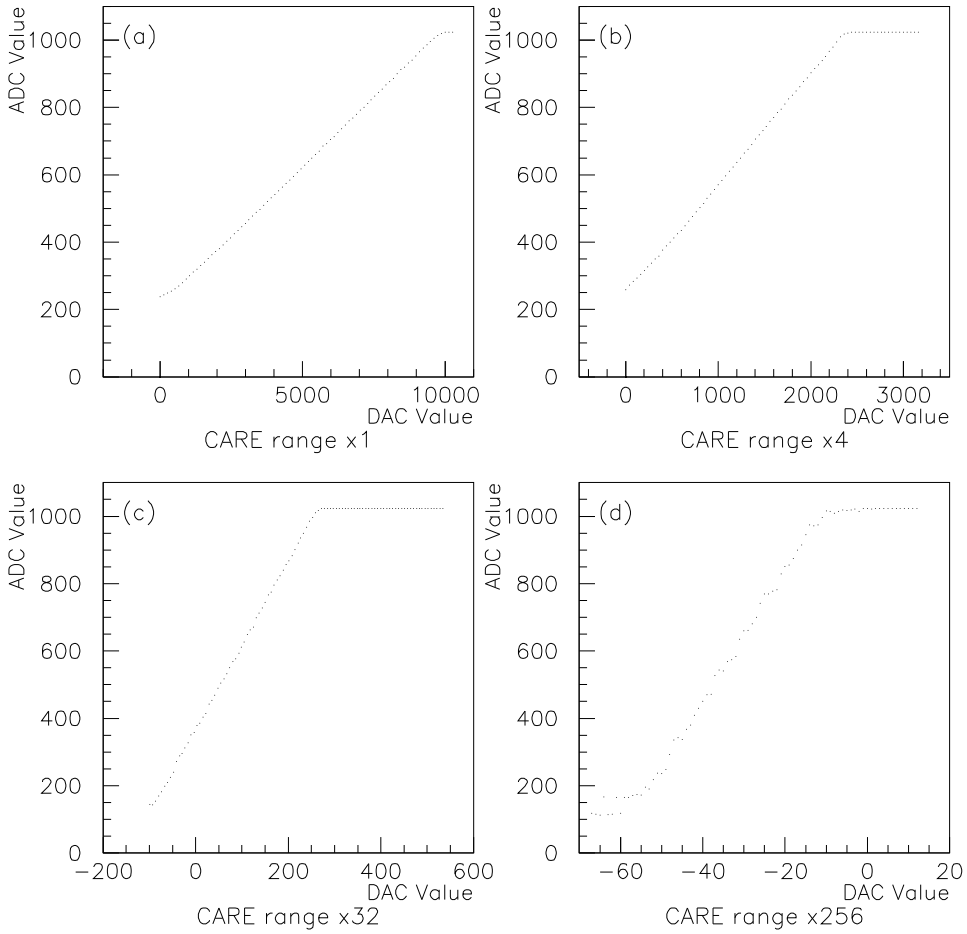

Figure 3.7: Raw calibration data using $1.8pF$ calibration capacitor.

cuts in table 3.1 were applied to the data points in each CARE range for all electronics channels.

The final step of the calibration procedure was to perform the parametrization.

3.5.3 Parametrizing the CARE response.

The parametrization of the EMC channels is undertaken to compensate for non-linearities in the electronics output. The parametrization of the electronics channels is made complicated by the use of the autoranging CARE which means that parameters must be sought for each of the individual CARE ranges. When devising a

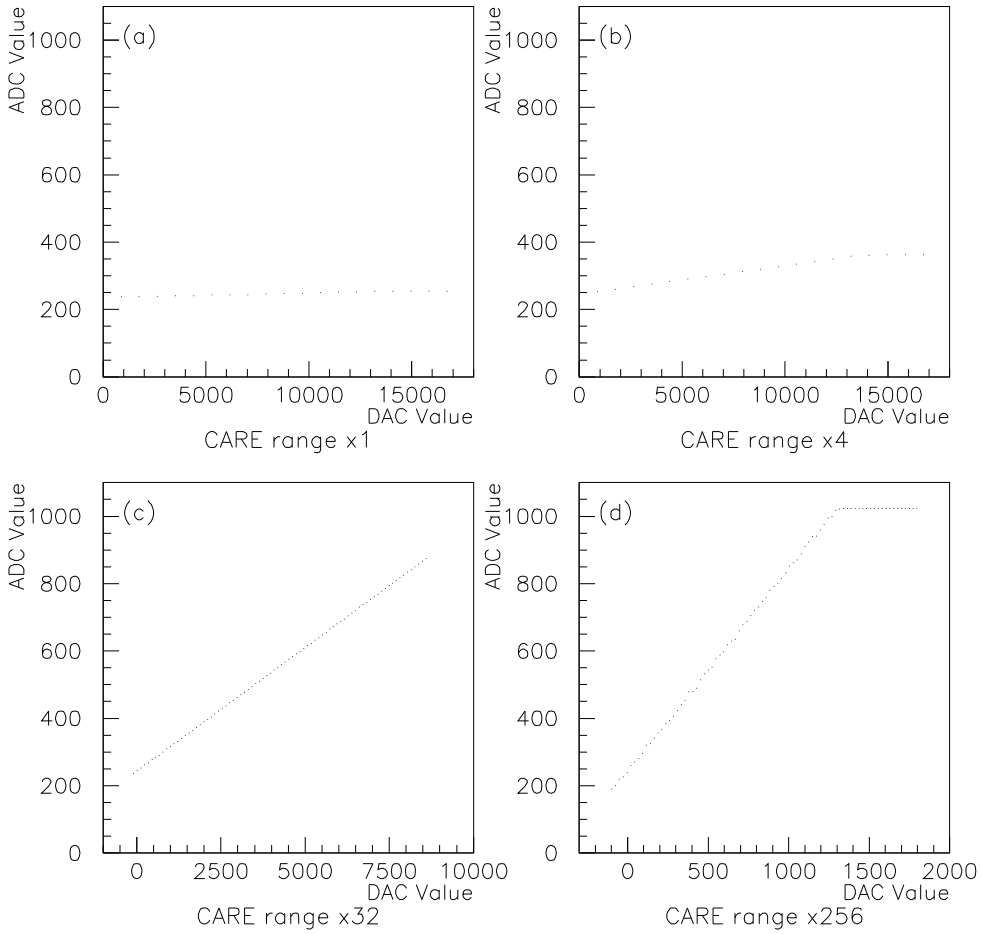

Figure 3.8: Raw calibration data using $220fF$ calibration capacitor.

stratergy for parametrizing the electronics a number of points need to be taken into consideration,

• the gain and pedestal of the electronics response depends on which CARE range is in use.

• In order to calibrate across the whole of each of the CARE range the use of both the calibration capacitors needs to be employed. As the tolerances of the capacitors are considerable the capacitor ratio constitutes another parameter that needs to be determined in the parametrization.

CARE Range	Capacitor	Minimum ADC Value	Maximum ADC Value
$\times 1$	1.8 pF	300	1000
$\times 1$	220 fF	500	
$\times 4$	1.8 pF	250	1000
$\times 4$	220 fF	500	
$\times 32$	1.8 pF	200	1000
$\times 32$	220 fF	200	1000
$\times 256$	1.8 pF	220	1000
$\times 256$	220 fF	200	1000

Table 3.1: Electronics raw data cuts applied before fitting.

- The non-linearities are more prevalent in particular CARE ranges.

- The calibration strobe produces an additional offset to each CARE range, as it perturbs the DAC voltage by a small amount. The DAC offset must also be precisely determined in the calibration and contributes an extra parameter, x_0, to the fitting procedure.

If we were to assume that the response of each CARE range were completely linear, then the minimum number of parameters needed to parametrize the electronics response would be ten: four CARE range gains, four CARE pedestals, the ratio of capacitances of the calibration capacitors and the DAC offset.

When examining the contribution to the resolution caused by the residual difference between a linear parametrization and the electronics response, the simple assumption that the CARE ranges can be treated as essentially linear is found not to be the case for the $\times 4$ gain ranges. Figure 3.9 shows the residual difference between the raw data and a straight line fit to the raw data points. Instead of being evenly distributed about zero across the whole range, the residuals form a hump shape, this hump shape repeats itself in the residuals throughout all of the electronics channels in the $\times 4$ range. This feature is a consequence of feed through from the higher amplification ranges of the pre-amplifier. The obvious consequence being, that more parameters are necessary to describe the gain of the $\times 4$ range in order to achieve

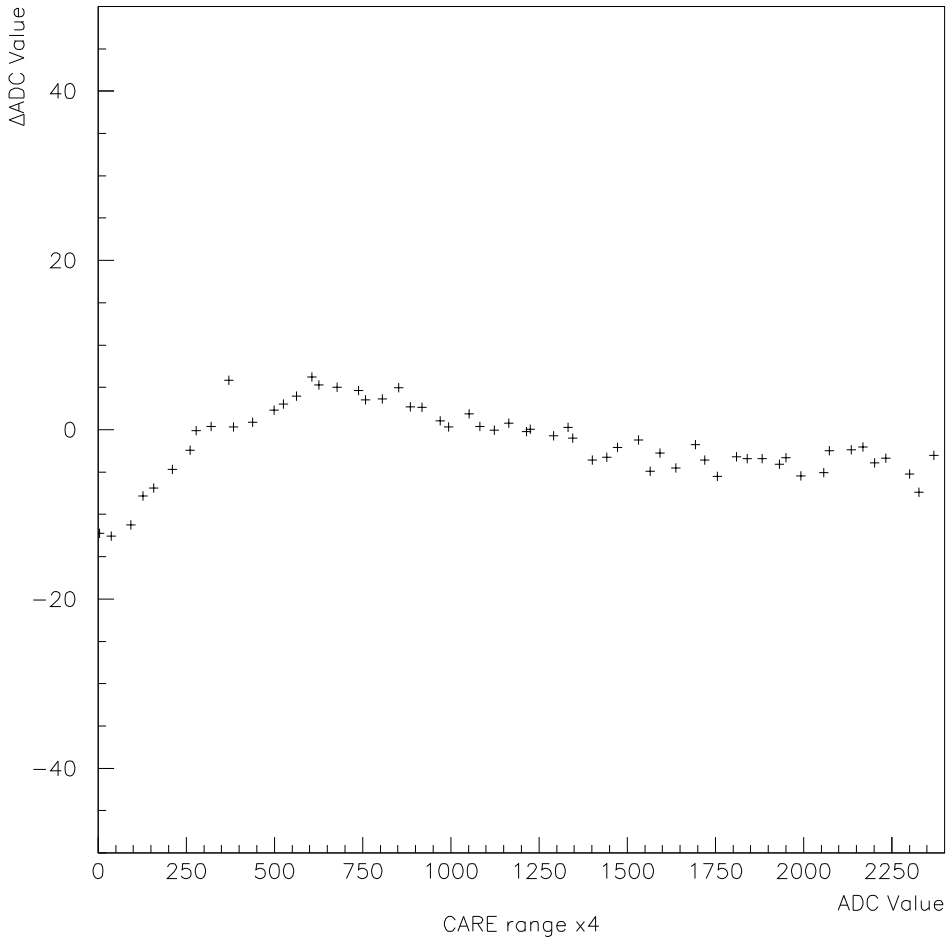

Figure 3.9: Raw data Channel A capacitor 1.

the desired EMC FEEs resolution.

For the case of the $\times 1$, $\times 32$ and $\times 256$ gain CARE ranges the ADC value is related to the DAC value by the simple equation 3.1,

$$y_{ADC} = m_r r_c (x_{DAC} + x_0) + c_r \tag{3.1}$$

where y_{ADC} is the ADC value, x_{DAC} is the DAC value, r_c is a function of the capacitance ratio, x_0 is the DAC offset and m_r and c_r are the gain and pedestal values for each CARE range respectively.

However, the $\times 1$, $\times 32$ and $\times 256$ gain CARE ranges can not be separately parametrized with straight line fits, as not all the parameters describing each CARE range are independent of each other. The same value for the capaticance ratio and the DAC offset must be used for all the CARE ranges.

In order to parametrize each channel to the level of accuracy required, the following algorithm was devised, which is essentially a non-linear sixteen dimensional least squares minimisation. The solution to the least squares minimisation technique is found by iteration and its success is highly sensitive to the choice of initial values used.

The first step of the procedure was to find good initial starting values in order to attempt the fit. This was achieved by parametrizing the 4 CARE ranges separately, to get an approximate value for the gains and pedestals.

The raw calibration data for the $\times 1$, $\times 32$ and $\times 256$ ranges is therefore parametrized by a straight line fit as a preliminary step, as described by equation 3.2, where y_{ADC} is the ADC value, x_{DAC} is the DAC value and $m_{c,r}$, $c_{c,r}$ are the gradient and pedestals respectively for CARE range, r and calibration capacitor, c.

$$y_{ADC} = m_{c,r} x_{DAC} + c_{c,r} \tag{3.2}$$

Comparing equation 3.1 with equation 3.2 the following relationships can easily be deduced,

$$m_{c,r} = m_r r_c \tag{3.3}$$

$$c_{c,r} = m_r (r_c x_0) + c_r \tag{3.4}$$

where r_c is the rescaling function used to combine data generated using different calibration capacitors, $r_c = 1$ for the $1.8pF$ capacitor and $r_c = r_{cap}$ for the 220 fF capacitor, where r_{cap} is the calibration capacitance ratio.

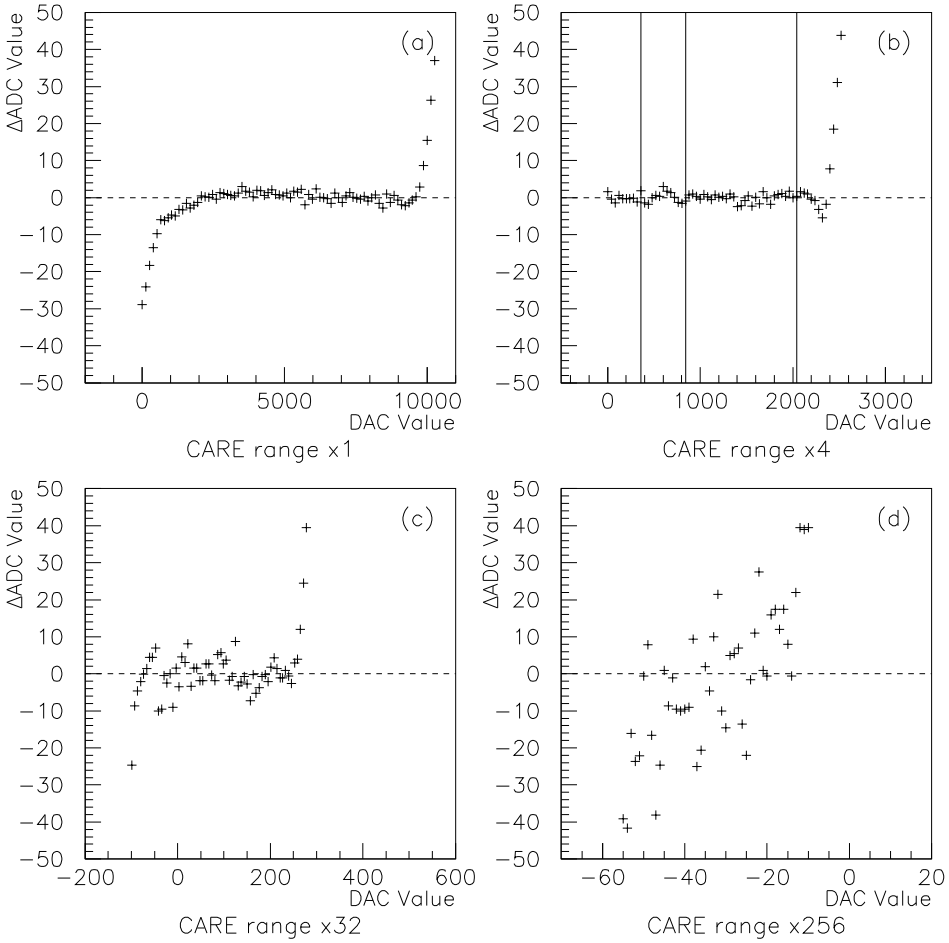

Figure 3.10: Residuals for data generated using the $1.8pF$ calibration capacitor.

An initial value for the capacitance ratio is guessed, then by using relationships 3.3 and 3.4, values for the gains and pedestals can be extracted from a Least Squares (LS) straight line fit to the raw data for each CARE range. Where the fits are applied to the combined data, generated using both calibration capacitors with the appropriate rescaling.

For the $\times 4$ channel, initial values for the gain and pedestal can be found by using essentially the same method as above, except a four line segment fit is used rather than a single straight line fit. Although there are other possible approaches to deal

with the non-linearities in the $\times 4$ channel, such as the use of a polynomial fit, the chosen approach is capable of paramatrizing the range to the desired requirements and seems more consistent with the parametrization of the other ranges. However this approach introduces an additional 6 parameters into the parametrization, an extra two parameters per line segment, the gain and the pedestal (or equivalently, the DAC value for the segment start point).

To find a more accurate initial value for r_{cap} one can then minimise the derivative

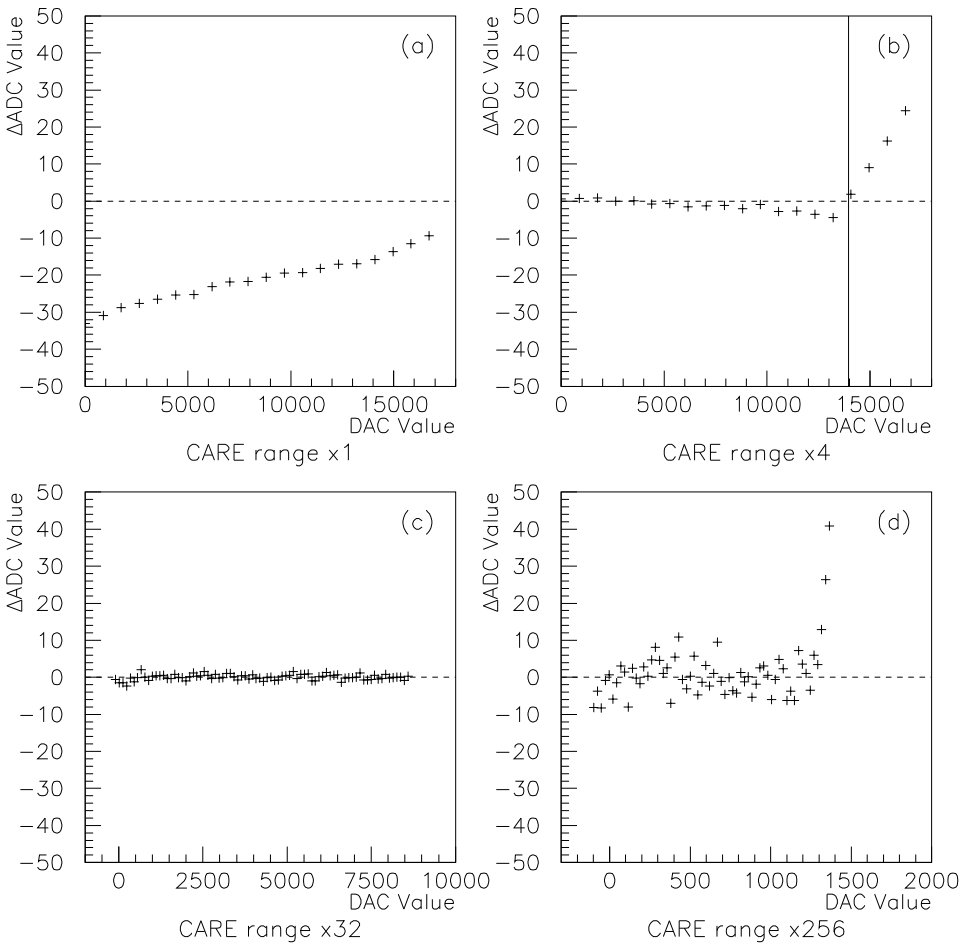

Figure 3.11: Residuals for data generated using the $220fF$ calibration capacitor.

of the sum of the χ^2s for each range with respect to r_{cap},

$$\frac{\sum_r \partial \chi_r^2}{\partial r_{cap}} = 0 \tag{3.5}$$

Practically, this is achieved by an iterative method. Firstly the combined χ^2 for each of the fits is evaluated using a particular value of r_{cap}. The derivate of the χ^2 with respect to r_{cap} is then determined. This process is then repeated using,

$$r_{cap}^{'} = r_{cap} + \delta r_{cap}, \tag{3.6}$$

where δr_{cap} is a small postive or negative increment, added with the intention of diminishing the magnitude of the derivative. The procedure is repeated until the derivative has converged to a value close enough to zero to be acceptable.

Once an initial value for r_{cap} is settled upon, the other inital parameters can then be properly evaluated. The gains and pedestals are extracted independently from each CARE range fit as described above and a suitable initial value for x_0 is found using the following equation,

$$x_0 = \sum_{r=1}^{r=4} \frac{c_{0,r} - c_{1,r}}{m_r(1 - r_{cap})} \tag{3.7}$$

which is the average value of x_0 extracted from each CARE range fit. The initial values were then used in a standard sixteen parameter non-linear least squares fit, which is described in detail below, to arrive at the final parametrization results.

3.5.4 Non-linear χ^2 fit.

A non-linear least squares fit uses an iterative procedure to find the parameters, the initial values found above are taken as a starting point. The gradients for the χ^2 with respect to each parameter is given by equation 3.8 where $\mathbf{a^0}$ is the vector of

parameters used in the fit, and f is the function being fitted.

$$\frac{\partial \chi^2}{\partial a_r}|_{\mathbf{a}=\mathbf{a^0}} = g_r(\mathbf{a^0}) = \sum_i -\frac{2}{\sigma_i^2}[y_i - f(x_i;\mathbf{a^0})]\frac{\partial f(x_i;\mathbf{a^0})}{\partial a_r} \tag{3.8}$$

The value $\delta\mathbf{a}$ is sought in order to minimize the χ^2 with respect to all the parameters used in the fit, as described by equation 3.9.

$$g_r(\mathbf{a^0} + \delta\mathbf{a}) = \frac{\partial \chi^2}{\partial a_r}|_{\mathbf{a}=\mathbf{a^0}+\delta\mathbf{a}} = 0 \tag{3.9}$$

$$g_r(\mathbf{a^0} + \delta\mathbf{a}) \approx g_r(\mathbf{a^0}) + \sum_s \frac{\partial g_r}{\partial a_s}\delta a_s = g_r(\mathbf{a^0}) + \sum_s \frac{\partial^2 \chi^2}{\partial a_r \partial a_s}\delta a_s \tag{3.10}$$

The second term in 3.10 is a matrix, G_{rs} which is given by evaluating equation 3.11.

$$G_{rs} = \frac{\partial^2 \chi^2}{\partial a_s \partial a_r} = \sum_i \left(\frac{-2}{\sigma_i^2}\right)\left[-\left(\frac{\partial f_i}{\partial a_s}\right)\left(\frac{\partial f_i}{\partial a_r}\right) + (y_i - f_i)\left(\frac{\partial^2 f_i}{\partial a_r \partial a_s}\right)\right] \tag{3.11}$$

Finally $\delta\mathbf{a}$ can be found by finding the inverse of G_{rs} and using equation 3.12.

$$\delta\mathbf{a} = -\mathbf{G}^{-1}\mathbf{g} \tag{3.12}$$

The value calculated for $\delta\mathbf{a}$ is then added to $\mathbf{a^0}$ and the procedure repeated until the parameters have converged.

3.5.5 Results

The 16 parameters of the non-linear least squares (χ^2) fit are therefore as follows, the 3 gradients and 3 pedestals for each of the $\times 1$, $\times 32$ and $\times 256$ CARE ranges, four pedestals and 4 gains covering the $\times 4$ range, the capacitor ratio and the offset on the DAC.

Figures 3.10 and 3.11, show the residual difference between the parametrization

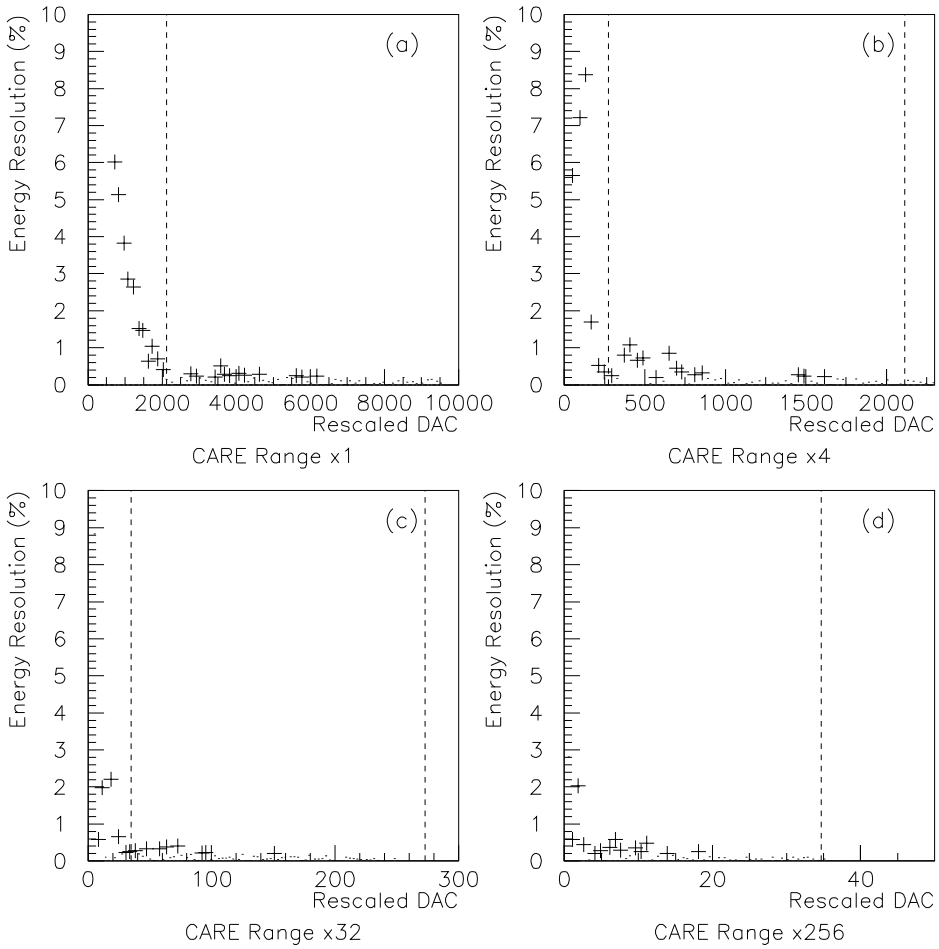

Figure 3.12: Contribution to resolution due to residual non-linearities.

and the raw data generated using the $1.8pF$ and $220fF$ calibration capacitors respectively, for each CARE range of a typical electronics channel. The thick vertical lines in the plots 3.10.(b) and 3.11.(b) indicate the positioning of the line segments used in the $\times 4$ CARE range. It should also be noted that the charge pulses are more susceptible to random noise when the $1.8pF$ calibration capacitor is used, which can also be seen in the residual plots. Note that the points from the $\times 1$ and $\times 4$ CARE ranges are ouside the points selected and are therefore not used in the fit. The plots also confirm that the residuals of the points used in the fitting procedure are evenly distributed about zero, except for a negligible but visible bump, remaining in the $\times 4$ gain range.

Figure 3.12 indicates the contribution to the energy resolution from the parametrization. The energy resolution has been roughly calculated using,

$$\Delta E = |y_i - f(x_i)| / f(x_i) \tag{3.13}$$

where $f(x_i)$ is the parametrization function for point x_i on the DAC and $|y_i - f(x_i)|$ is the magnitude of the residual at that point, normalized by the random noise[2] for the particular calibration capacitor. The dashed vertical lines indicate where the autoranging circuitry switches from one range to another. The saturation points have been removed from this plot and the DAC has been rescaled in order to combine points generated from the use of both calibration capacitors, where the rescaled DAC x'_{DAC} is given by,

$$x'_{DAC} = r_c(x_{DAC} - x_0) \tag{3.14}$$

The final plot 3.13, compares the parametrization energy resolution contribution

CARE Range	Segment	Gain (m)	Pedestal (c)	Capacitor ratio (r_{cap})	Offset (x_0)
×1	1	0.082847	209.081	0.0297114	-1680.69
×4	1	0.328605	242.828	0.0297114	-1680.69
×4	2	0.311455	250.961	0.0297114	-1680.69
×4	3	0.332397	237.868	0.0297114	-1680.69
×4	4	0.329094	242.239	0.0297114	-1680.69
×32	1	2.48967	366.267	0.0297114	-1680.69
×256	1	19.9715	1243.95	0.0297114	-1680.69

Table 3.2: Parameters describing a typical channel of electronics.

from a typical electronics channel with the intrinsic CsI resolution. The energy scale on this plot is approximate and follows from the assumption that the saturation point of the ×1 gain CARE range is ∼13 GeV.

[2]The 1.8pF is more susceptible to random noise which has to be taken into account.

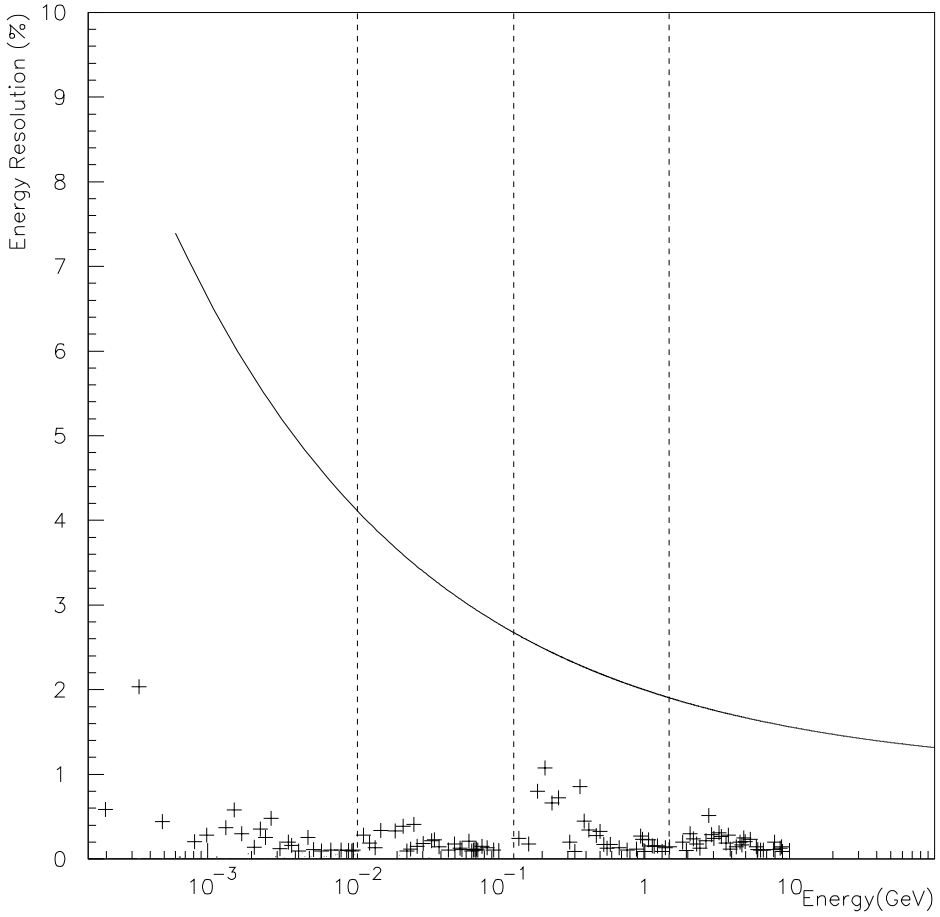

Figure 3.13: Energy resolution contribution from residual non-linearities compared to CsI resolution.

Typical values for the parameters describing an electronics channel are shown in table 3.2.

3.6 Summary

This study has shown that a parametrization of the EMC FEEs to correct for non-linearities is possible. This parameters found in the electronic calibration are used in conjuction with the 6 MeV source calibration, which establishes the lower point of the energy scale, are used to generate the the look up table of energies stored in the UPC.

Chapter 4

Photon Selection.

4.1 Monte-Carlo analysis method.

The aim of this study was to investigate the feasability of a measurement of the inclusive $b \to s\gamma$ branching fraction at BaBar and to devise the necessary techniques which could be applied to make an actual measurement. In order to achieve these aims I have developed two different analysis algorithms. The analysis algorithms were developed with use of fully reconstructed Monte-Carlo events as the data input. The Monte-Carlo events were generated using the following software packages, unique to the BaBar collaboration, **EvtGen**, **SimApp** and **Bear**.

• **EvtGen** is used to generate the 4 vectors of the particles produced in the e^+e^- interactions.
• **SimApp** is used to simulate the interactions between the produced particles and the BaBar detector. **SimApp** also simulates the detector response to each event, outputing the digital readout, "digis", from each of the detector's electronic channels.
• **Bear** is the BaBar reconstruction software and produces the final data objects used for data analysis, EMC clusters, drift chamber tracks, etc. The input of the Bear algorithm can be either the digis produced by SimApp or the output of the real BaBar detector.

The Monte-Carlo data sample generated consists of a total of 40,000 signal events,

$\sim$50,000 generic $b\overline{b}$ events and $\sim$200,000 continuum events.

The methodology of the two analyses is as follows.

• The first step is photon selection. The photon radiated in a $b \to s\gamma$ process is a characteristic signature of the event. Candidate events are selected on the condition that they contain an EMC cluster which is consistent with a cluster produced by a $b \to s\gamma$ photon.

• The second step is to further increase the signal to background ratio using background discrimination techniques. Event-shape variables were used as discriminators, taking advantage of the different morphologies of signal and background events. A quasi-reconstruction of the B meson was also used to reject background.

4.2 Signal.

Inclusive $b \to s\gamma$ is the combination of exclusive $b \to s\gamma$ modes and non-resonant decays. The observed decay is $B \to X_s\gamma$, where X_s is a state containing an s quark. As the only types of B mesons produced at BaBar are B^0 or B^{+-} and since their constituent quarks are a combination of a b and a u or a d quark, X_s is either a single kaon resonance or in the non-resonant case, a single kaon plus multiple pions.

In the exclusive case the quarks form a bound kaon state. The mass distribution for resonant X_s is the relative sum of the Breit-Wigner distributions for each type of kaon resonance. Each type of resonant X_s produced in inclusive decays represents a different exclusive $b \to s\gamma$ mode and the relative heights of each Breit-Wigner distribution depends on the relative ratios of the exclusive $b \to s\gamma$ decays.

$$E_\gamma = \frac{M_B^2 - m_{X_s}^2}{2M_B} \tag{4.1}$$

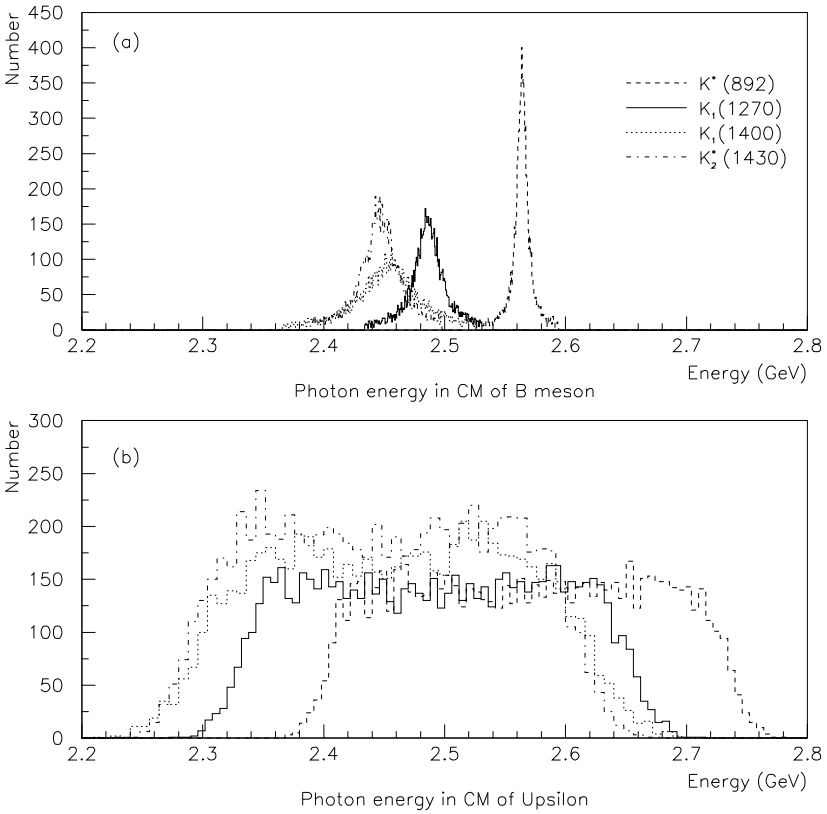

Figure 4.1: (a) Signal photon energy spectrum in the B mesons CM frame. (b) Signal photon energy spectrum in the $\Upsilon(4s)$ CM frame for exclusive $b \to s\gamma$ modes.

In the non-resonant case the quarks do not form a bound state and instead hadronize, resulting in a continuum of possible masses for X_s which is directly related to the inclusive $b \to s\gamma$ photon energy by equation 4.1, where M_B is the mass of the decaying B meson and m_{X_s} is the mass of X_s.

In order to test the Standard Model prediction for $b \to s\gamma$, one would ideally like to have accurate theoretical results predicting the relative exclusive contributions and the non-resonant contributions to $b \to s\gamma$. Using these values one could then generate MC events for the different types of $b \to s\gamma$ in the same proportions and compare the results of the analysis algorithm between the Monte-Carlo and real data. At present the relative contributions of each of the exclusive $b \to s\gamma$ modes to

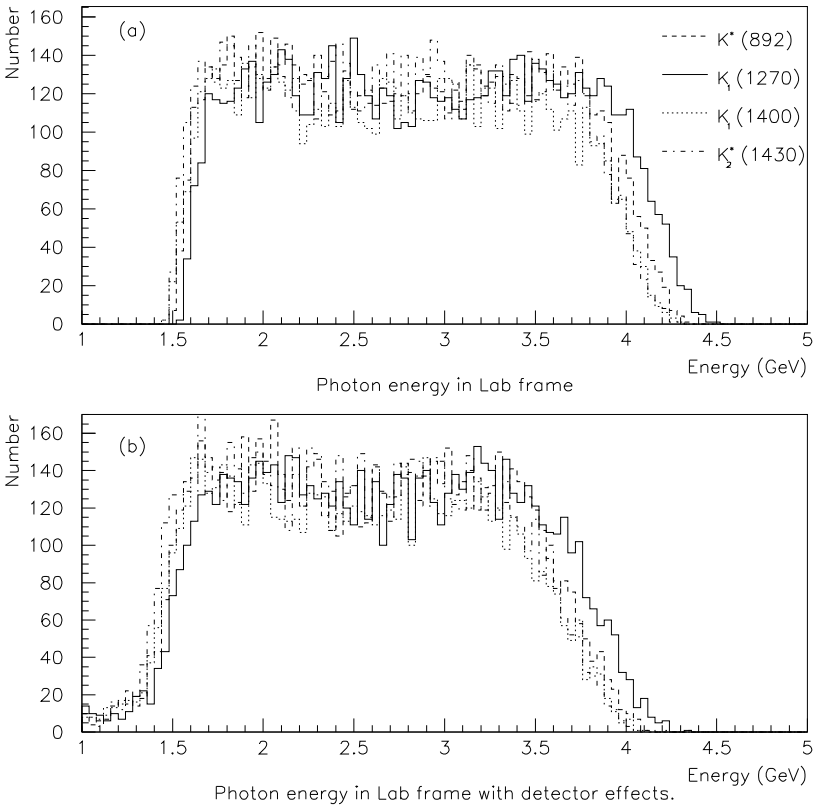

Figure 4.2: (a) Signal photon energy spectrum in the laboratory frame. (b) Signal photon energy spectrum in the laboratory frame with detector effects for exclusive $b \to s\gamma$ modes.

the total inclusive $b \to s\gamma$ decay rate and the contribution from non-resonant decays are unmeasured and can only be estimated by theoretical calculations with a large amount of uncertainty [11].

The Monte-Carlo signal events used in my analysis consist of equal proportions of four different exclusive $b \to s\gamma$ modes, $B \to K^*(892)\gamma$, $B \to K_1(1270)\gamma$, $B \to K_1(1400)\gamma$ and $B \to K_2(1430)\gamma$. Each of these modes included decays of both neutral and charged B mesons, also in equal proportions. The theoretical estimates suggest that these exclusive modes are the dominant contributions to the inclusive $b \to s\gamma$ branching fraction. By studying the sensitivity of the cut efficiencies for the different modes, systematic errors due to the lack of knowledge of the relative exclusive contributions can be estimated.

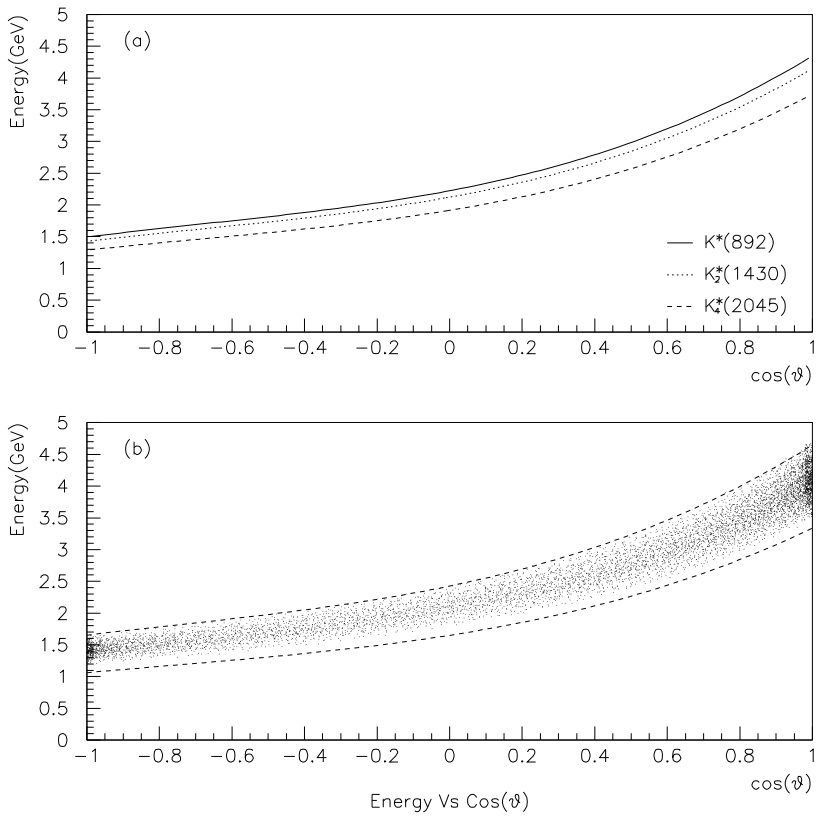

Figure 4.3: Various exclusive modes plotted against theta.

A $b \to s\gamma$ event is essentially a two body decay, where the radiated photon recoils against X_s. The photon energy is equal to the recoiling momentum and is a fixed function of the X_s mass. In the CM frame of the decaying B meson the photon energy is given by equation 4.1.

Table 4.1 shows the mean photon energy for various kaons produced in $b \to s\gamma$ exclusive modes. Only the first four were simulated.

Figure 4.1.(a) shows the energy spectra of the radiated photons from the decays of the four simulated exclusive signal modes in the CM frame of the decaying B meson. As an equal number of events where used for each mode the relative heights of the distributions have no significance. However, the shapes of the distributions

kaon resonance	Mass (GeV/c^2)	Photon energy (GeV)
$K^*(892)$	0.892	2.564
$K_1(1270)$	1.270	2.487
$K_1(1400)$	1.402	2.453
$K_2^*(1430)$	1.430	2.446
$K_2(1770)$	1.770	2.343
$K_3^*(1780)$	1.780	2.339
$K_4^*(2045)$	2.045	2.243

Table 4.1: Kaon resonances and the corresponding photon energy in the CM of the B meson.

are significant. The differing means and widths of these distributions are a consequence of the fact that the distribution of each mode is related to the Breit-Wigner distribution of the corresponding X_s according to equation 4.1.

Figure 4.1.(b) shows the energy spectra of the radiated photons boosted into the CM frame of the Υ(4s). In the Υ(4s) frame the B's have a small amount of residual momentum $\simeq$200 MeV which is independent of the photon momentum. The effect of the boost is to broaden out the photon energy spectrum.

Figure 4.2.(a) and (b) show the energy spectra of the radiated photons boosted into the laboratory frame. The BaBar boost significantly broadens out the energy spectra. The photon energy is a minimum when it is radiated in a direction anti-parallel to the boost in CM frame of Υ(4s), conversely the photon energy maximum occurs when the photon is radiated in a direction parallel to the boost. Figure 4.2.(b) includes detector resolution effects, the must notable difference being a low energy tail due to energy leakage and the loss of the high energy photons.

In the laboratory frame the photon energy is heavily correlated with angle. Figure 4.3.(a) shows the mean photon energy as a function of $\cos(\theta)$ in the laboratory frame for a variety of exclusive modes. Figure 4.3.(b) shows the effect of the residual B momentum on the energy as a function of $\cos(\theta)$ for the same modes. It is this correlation that results in the loss of the high energy photons which are at an angle outside of the detector acceptance.

4.3 Backgrounds.

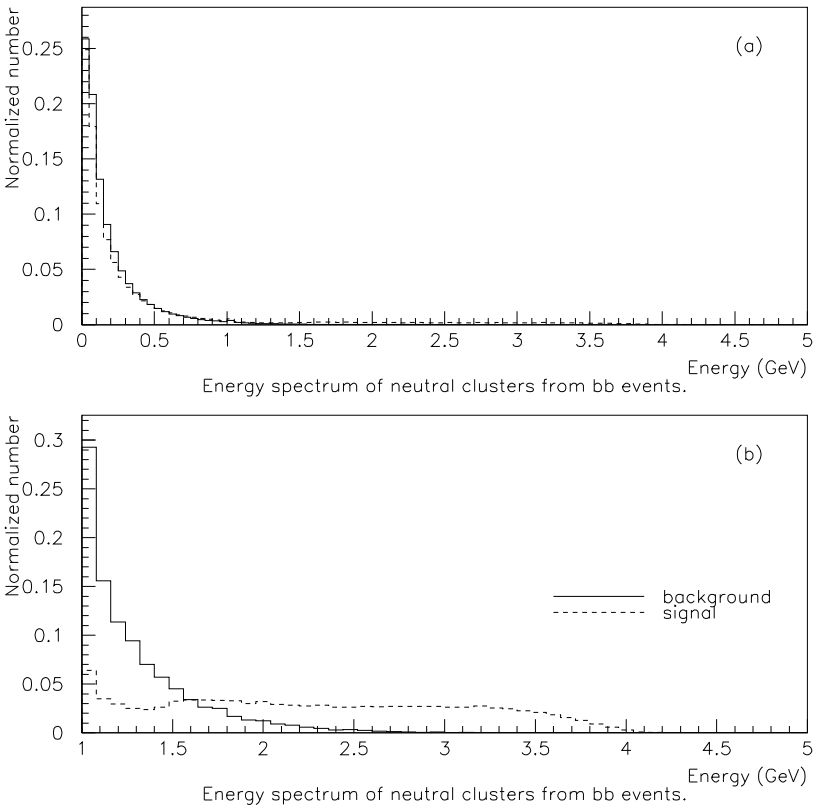

Figure 4.4: Comparison of the EMC neutral energy spectra for $b\overline{b}$.

There are a number of different backgrounds to consider when attempting a $b \to s\gamma$ measurement. As the radiated photon is the most distinguishing feature of a $b \to s\gamma$ event, the primary backgrounds are events where an EMC cluster of comparable energy to the radiated photon occurs. The major sources of these backgrounds are π^0's and η's decaying to two photons, merged π^0s and Initial State Radiation (ISR) photons. Other lesser sources of background are $\omega \to \pi^0\gamma$, long-lived neutrals and charged particles that the EMC reconstruction software fails to match to a track. The source of these neutral backgrounds are two distinct types of event: generic $b\overline{b}$ and continuum.

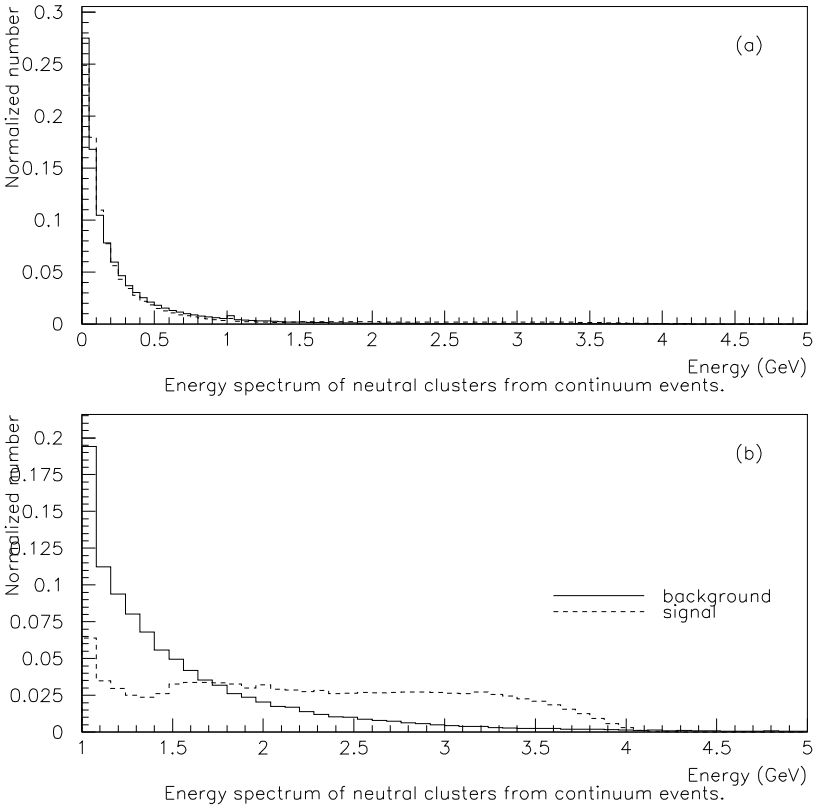

Figure 4.5: Comparison of the EMC neutral energy spectra for continuum.

4.3.1 Generic $b\bar{b}$ background.

Generic $b\bar{b}$ events are not expected to contribute significantly to the background of inclusive $b \to s\gamma$ as the energy spectrum of neutral EMC clusters produced in these events is generally lower than the inclusive $b \to s\gamma$ photon. Figures 4.4.(a) and (b) shows the generic $b\bar{b}$ neutral energy spectrum plotted against the signal photon spectrum in the laboratory frame, where both spectra are normalized to one.

There are a number of rare B processes which produce photons and π^0's in the same energy range with branching ratios that are not well known and could possibly be comparable to that of inclusive $b \to s\gamma$. For example, two body decays with π^0's or gammas in the final state such as $B \to D\pi^0$, $B \to K\pi^0$ or $B \to D\gamma$ are possible backgrounds. However a number of recent measurements suggest that

these channels may not be significant backgrounds to inclusive $b \to s\gamma$. A recent measurement from CLEO [19] sets an upper limit on $\overline{B}^0 \to D^{*0}\gamma$ of 5.0×10^{-5} at 90% confidence level. A branching ratio of 10^{-5} would be comparable with the exclusive $b \to s\gamma$ processes. However theoretical estimates predict that this branching ratio is of the order of 10^{-6}. The CLEO experiment has also recently measured the branching ratio of $B \to K^0\pi^0$[20] to be $(8.2^{+3.1}_{-2.7} \pm 1.2) \times 10^{-6}$, a factor of 10 less than the exclusive $b \to s\gamma$ branching ratios and the charged B$\to K\pi^0$ has an upper limit of 1.6×10^{-5} with a confidence level of 90%. As only a fraction of the π^0s produced would be merged the Kπ process should not be significant. $B^0 \to \overline{D}^0\pi^0$ has an upper limit of 1.2×10^{-4} with 90% C.L. $B^+ \to D_s^+\pi^0$ has a limit of 2.0×10^{-4} but once again only a fraction of the π^0s are merged.

The possibility of a background from inclusive $b \to d\gamma$ is unlikely as the process is CKM suppressed, the ratio between the two processes is approximately given by $|V_{td}/V_{ts}|^2$. Neither V_{td} or V_{ts} is well known, but using current values the maximum number of $b \to d$ events would be 17% of the number of $b \to s\gamma$ events and the minimum would be 0.7%.

Initial state radiation is not present in generic $b\overline{b}$ events as producing a photon of sufficient energy would cause the beam CM energy to drop below the $b\overline{b}$ production threshold.

4.3.2 Continuum background

Continuum contributes to the background in the form of high energy photons produced by the decays of π^0's, η's, merged π^0's and ISR photons. Continuum events are jets formed from the hadronization of u, d, s or c quark anti-quark pairs. Figure 4.5 compares the normalized neutral energy spectrum for continuum with the normalized photon energy spectrum of inclusive $b \to s\gamma$. The typical continuum neutral energy is lower that $b \to s\gamma$ but there are significantly more continuum events. The cross section for continuum event production at the $\Upsilon(4s)$ is $3.3nb$ compared to $1.05nb$ for generic $b\overline{b}$ production. This corresponds to $\simeq$ 5000 continuum events for every $b \to s\gamma$ event.

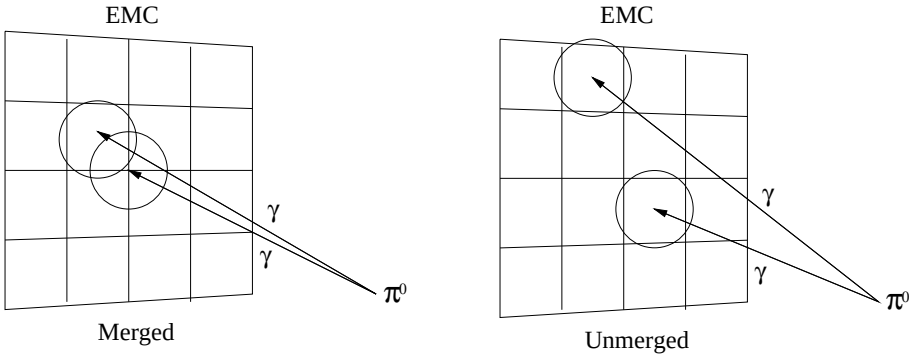

Figure 4.6: Merged and unmerged π^0 decay.

4.3.3 Merged π^0's.

π^0s decay ~98% of the time to two photons. A merged π^0 describes the situation when a high momentum π^0 decays to two photons which fail to separate enough such that they can be distinguished as different clusters, illustrated in figure 4.6. The π^0 then appears as a single cluster with energy equal to the π^0 energy. The EMC's ability to separate two neutrals is dependent on the distance between them, the crystal granularity and the Moliere radius of the crystal material. The EMC crystal faces have an average dimension of $47 \times 47mm^2$ and a Moliere radius of $36mm$. Approximately 90% of an electromagnetic shower is contained within one Moliere radius, thus effectively no showers are completely contained within one crystal. BaBar is particularly susceptible to this background in the forward region of the EMC where the π^0s are heavily boosted by the BaBar boost. Figure 4.7 shows the angular and energy distributions of merged π^0 clusters in the laboratory frame.

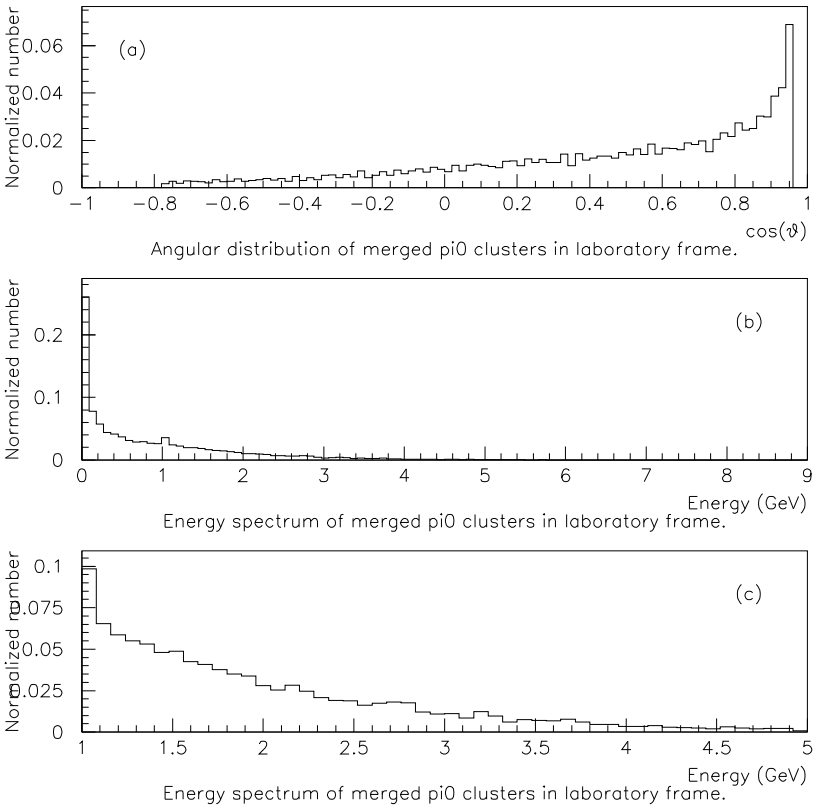

Figure 4.7: (a) Angular distribution of merged π^0 clusters. (b) Merged π^0 energy spectrum. (c) Merged π^0 energy spectrum within signal region.

4.3.4 π^0 and η background.

π^0's and η's decaying to two photons are a major source of background. The photons produced are typically of lower energy than the $b \to s\gamma$ signal but because the ratio of $b\overline{b}$ and continuum events to $b \to s\gamma$ is large and the combined multiplicity of π^0's and η's is approximately 7 per event, π^0's and η's represent a significant source of background to $b \to s\gamma$ processes. Figure 4.8 shows the angular and energy distributions of photons produced by π^0s and ηs in the laboratory frame (the artificial structure in this plot is due to the crystal granularity).

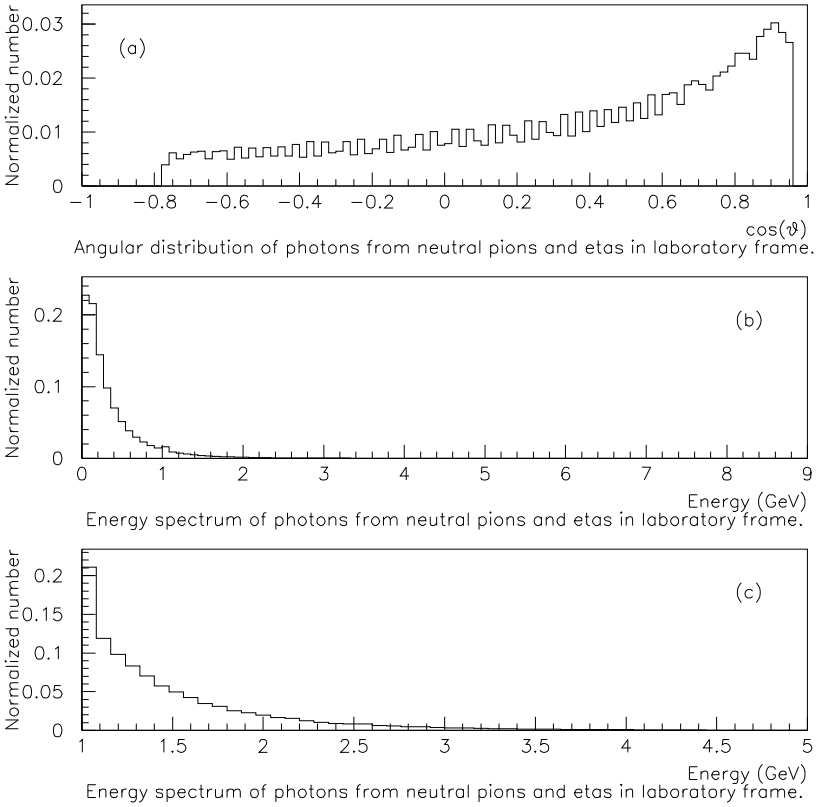

Figure 4.8: (a) Angular distribution of photons from π^0's and η's. (b) Photon energy spectrum. (c) Photon energy spectrum in signal region.

4.3.5 Initial State Radiation background.

An Initial State Radiation (ISR) event is an event where a photon is radiated by either the positron or electron before annihilation. The ISR Feynman diagram is illustrated in figure 4.9. As the electron-positron beams are tuned to the CM energy of the $\Upsilon(4s)$ the effect of ISR is to move the CM energy off resonance, which results in the production of $q\overline{q}$ (u,d,s,c) jets. Figure 4.10 shows the angular and energy distributions of ISR photons in the laboratory frame.

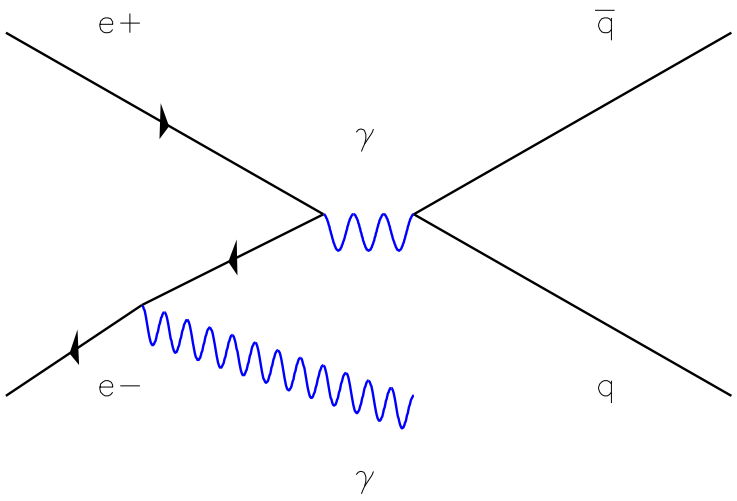

Figure 4.9: Initial State Radiation.

4.4 Photon Selection.

The primary signature of a b $\rightarrow$ sγ event is the radiated photon. Therefore a method of efficient photon selection is a likely prerequisite for any b $\rightarrow$ sγ analysis. This section describes the techniques I have employed for selecting signal photons over photons produced by the backgrounds. My method of photon selection is common to both the analyses described in this thesis. Figure 4.11 illustrates the severity the background present in this channel. The figures show (a) the photon spectrum for all the generic continuum backgrounds and the spectrum for signal scaled by the relatives proportions they are produced in 1 fb^{-1}, (b) comparing signal with the generic $b\overline{b}$ background.

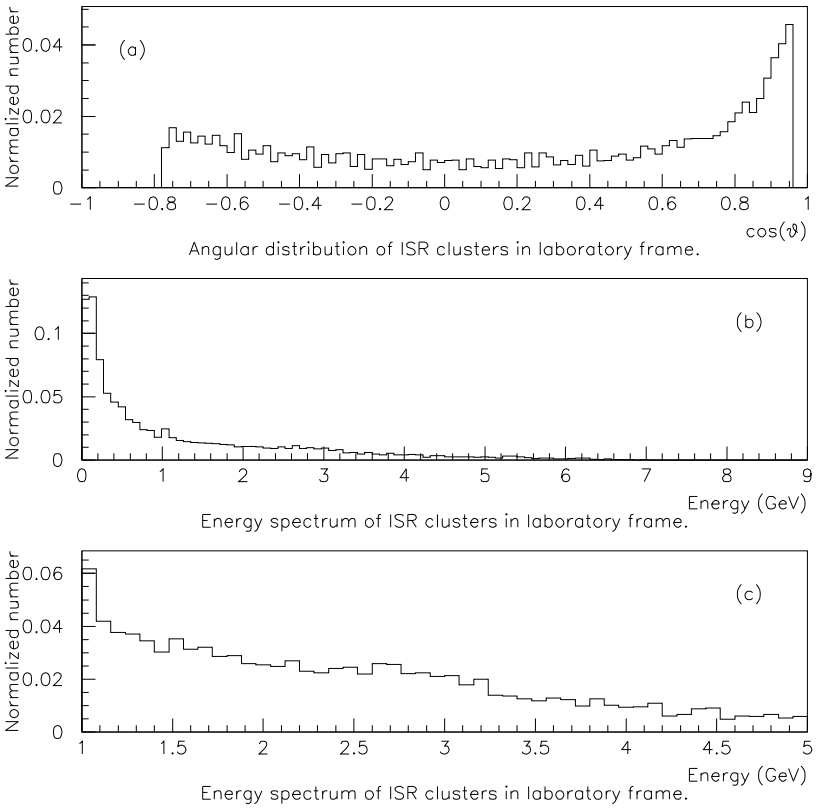

Figure 4.10: (a) ISR photon angular distribution. (b) ISR photon Energy spectrum within the EMC solid angle. (c) ISR Energy spectrum in signal region.

4.4.1 Photon detection.

Before selecting signal photon candidates it is necessary to determine the fraction of signal photons that can be detected. The direction of the radiated photon in the CM frame is isotropic, hence the fraction of photons accepted by the EMC is directly proportional to the solid angle coverage in the CM frame, ∼91%.

Photons are also lost due to pair production or scattering before reaching the calorimeter. The threshold for pair production is $\sim 1MeV$ and dominates over all other photon interactions in the signal energy region [21]. The photon encounters material in the form of the SVT, the Drift Chamber walls and the DIRC radiator bars. Monte-Carlo analysis predicts that pair production and scattering results in a further ∼9% reduction in photon detection.

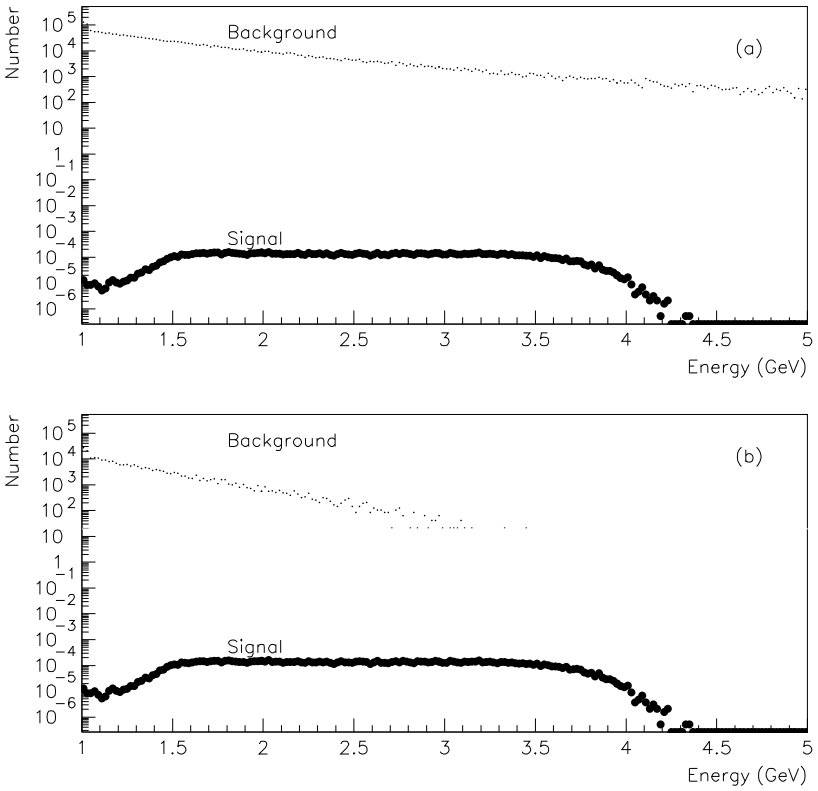

Figure 4.11: Photon spectrum, scaled to 1 fb^{-1} for (a) generic continuum background and signal, (b) generic $b\overline{b}$ background and signal.

Figure 4.12(a) shows the pair production vertex position in the rθ plane, outlining the SVT and Drift Chamber walls. Figure 4.12(b) shows that the angular distribution of the pair-producing photon peaks in the forward region due to the fact the SVT support structure is within the EMC solid angle.

In principle any photons that pair produce in the SVT or the inner wall of the drift chamber could be reconstructed by combining charged tracks, in practice the combinatorial backgrounds introduced by such a scheme are an unnecessary complication resulting in only a small improvement in photon detection. These effects mean that in the best possible situation only 82% of signal photons can be detected.

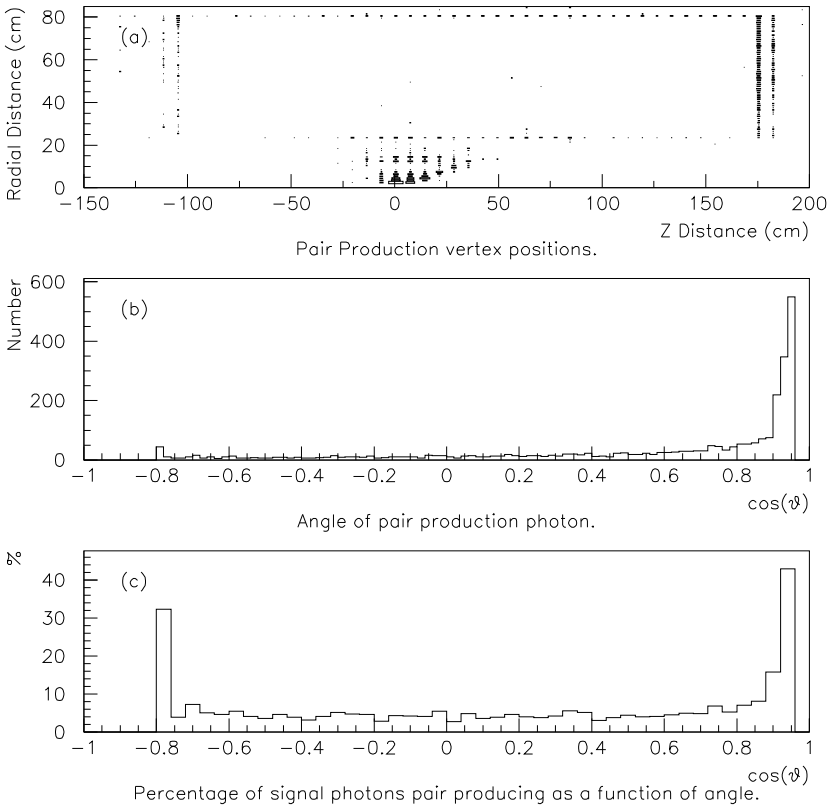

Figure 4.12: Photon pair production properties in the BaBar detector.

4.4.2 Energy cuts.

After comparing the energy spectra for signal and continuum it is quite clear that a cut on the energy of the candidate photon is beneficial in the rejection of background. Unfortunately deciding upon the bands for an energy cut is problematic in this analysis. The difficulty arises due to the fact that the proportions of the different exclusive modes and non-resonant decays that contribute to $b \to s\gamma$ are not well known and the energy of the photon is dependent on the mass of X_s. If the exclusive modes I have chosen for undertaking this Monte-Carlo analysis are not the dominant ones, then the results of this analysis could be biased. If the majority of inclusive $b \to s\gamma$ decays produced a more massive X_s product then these decays would also radiate a photon with lower energy than anticipated. If the cut on the energy were too low these modes would be rejected. The high energy cut on the

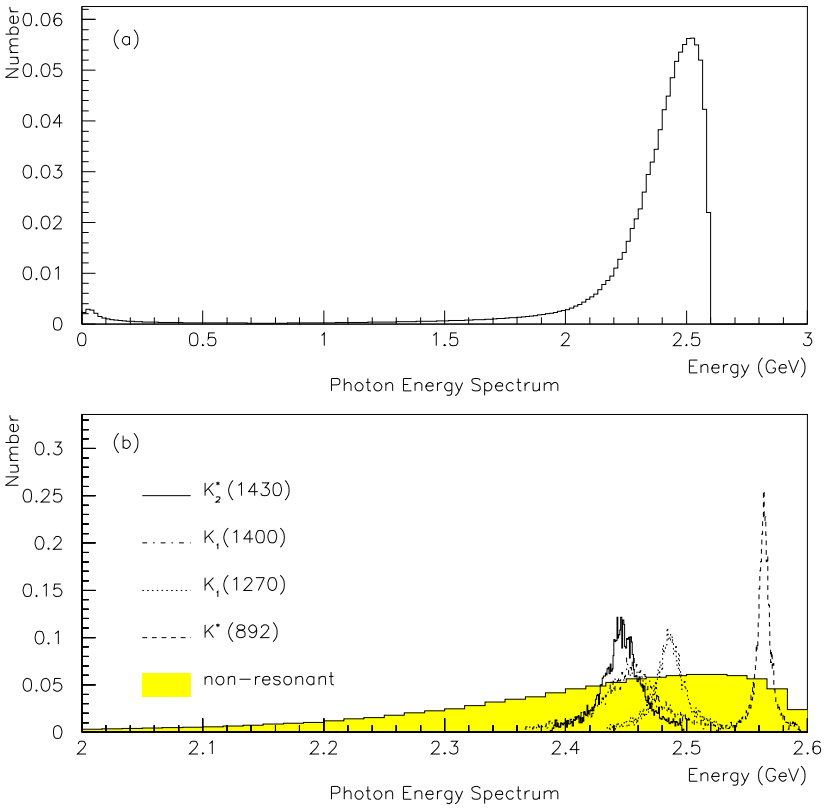

Figure 4.13: (a) Theoretical prediction of non-resonant $b \to s\gamma$ photon energy spectrum contribution. (b) Comparison of non-resonant and exclusive $b \to s\gamma$ photon energy spectra.

other hand is trivial as $K^*(892)$ is the lightest kaon resonance that it is possible to produce in an inclusive $b \to s\gamma$ decay (see appendix) and thus constrains the maximum photon energy. Figure 4.13.(a) shows the theoretically calculated photon spectrum for non-resonant $b \to s\gamma$ decays. More than 90% of non-resonant decays produce a photon of energy greater than 2 GeV. Figure 4.13.(b) shows the energy spectra of the different exclusive modes I have used in this analysis plotted against the non-resonant spectrum.

I have chosen to make a cut on the candidate $b \to s\gamma$ photon energy in the laboratory frame as a function of $\cos(\theta)$. Figure 4.14 illustrates the bands of this cut on signal, continuum and $b\bar{b}$ events in the laboratory frame. This cut corresponds to a cut on the photon energy in the decaying B meson CM frame which rejects photons

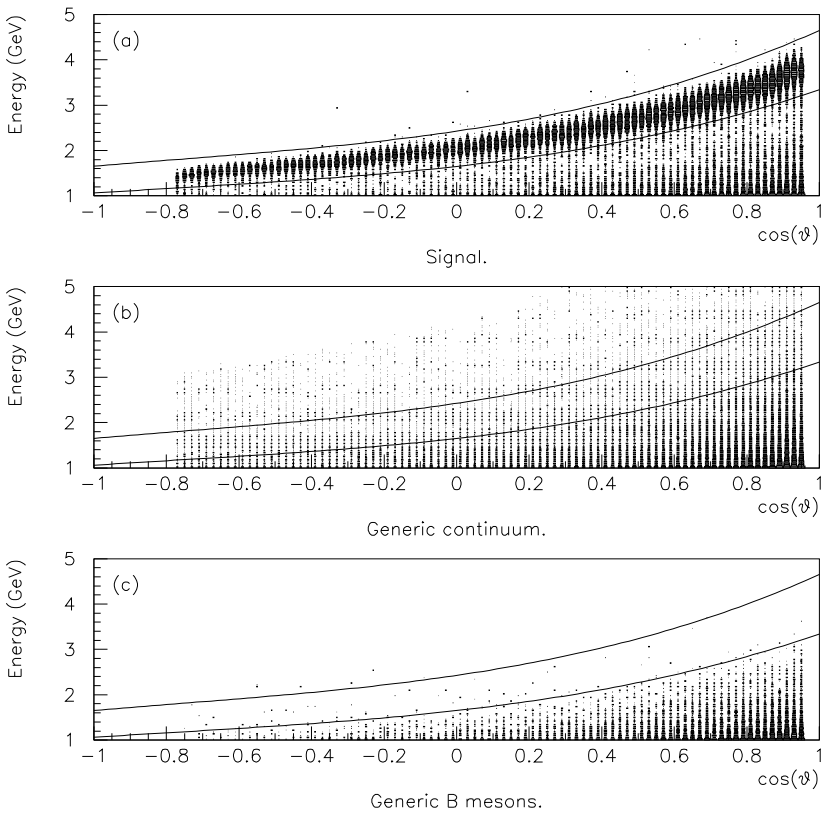

Figure 4.14: Energy vs angle for different exclusive modes for (a) signal (b) continuum and (c) $b\overline{b}$ events.

with energies outside of the region, 2.0 GeV to 2.7 GeV. Theoretical predictions suggest that a lower energy cut of 2.0 GeV, should not reject more than 10% of inclusive $b \to s\gamma$ events. If detector effects were neglected all the signal photons from the exclusive modes considered in this analysis would be accepted using this cut. The efficiencies for the energy cuts are listed in table 4.2, where cut efficiency is defined to be the ratio of the number of events remaining after the cut to the number of events before the cut was applied. Therefore the usefulness of the cut is indicated by a high efficiency value for signal and a low value for background.

	No. candidates before cut.	No. candidates after cut.	Cut efficiency.
$K^*(892)\gamma$	10000	7695	0.77
$K_1(1270)\gamma$	10000	7631	0.76
$K^*(1400)\gamma$	9033	6853	0.76
$K_2(1430)\gamma$	10000	7559	0.76
Total signal	39034	29738	0.76
$b\bar{b}$	50000	86	0.17×10^{-2}
Merged π^0's	20532	2520	0.12
Unmerged π^0's	68876	4300	0.62×10^{-1}
ISR	3900	950	0.24
η's	9866	1099	0.11
Other	5473	449	0.82×10^{-1}
Total continuum	200000	9318	0.47×10^{-1}

Table 4.2: Efficiencies of energy-angle cut.

4.4.3 Merged π^0 rejection.

The next stage of the photon selection procedure is to eliminate the merged π^0 background. It is possible to differentiate between photon and merged π^0's by parametrizing the energy distribution of the calorimeter clusters. A variety of parametrizations can be employed, however the method of second moments proved to be a very powerful discriminator. In the method of second moments each cluster is parametrized by equation 4.2, where S is the second moment, E_i is the energy deposited in crystal i and $\underline{R_i}$ is the vector from the centroid of the cluster $\underline{\mathrm{O}}$, to the centre of crystal r_i. The centroid of the cluster is given by equation 4.4, where x_{ij} is the component j, of the vector from the origin to crystal i.

$$S = \frac{\sum_i E_i \cdot \underline{R_i}^2}{\sum_i E_i} \tag{4.2}$$

$$\underline{R_i} = \underline{r_i} - \underline{O_i} \tag{4.3}$$

$$\underline{O} = \left(\frac{\sum_i E_i x_{ij}}{\sum_i E_i} \right) \underline{\hat{x}}_j \tag{4.4}$$

Essentially this parametrization is a measure of how the deposited energy is distributed about the cluster maximum.

Figure 4.15 shows the second moment distributions for (a) signal (b) continuum

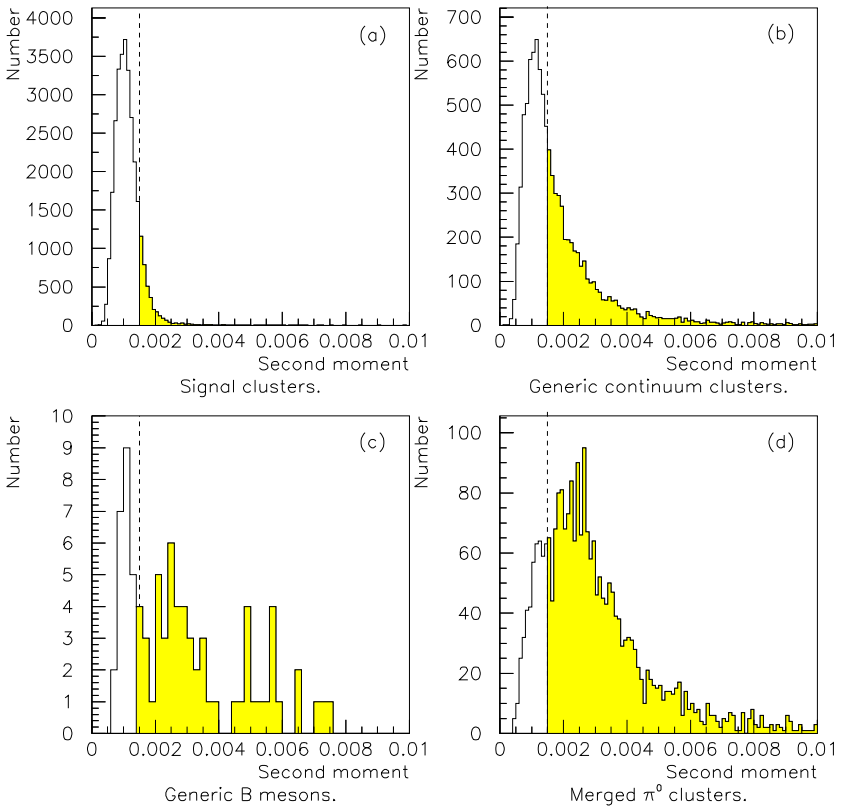

Figure 4.15: Second moment distributions.

background, (c) $b\overline{b}$ background and (d) the merged π^0 contribution to the continuum background. The distributions clearly show the discriminating power of this variable. All events with a second moment value greater than 0.0015 were eliminated. The shaded grey area in the plots indicates the events removed by this cut, this convention is used throughout the rest of this document. Table 4.3 shows the cut efficiency for the events of interest.

As intended the merged π^0 contribution is significantly reduced. In the case of merged π^0's originating from the continuum, the contribution is reduced by more than 80%.

	No. candidates before cut.	No. candidates after cut.	Cut efficiency.
$K^*(892)\gamma$	7695	6715	0.87
$K_1(1270)\gamma$	7631	6682	0.88
$K_1(1400)\gamma$	6853	5954	0.87
$K_2(1430)\gamma$	7559	6592	0.87
Total signal	29738	25943	0.87
$b\bar{b}$	86	25	0.29
Merged π^0s	2520	462	0.18
π^0s	4300	2509	0.58
η	1099	917	0.83
ISR	950	839	0.88
Other	449	269	0.60
Total continuum	9318	4996	0.54

Table 4.3: Efficiencies of second-moment cut at 0.0015

4.4.4 π^0 rejection.

High energy photons originating from the decays of π^0 and η represent a major source of background to $b \to s\gamma$. π^0's decay $\sim 99\%$ of the time to two photons, η's $\sim 39\%$ of the time. These backgrounds make up a considerable proportion of both the continuum and $b\bar{b}$ backgrounds.

In order to reduce the π^0 contribution of this background, candidate π^0s are constructed by combining pairs of the candidate $b \to s\gamma$ photon and each of the other photons in the event. The candidate π^0 with the best mass, i.e with a mass closest to the mass of a real π^0, is selected for each candidate photon.

Figure 4.16 shows the mass distributions of the candidate π^0s for (a) signal (b) continuum background, (c) $b\bar{b}$ background and (d) from the π^0 contribution to the continuum background.

There is a clear π^0 mass peak in the background distributions which is not present in the signal distribution. The actual π^0 mass is $\sim 0.135\ GeV/c^2$. All events with a candidate π^0 mass within the region 0.10 - 0.15 GeV/c^2 were rejected. Table 4.4

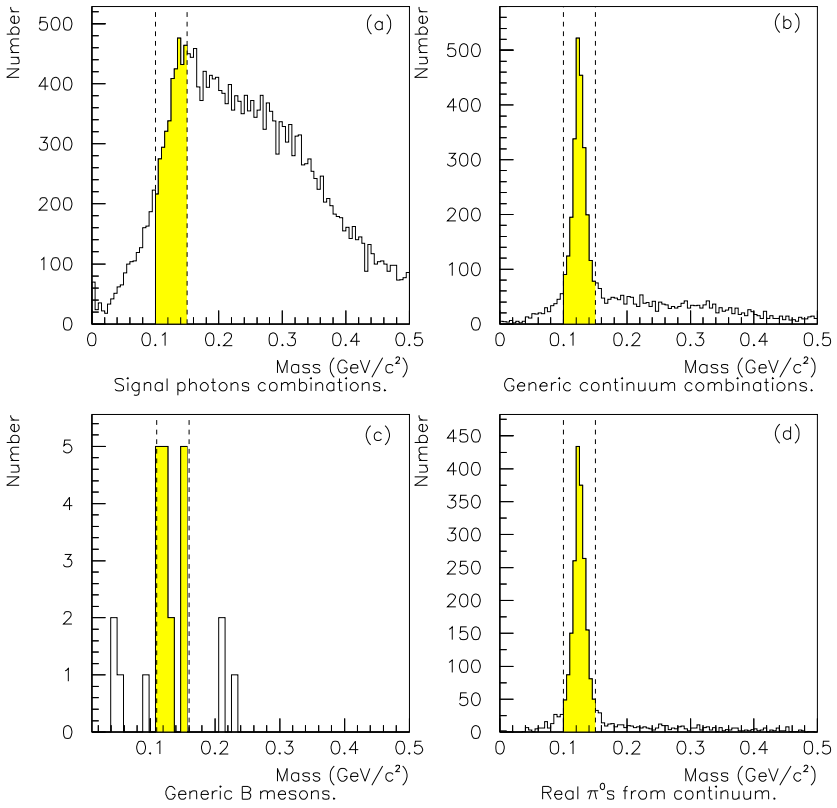

Figure 4.16: Mass spectrum of candidate π_0s.

shows the cut efficiency for the events of interest.

This cut not only significantly reduces the π^0 contribution, in the continuum case by $\sim$ 75%, it also reduces the remaining merged π^0 contribution by $\sim$ 50%. This most likely due to the fact that there are often low energy photons present in each event.

In an attempt to reduce the η contribution the same method was tried, constructing the best mass candidate η for each event. Figure 4.17 shows the mass distributions of the η candidates for (a) signal (b) continuum background, (c) $b\overline{b}$ background and (d) from the η contribution to the continuum background.

Comparing the signal and background distributions it is quite clear that this method

	No. candidates before cut.	No. candidates after cut.	Cut efficiency.
$K^*(892)\gamma$	6715	5773	0.86
$K_1(1270)\gamma$	6682	5747	0.86
$K_1(1400)\gamma$	5954	5132	0.86
$K_2(1430)\gamma$	6592	5641	0.86
Total signal	25943	22293	0.86
$b\bar{b}$	25	12	0.48
Merged π^0s	462	205	0.44
π^0s	2509	602	0.24
η	917	784	0.85
ISR	839	763	0.91
Other	269	200	0.74
Total continuum	4996	2554	0.51

Table 4.4: Efficiencies of π^0 mass cut.

	No. candidates before cut.	No. candidates after cut.	Cut efficiency.
$K^*(892)\gamma$	5773	1807	0.31
$K_1(1270)\gamma$	5747	1714	0.30
$K_1(1400)\gamma$	5132	1482	0.29
$K_2(1430)\gamma$	5641	1652	0.29
Total signal	22293	6655	0.30
$b\bar{b}$	12	2	0.17
Merged π^0's	205	84	0.41
π^0s	784	248	0.36
η	602	215	0.33
ISR	763	64	0.82×10^{-1}
Other	200	52	0.26
Total continuum	2554	663	0.26

Table 4.5: Efficiencies of attempted η mass cut.

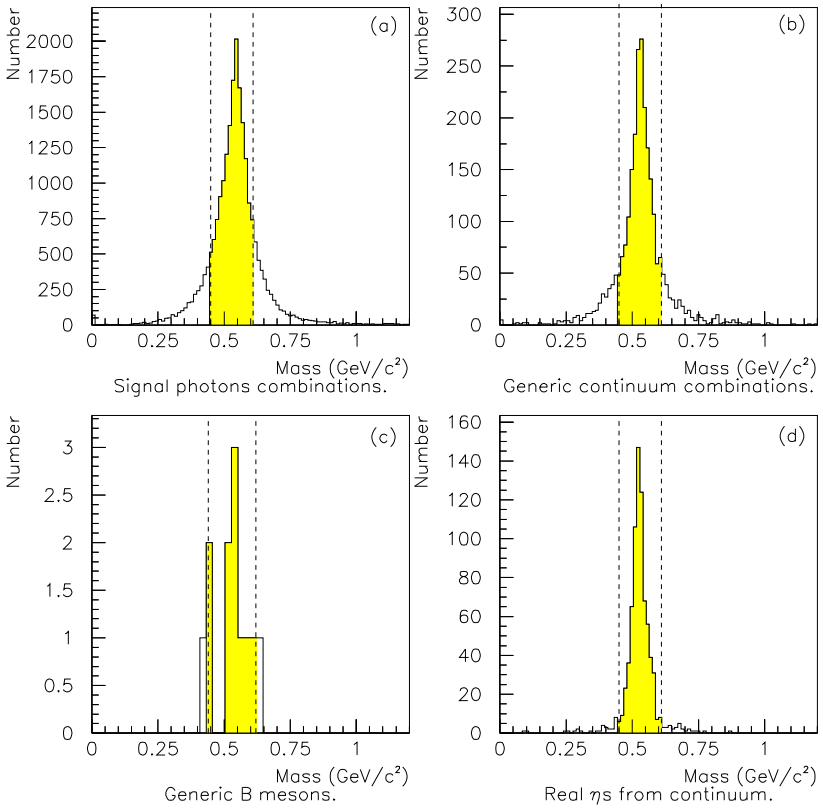

Figure 4.17: Mass spectrum of η candidates.

provides little or no discrimination for η's. This can be explained by the fact that multiplicity of neutrals in signal events is large enough such that there is a high probability of finding a neutral with an energy that when combined with the signal photon candidate reconstructs an η candidate close to the η mass. Table 4.5 shows the efficiencies of a cut between 0.45 and 0.61 GeV/c^2 about the η mass peak, similar to the cut made to the π^0 distribution.

Although there is a significant rejection of $b\overline{b}$ background, there is very little difference between the discrimination efficiencies of signal and continuum background events. As the $b\overline{b}$ background has already been significantly reduced by the other cuts, the η mass cut serves no practical purpose and therefore has not been employed in this analysis.

	No. candidates before cut.	No. candidates after cut.	Cut efficiency.
$K^*(892)\gamma$	10000	5773	0.57
$K_1(1270)\gamma$	10000	5747	0.57
$K_1(1400)\gamma$	9033	5132	0.57
$K_2(1430)\gamma$	10000	5641	0.56
Total signal	39033	22293	0.57
$b\bar{b}$	50000	12	0.24×10^{-3}
Merged π^0s	20532	205	0.10×10^{-1}
π^0s	68878	598	0.87×10^{-2}
η	9866	784	0.79×10^{-1}
ISR	3900	763	0.20
Other	5473	200	0.37×10^{-1}
Total continuum	200000	2550	0.13×10^{-1}

Table 4.6: Total efficiencies for photon selection.

4.4.5 Summary.

The photon selection procedure significantly reduces both continuum and generic $b\bar{b}$ backgrounds. However the continuum background is still significant at this stage. In the next chapter further techniques are demonstrated to further reduce the continuum background. Table 4.6 lists the efficiencies for the photon selection procedure for all types of events.

Figure 4.18 shows the efficiencies for the acceptance of signal events by the photon selection cuts, as a function of the mass of X_s. The graph does not show an obvious correlation between the photon selection efficiency and the mass of X_s, which implies that the efficiency for inclusive $b \to s\gamma$ is not biased by the particular choice of exclusive modes used for this analysis.

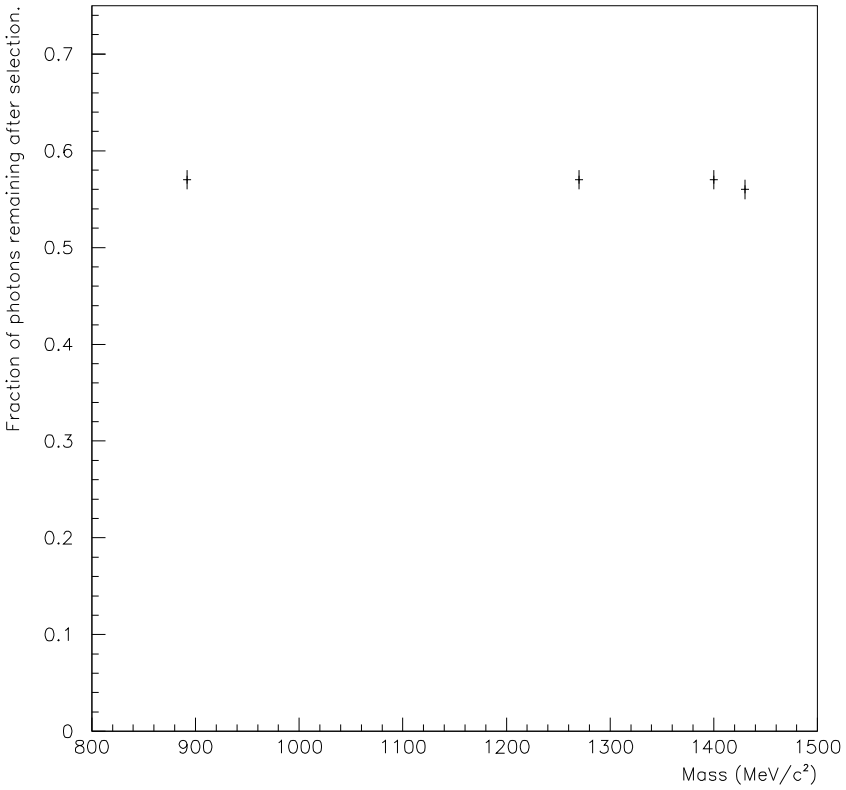

Figure 4.18: Number of signal events against mass of kaon resonance.

Chapter 5

Methods to suppress the continuum backgrounds.

5.1 Introduction.

At the end of the initial photon selection procedure, continuum events remain as the major source of background to $b \to s\gamma$ processes. This section describes the techniques I have used in an attempt to further reduce the continuum backgrounds. Two different schemes are used to achieve this aim and their effectiveness compared. The first scheme involves a partial reconstruction of the candidate events, where an attempt is made to reconstruct a signal B candidate. The degree of success of the reconstruction determines whether or not the event is accepted or rejected. The second scheme uses event shape variables to discriminate between signal and continuum background, these variables are combined to form a single discriminating variable, the value of which determines the fate of the event in question.

5.2 Reconstruction Analysis.

The first method I investigated, attempts a reconstruction of the parent B meson using the candidate $b \to s\gamma$ photon and a combinations of kaons and pions present in the event. The possible final states of an inclusive $b \to s\gamma$ process are varied due to the fact that different exclusive modes and non-resonant $b \to s\gamma$ events must be considered. For this reason, the approach of combining daughter candidates, back through the decay cascade, in a deliberate manner to reconstruct the B meson is

not practical. All that can be said with certainty about the final states of $b \to s\gamma$ events, is that they largely consist of charged kaons and a varying number of pions.

The reconstuction method considered here, instead proceeds by combining the candidate photon with a kaon and varying numbers of pions, to produce multiple composite particles, each of which is then treated as a candidate signal B meson.

Firstly a list of kaons is constructed. The charged kaons are selected by taking the list of all the charged tracks identified by the DIRC as most likely to be kaons. Neutral kaons candidates are selected by combining all the negative and positive charged pions in each event and selecting only those composite products with a mass between 0.45 and 0.55 GeV/c^2. The decay mode $K^0_S \to \pi^+\pi^-$ is the most dominant decay mode for K^0_S with a branching ratio $\simeq 2/3$, which motivates the above procedure. The other dominant mode for neutral kaons is of course $K^0_S \to \pi^0\pi^0$. For the purpose of this analysis neutral kaons decaying through $K^0_s \to \pi^0\pi^0$ were not considered, the justification being that in order to reconstruct this kaon channel, one must first also reconstruct the neutral pions themselves increasing the number of possible combinations of particles, if the number of combinations were completely unrestricted the chances of getting a candidate B meson would be high, whether one was dealing with signal or background. K^0_L mesons have also been ignored because of the difficulty identifying them.

The list of kaons produced is then combined with a combination of one to four pions, a maximum of one of which could be a π^0, to produce the list of candidate B mesons. The charge on the composites is restricted to the values $+1$, 0 and -1 which are the possible charges of a B meson.

$$\chi^2 = \frac{(M_B - m_{cand})^2}{\sigma^2_m} - \frac{(E_{beam} - E_{cand})^2}{\sigma^2_E} \tag{5.1}$$

For each event the value of χ^2, expressed in equation 5.1, is evaluated for each B

candidate in the generated list. The most consistent candidate B meson (the candidate with lowest χ^2) was then selected from each event. The χ^2 was evaluated in the $\Upsilon(4s)$ CM frame, where M_B is the B meson mass of 5.28 GeV/c^2, m_{cand} is the mass of the candidate parent B meson, E_{beam} is the CM beam energy and E_{cand} is the energy of the candidate B. The width of the reconstructed mass distribution, σ_m and the width of the energy distribution σ_E are practically identical, therefore both are set to one when evaluating the χ^2.

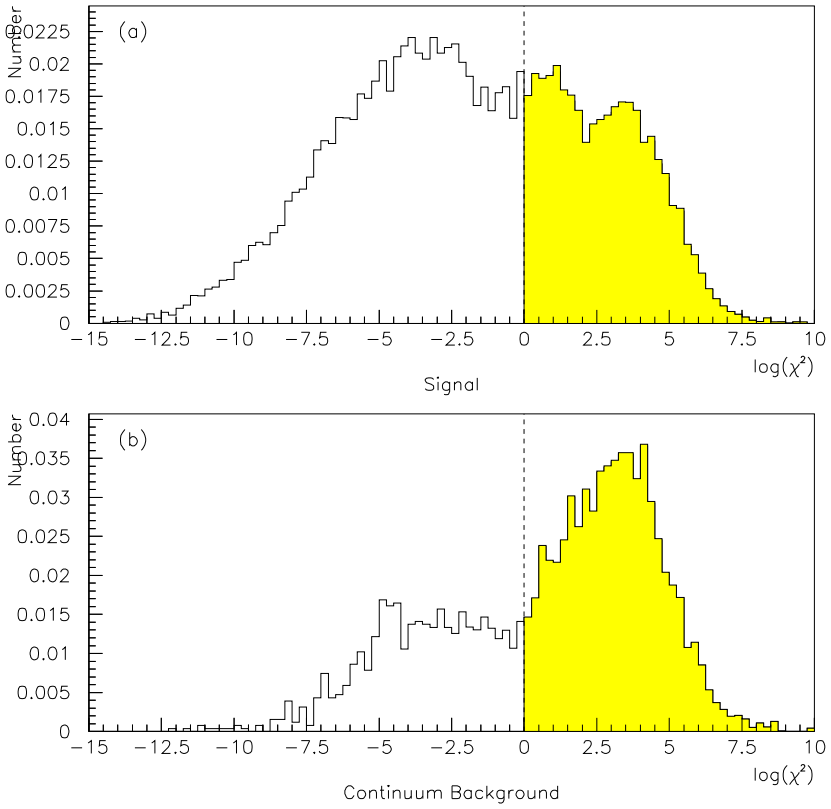

Figure 5.1: Distributions of $\log(\chi^2)$ for (a) signal and (b) generic continuum events.

The distributions for $\log(\chi^2)$ are plotted in figure 5.1.(a) for signal events and 5.1.(b) for continuum events. A cut was then applied to these distributions, selecting only the events where a B meson candidate had a value for χ^2 of less than one. As the number of continuum events is much larger than the number of signal events the

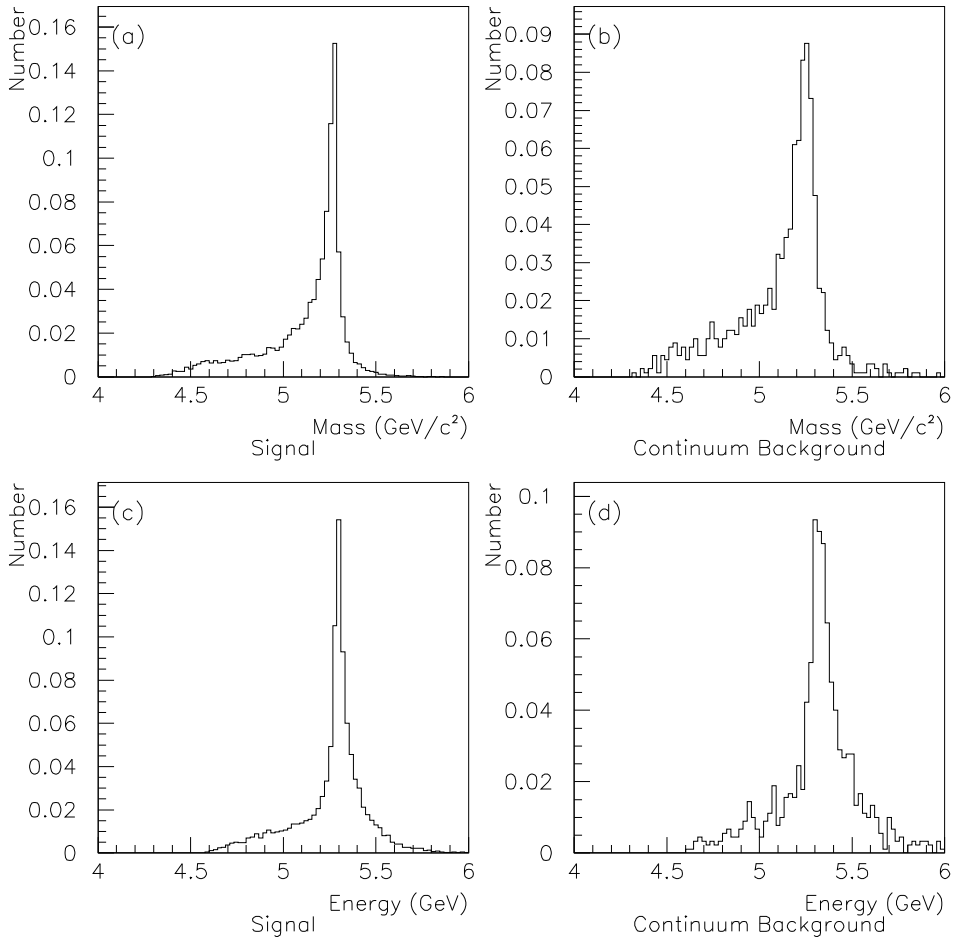

Figure 5.2: Mass distributions of selected candidate B mesons from (a) signal and (b) generic continuum events and energy distributions for (c) signal and (d) background.

ratio of the number of signal to the standard deviation, R_{sb} is approximated by equation 5.2. The cuts used in this chapter aim to optimize the ratio of R_{sb}, this is done by finding the cut that optimizes the value of equation 5.3, where E_f is the cut efficiency.

$$R_{sb} = \frac{N_{Signal}}{N_{Background} + N_{Signal}} \simeq \frac{N_{Signal}}{N_{Background}} \tag{5.2}$$

$$\text{Cut optimization value } = \frac{E_{fSignal}}{\sqrt{E_{fBackground}}} \propto \frac{R_{After}}{R_{Before}} \tag{5.3}$$

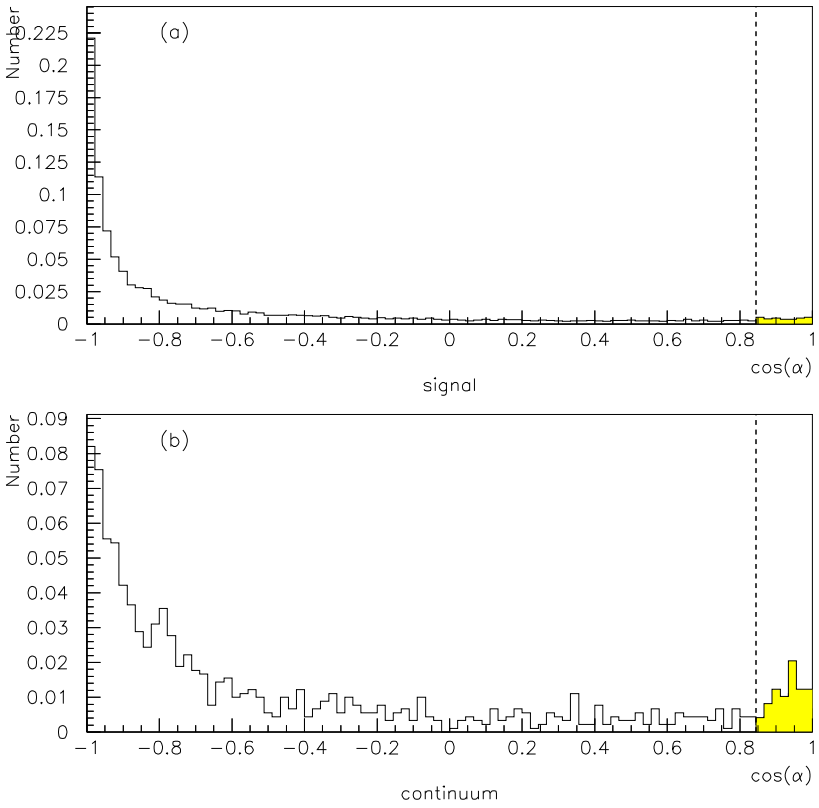

Figure 5.3: Distributions for cos α for selected B meson candidates from (a) signal and (b) generic continuum events.

The efficiencies for the cuts on the χ^2 distribution are summarized in table 5.1.

Event type.	Cut range.	No. candidates before cut.	No. candidates after cut.	Efficiency.
Signal	0.0 - 15.0	22293	14205	0.64
Continuum Background	0.0 - 15.0	2550	902	0.35

Table 5.1: Efficiencies for reconstruction analysis cut.

The mass distributions of the candidate B mesons from the selected events are plotted in figure 5.2.(a) for signal events and 5.2.(b) for continuum events. As expected the distributions peak sharply at the B mass.

The cosine of the angle α between the composite X_s and the candidate photon in

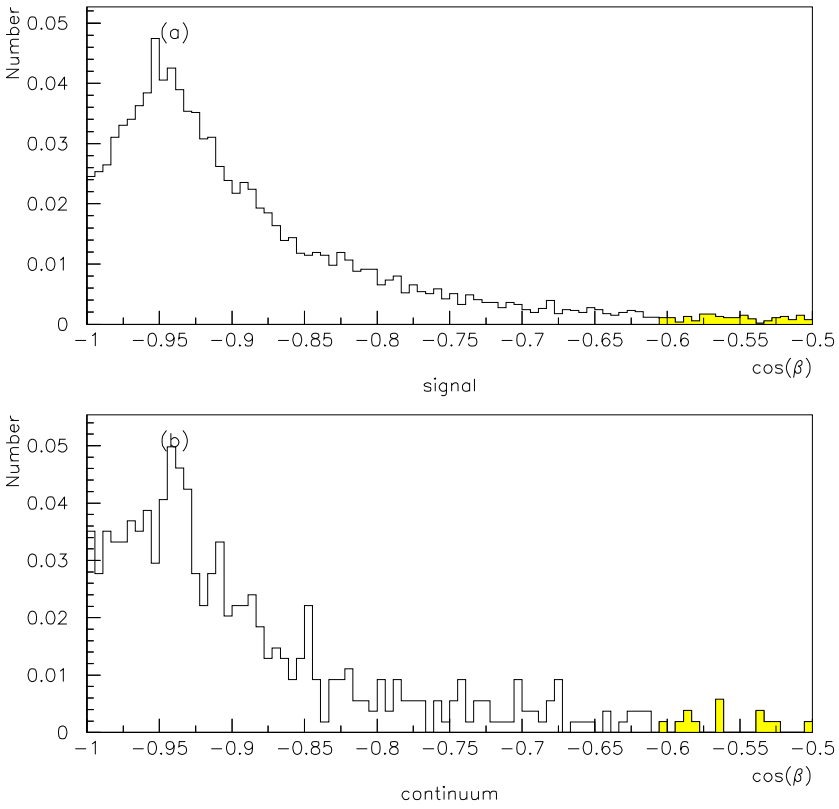

Figure 5.4: Distributions for cos β for selected B meson candidates from (a) signal and (b) generic continuum events.

the CM of the B meson are also shown in figures 5.3.(a) and 5.3.(b). As expected cos α tends to -1, as the pair should be back to back in this frame as demanded by the conservation of momentum. A cut was also attempted on this distribution, however the optimial cut, excluding events with cos α greater than 0.87 indicated in the figure, showed no marked improvement in discriminating signal events from background.

The final reconstruction analysis plot, figure 5.4, shows the distributions for cos β the cosine of the angle between the candidate B and the composite product of all the particles remaining in the event in the Υ(4s) CM frame, for (a) signal and

(b) background. As before these products should also be back-to-back in the frame considered, which is reflected in the plot shown. Unfortunately, cutting on this distribution also proved to be ineffective, the optimal cut excluding all events greater than -0.6 is also indicated in the figure had little discriminating power.

5.3 Combined event-shape variable analysis.

A property of an event that is often exploited to discriminate between signal and

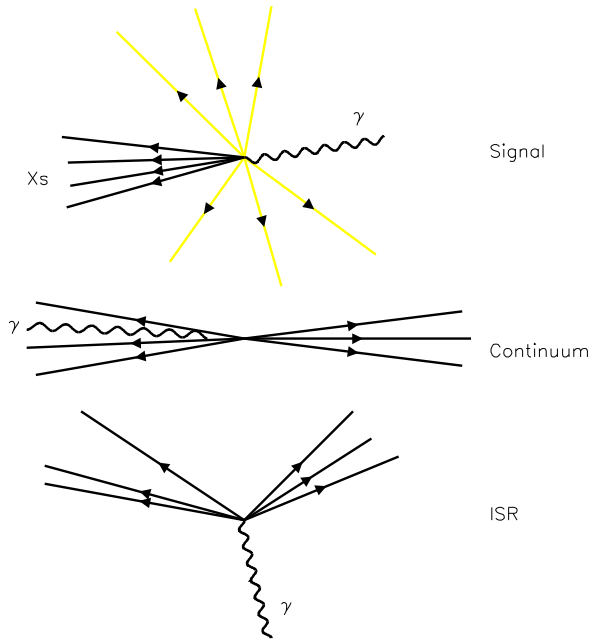

Figure 5.5: Illustration of the different event morphologies in the CM frame.

background is the event's morphology. The morphologies of $b \to s\gamma$ processes and continuum events are distinct and this can be taken advantage of. Figure 5.5 illustrates the signal and background event morphologies in the CM frame of the $\Upsilon(4s)$.

The signal $b \rightarrow s\gamma$ events have a characteristically spherical morphology. This results from the fact that in an Υ(4s) event, where two B mesons are produced, the two B mesons have very little residual momentum (due to the small difference in mass between mother and daughters) and decay isotropically, almost immediately after production. In an event where a B meson decays through the $b \rightarrow s\gamma$ process, the signal photon is back to back with the hadronizing X_s product. The other B meson present in the event decays to a random final state which is superimposed on top of the signal in the CM frame.

Amongst the continuum backgrounds, ISR events have a morphology distinctive from the other types of events that constitute this background. The morphology of non-ISR continuum events is simply that of back to back jets of hadronizing quarks, which are produced as a consequence of the substantial amount of residual energy remaining after the creation of u, d, s, c quark pairs. The photon candidate is typically found within either of the jets.

The morphology of Initial State Radiation events is a combination of a photon and two skewed jets. The ISR photon recoils against the two hadronizing u, d, s, c jets to produce this effect. The angle between the jets is dependent on the energy of the radiated photon. For the candidate events that remain after the photon selection procedure, the angle tends to be large enough to make the morphology distinct from non-ISR continuum events.

5.3.1 Event-shape variables.

Event-shape variables are discriminating tools which are used to exploit differences in the morphologies of signal and background events. Event shape variables provide a measure of a certain characteristic of the morphology of an event.

In this section the different event-shape variables used in this analysis are introduced. The aspect of the event morphology from which each event-shape variable derives its discriminating power is described and the usefulness of the variable is

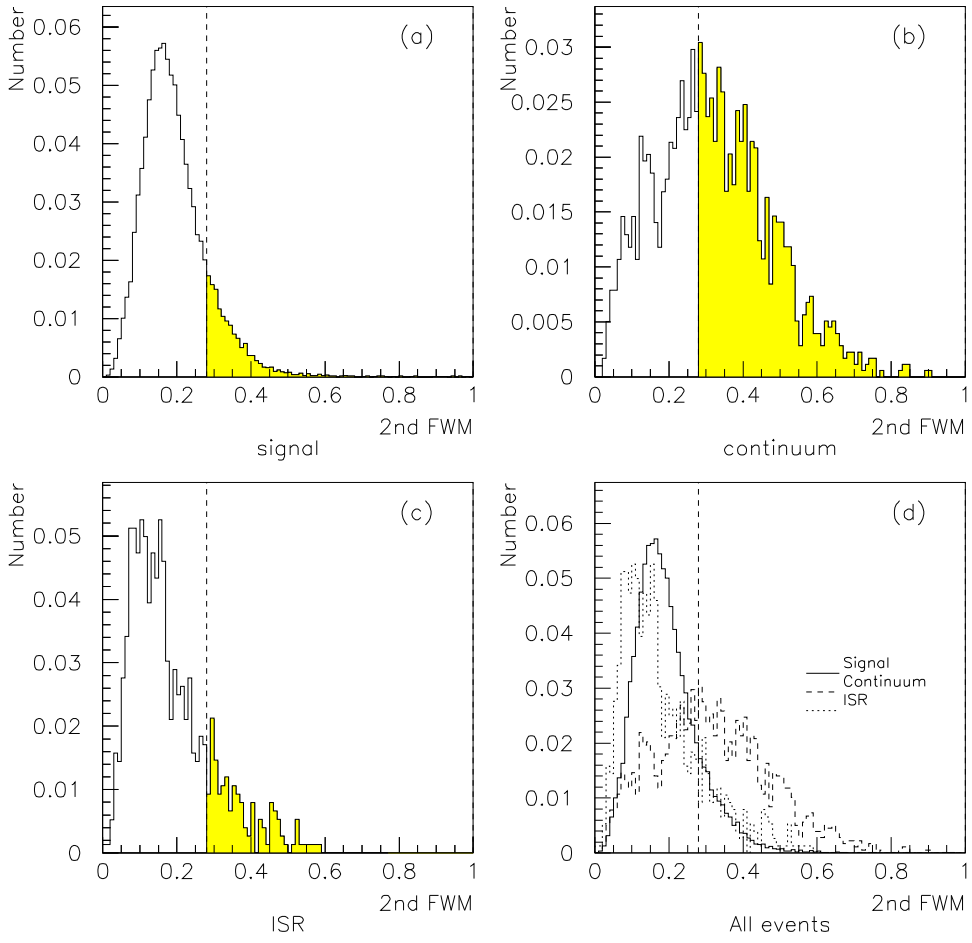

Figure 5.6: Distributions of the 2nd FWM for (a) signal (b)continuum (c) ISR (d) signal and background events.

demonstrated by applying simple cuts to the signal and background data samples. The event-shape variables are then combined to form a single discriminating variable and which the final cuts are performed.

When attempting an analysis of this type all event shapes are best evaluated after Lorentz boosting them into the CM frame, as the BaBar boost make matters complicated when attempting to apply an event shape analysis in the laboratory frame.

5.3.2 The Second Fox-Wolfram Moment (2nd FWM).

The general definition of the Fox-Wolfram moment is given by the following equation[22],

$$H_l = \left(\frac{4\pi}{2l+1}\right) \sum_{m=-l}^{+l} \left[\sum_i^N Y_l^m(\Omega_i) \frac{|\underline{p_i}|}{E_{tot}}\right]^2 \tag{5.4}$$

The Fox-Wolfram moments are constructed from the momentum vectors of the final state particles, $\underline{p_i}$. The spherical harmonics Y_l^m, characterized by the integers l and m, also need to be evaluated and require a choice of axes, $\Omega_i = (\theta_i, \phi_i)$, although the final result is coordinate independent. In the case of the 2nd FWM, l is set to two.

The role of the 2nd FWM is to give a measure of how jet like an individual event actually is. The 2nd FWM tends to zero for spherical events and tends to one for events that are more jet-like. Figure 5.6 shows the 2nd FWM distributions for signal, generic continuum and ISR events. The signal and generic continuum distributions are clearly distinguishable, whereas the signal and ISR events appear very similar. To illustrate the effectiveness of this variable, the optimum cut to maximize 5.3 is indicated in the figures, excluding events in the range 0.28 - 1.0. Table 5.2 lists the efficiencies for this cut for the different event types.

	No. candidates before cut.	No. candidates after cut.	Efficiency.
Signal	22293	19164	0.86
Generic continuum	1787	768	0.43
ISR	763	629	0.82
Total Background	2550	1397	0.55

Table 5.2: Efficiencies of 2nd FWM cut for signal and background.

5.3.3 Sum of transverse momentum ($S_\perp$).

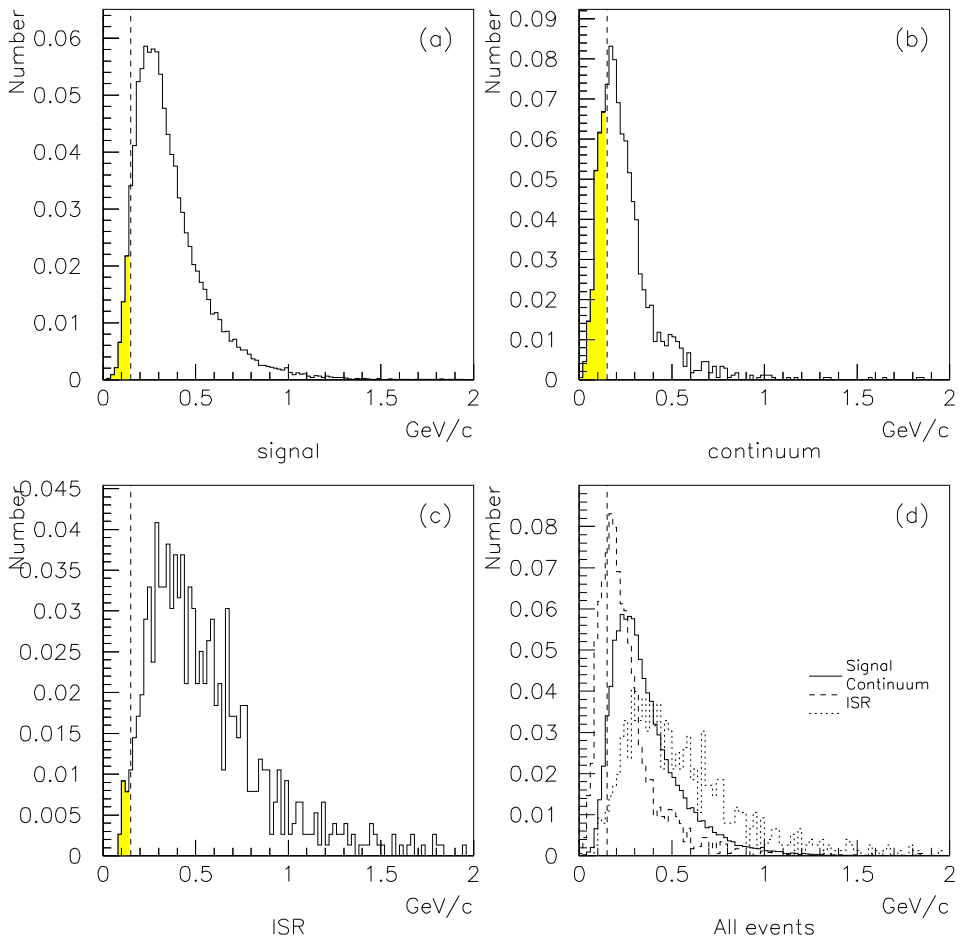

Figure 5.7: Distributions of the sum of transverse momentum for (a) signal (b) continuum (c) ISR (d) signal and background events.

The variable $S_\perp$ is defined by the following equation,

$$S_\perp = \frac{\sum_{\alpha_i>-\pi/8}^{\alpha_i<\pi/8} \left(|\underline{p_i}|\sin(\alpha_i)\right)^2}{\sum_i |\underline{p_i}|} \tag{5.5}$$

where α_i is the angle between the momentum vector, $\underline{p_i}$, of each final state particle and the photon candidate axis. Each final state particle that has a momentum vector within a 45^o cone of the axis is selected and the square of the momentum

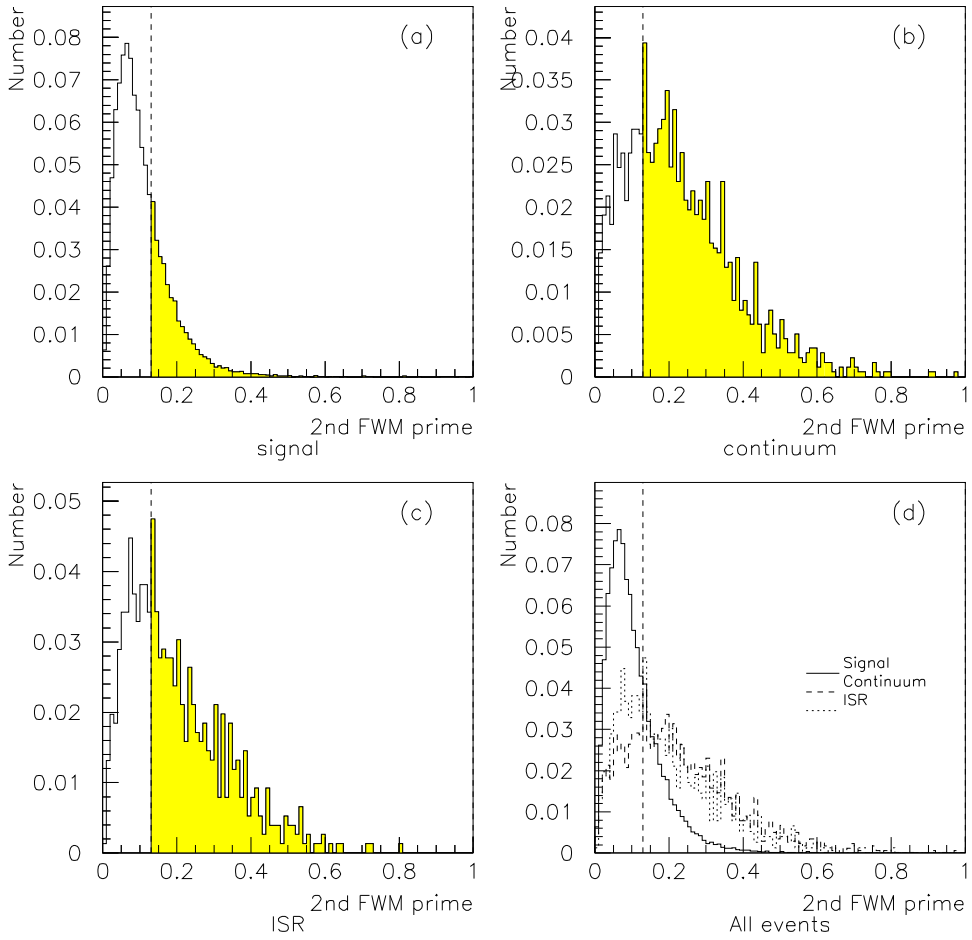

Figure 5.8: Distributions of the 2nd Fox-Wolfram Moment Primed for (a) signal (b) generic continuum (c) ISR (d) signal and background events.

components perpendicular to the axis are summed. The whole expression is divided by the sum of the magnitude of all the final state particles excluding the candidate photon.

The aim of $S_\perp$ is specifically to distinguish between generic continuum and signal events. In continuum jets each particle has a momentum vector that tends to have the majority of its momentum in the component parallel to the direction of the jet, whereas signal events tend not to be so collimated. Figure 5.7 shows the $S_\perp$ distributions for signal, continuum and ISR events. The cut that maximized

5.3 was found to be 0.0 - 0.15 and is shown to demonstrate the effectiveness of this variable. Table 5.3.3 show the efficiencies for the different events types using this cut.

	No. candidates before cut.	No. candidates after cut.	Efficiency.
Signal	22293	21287	0.95
Generic continuum	1787	1390	0.77
ISR	763	748	0.98
Total Background	2550	2138	0.84

Table 5.3: Efficiencies of transverse momentum cut for signal and background.

5.3.4 The Second Fox-Wolfram Moment evaluated in the recoil frame.

The 2nd FWM has already been demonstrated as a useful tool to discriminate against non-ISR continuum events but was less powerful in distinguishing ISR events from signal. However the 2nd FWM can be reapplied to discriminate against ISR but this time by evaluating it in the frame recoiling against the candidate photon. The reasoning behind this scheme is as follows. In the recoiling frame(or the primed frame) the two jets in an ISR event should no longer be skewed but back to back and would therefore have a 2nd FWM value tending to one. The signal event morphology would also be transformed by the Lorentz boost but not in such a way as to make the events appear cone-like and should still tend to zero.

Figure 5.8 shows the transformed 2nd FWM distributions for signal, generic continuum and ISR events. There is now a clear distinction between both the signal and generic continuum distributions and the signal and ISR distributions are clearly distinguishable. Plot 5.8 also shows that this variable is very powerful in distinguishing signal from non-ISR continuum events. Illustrating the point, the optimimum cut value to maximise 5.3 excludes events in the range 0.13 - 1.0. Table 5.2 lists the cut efficiencies for the different event types using this event shape variable.

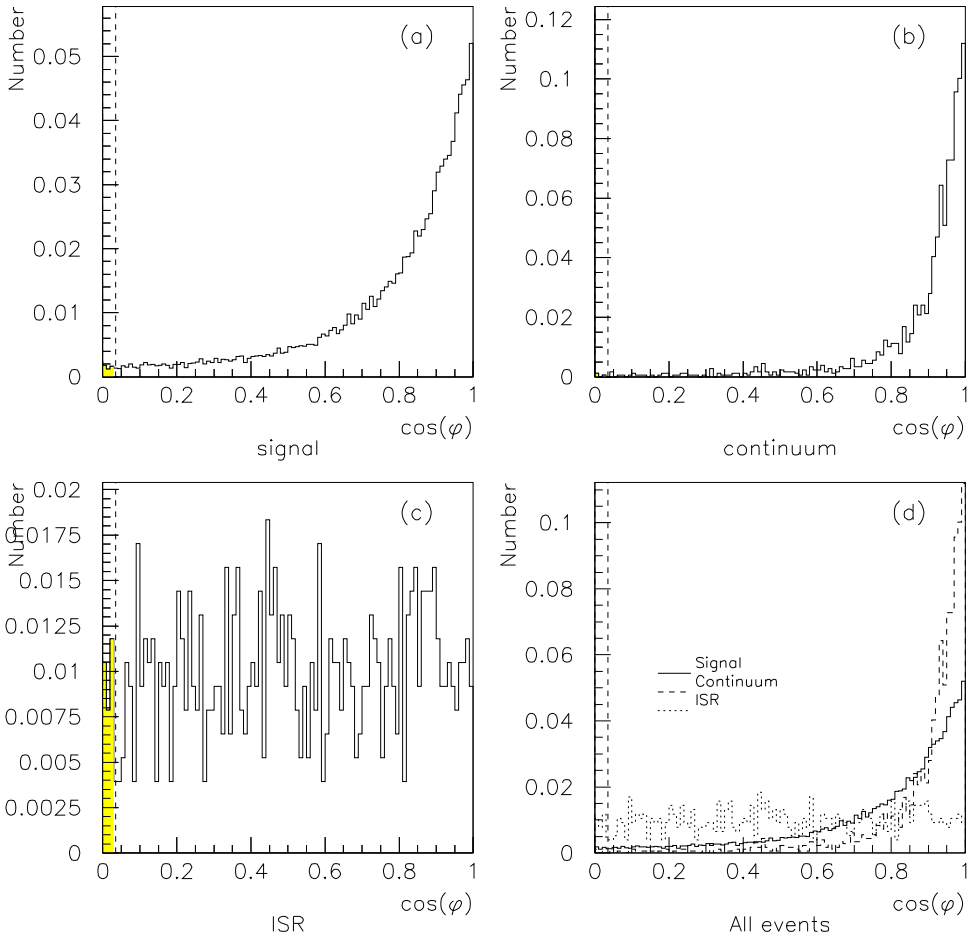

Figure 5.9: Distributions of the cos ϕ for (a) signal (b) generic continuum (c) ISR (d) signal and background events.

5.3.5 Cos ϕ.

This next event shape variable to be applied is defined as the cosine of the angle ϕ, where ϕ is the angle between the candidate signal photon candidate and the thrust axis of the rest of the event in the recoiling frame. The thrust axis is the axis where the value of T in equation 5.6 is maximized.

$$T = \frac{\sum_i |\underline{n} \cdot \underline{p_i}|}{\sum_i |\underline{p_i}|} \tag{5.6}$$

	No. candidates before cut.	No. candidates after cut.	Efficiency.
Signal	22293	15951	0.72
Generic continuum	1787	518	0.29
ISR	763	285	0.37
Total Background	2550	803	0.31

Table 5.4: Efficiencies of 2nd Fox-Wolfram Moment Primed cut for signal and background data samples.

The cos ϕ variable is useful for distinguishing ISR events. It exploits the fact that there should be no correlation between the direction of the photon and the thrust axis of ISR events, as an ISR photon is radiated in a direction totally independent of the direction of the rest of the event. As $b \to s\gamma$ events can be considered as two body decays with the photon recoiling against X_s, superimposed onto another decaying B meson decay, the photon axis should tend to align itself with the thrust axis of the rest of the event.

Figure 5.9 shows that as expected the distribution is remarkably different for ISR events. However using a simple cuts yields almost no discrimination between signal and background, because non-ISR events make up the majority of the remaining background. Table 5.5 shows the efficiencies for a simple cut optimised to maximize 5.3.

	No. candidates before cut.	No. candidates after cut.	Efficiency.
Signal	22293	22189	0.995
Generic continuum	1787	1784	0.998
ISR	763	740	0.970
Total Background	2550	2524	0.990

Table 5.5: Efficiencies of cos ϕ cut for signal and background data samples.

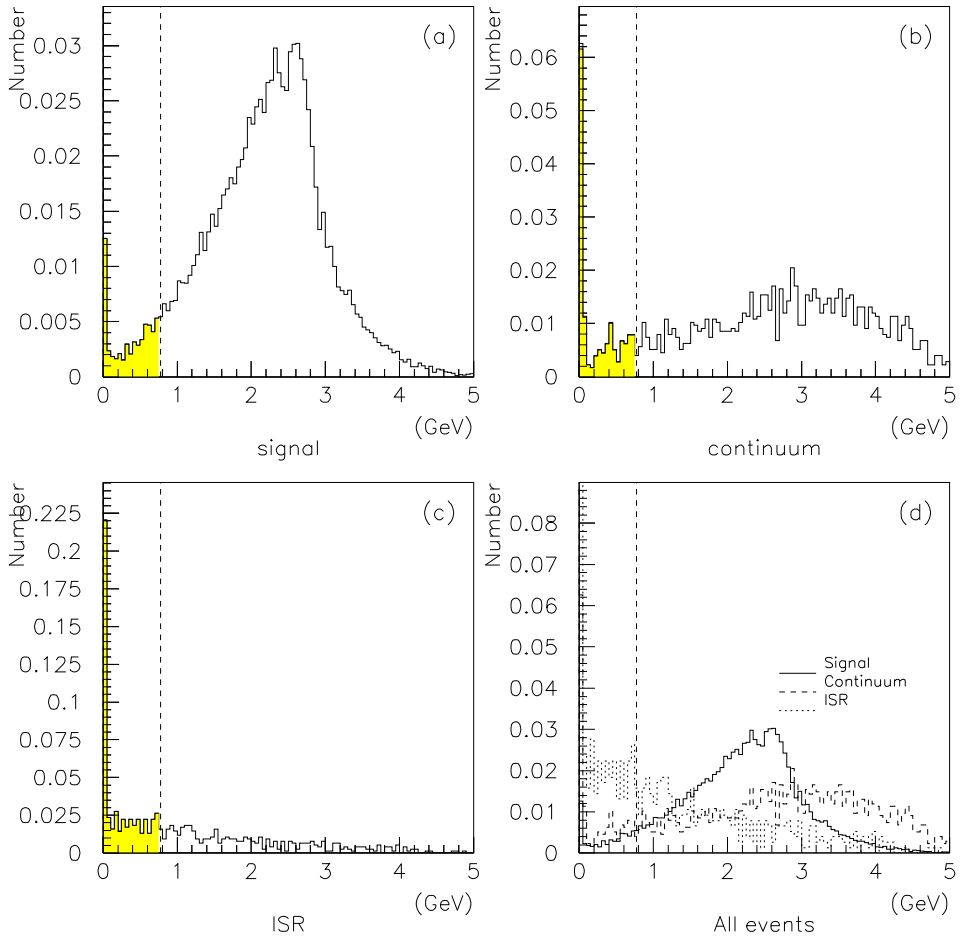

Figure 5.10: Distributions of Energy sum in 45^o cone anti-parrallel to the photon axis, for (a) signal (b) generic continuum (c) ISR (d) signal and background events.

5.3.6 Energy cones.

The energy cones used in this analysis are defined as the sum of the energy of the decay products within a cone around the photon axis, excluding the energy of the candidate photon. I examined cones of varying angles both parallel and anti-parallel to the high energy photon axis. I found that the most powerful discriminator amongst them was a cone of 45^o anti-parallel to the photon axis.

In a continuum event the candidate photons should be contained within a jet whereas in a signal event the signal photon should recoil against X_s. Therefore in the case of

	No. candidates before cut.	No. candidates after cut.	Efficiency.
Signal	22293	21064	0.94
Generic continuum	1787	1532	0.86
ISR	763	381	0.50
Total Background	2550	1913	0.75

Table 5.6: Efficiencies of energy cone cut for signal and background data samples.

cones parallel to the photon direction, one would on average expect a higher value for continuum than signal. For cones evaluated anti-parallel to the candidate photon, signal events should tend to contain more energy because the cone contains the recoiling X_s.

Figure 5.10 shows the distributions for the 45^o cone energy for signal, generic continuum and ISR events. The cut that maximized the signal to background was found to be 0.0 - 0.78. Table 5.6 lists the cut efficiencies for the different event types using this event shape variable.

5.3.7 Correlations.

What has not been mentioned so far is the fact that the event shape variables are correlated to a varying degree. Figures 5.11, 5.12, 5.13 and 5.14 show scatter plots of the different distributions plotted against each other to illustrate the correlations between different event shape variables. One consequence of this fact is that the cuts used above for the purpose of illustrating the discriminating power of each event-shape variable could not be combined with the same discriminating power, as they do not cut on the distributions independently. A simple cuts analysis could be employed at this stage optimizing the combined cut efficiencies through some iterative procedure. However, instead of taking this approach I decided to combine the variables to form a single discriminating variable. One of the motivating factors for this choice was that a cut on a combined distribution, discriminates using the information from all the events-shape variables at the same instance. For example, a signal event may be rejected when applying a cut on one particular event-shape variable but would have not been rejected when cutting on the others, by combining

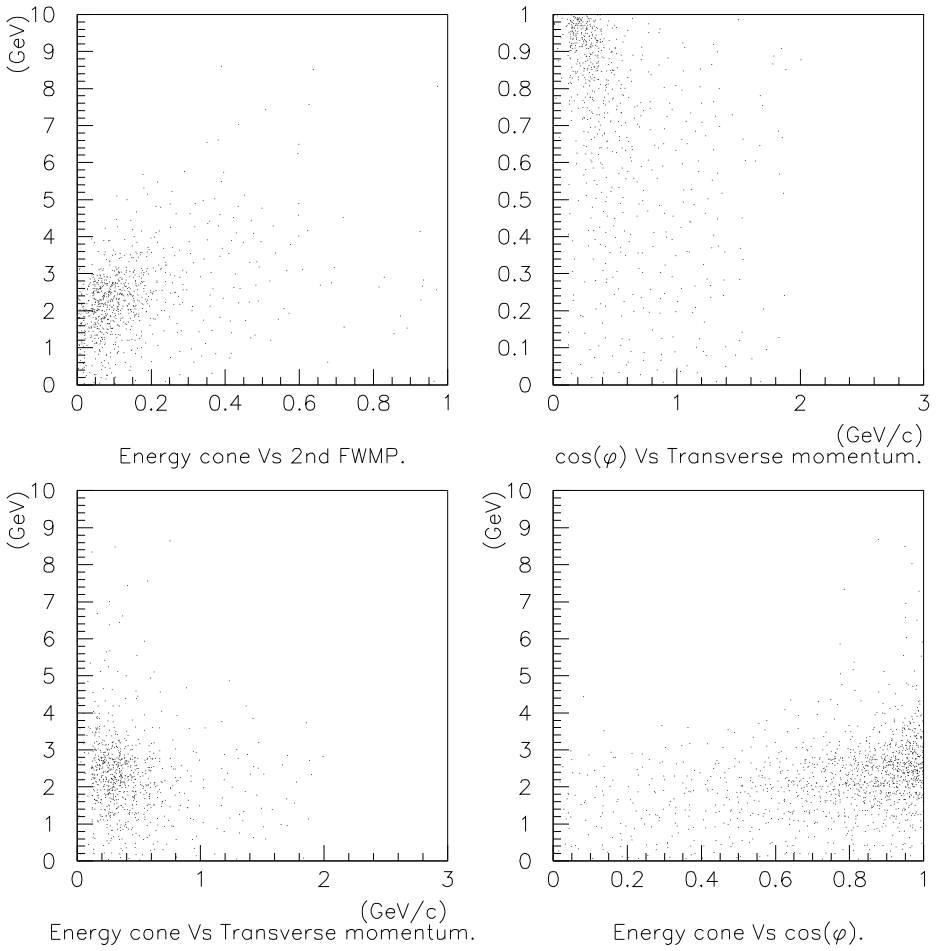

Figure 5.11: Correlations of event-shape variables for signal events.

the variables the weight of the other variables outweighs the single event-shape in disagreement and the event is accepted.

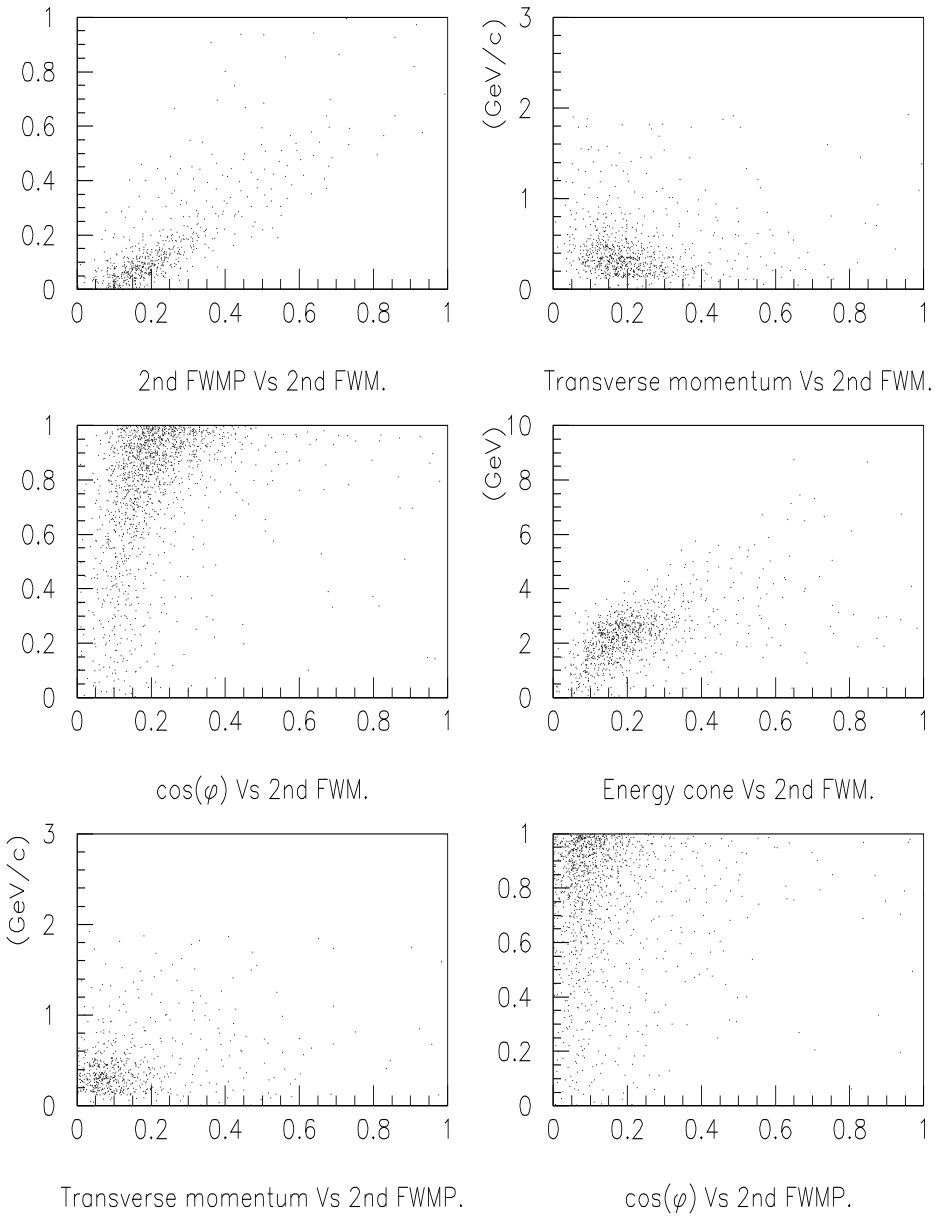

Figure 5.12: Correlations of event-shape variables for signal events.

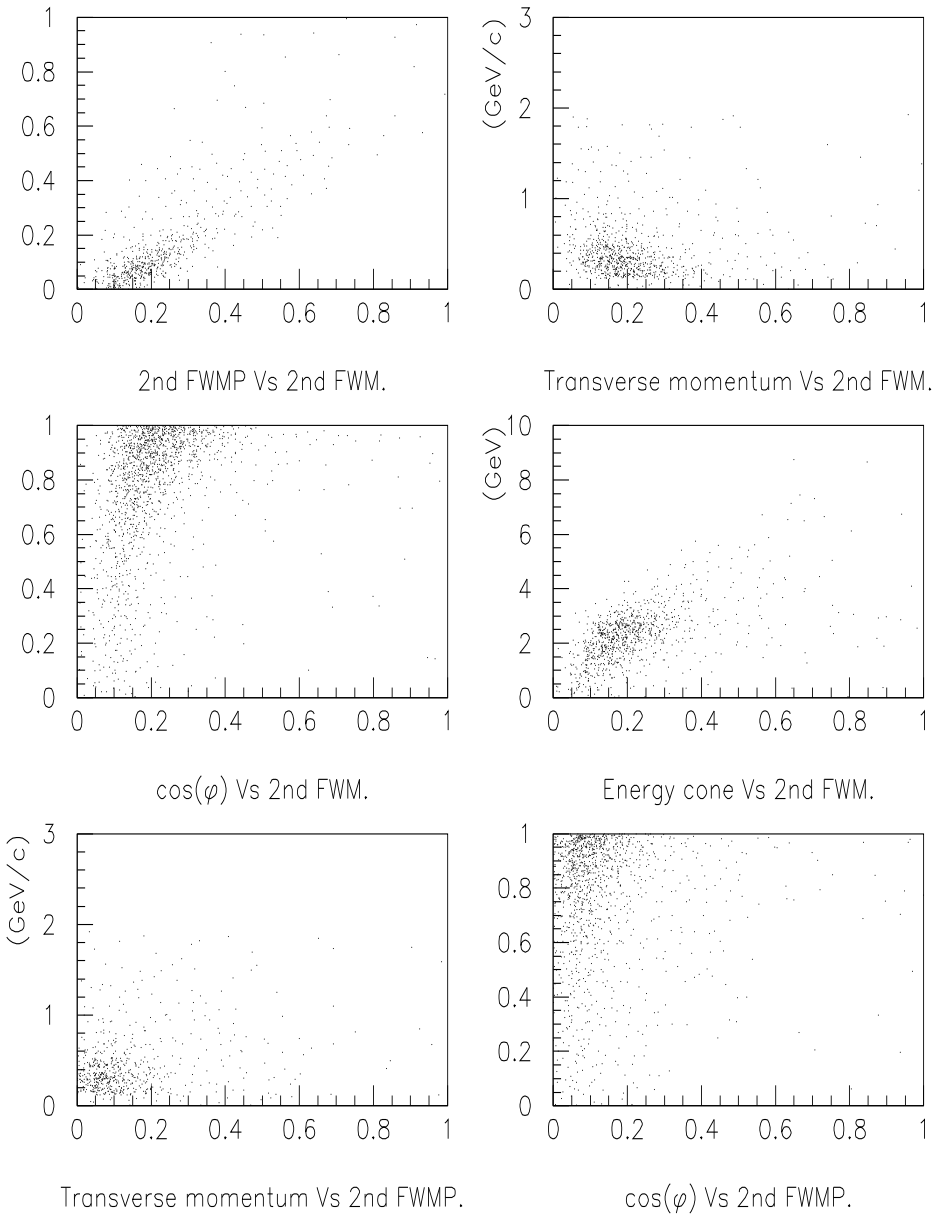

Figure 5.13: Correlations of event-shape variables for continuum events.

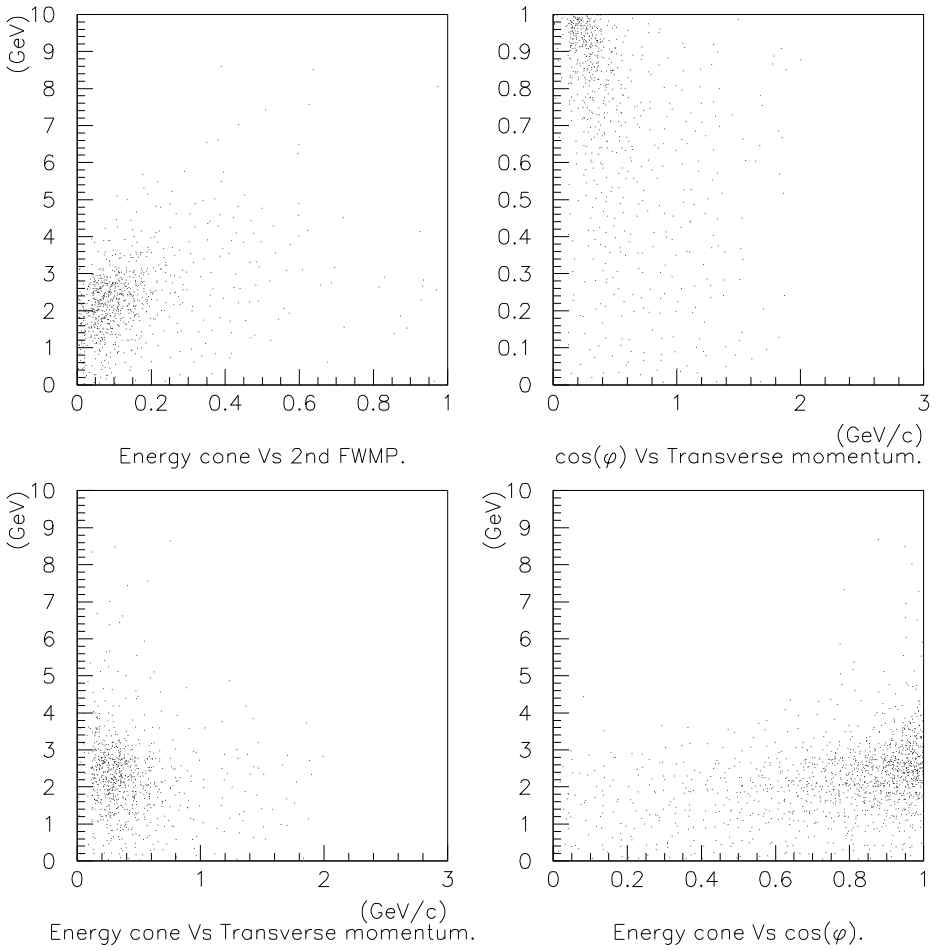

Figure 5.14: Correlations of event-shape variables for continuum events.

5.3.8 Combined discriminator.

The motivation for attempting this method, was to try and utilise the fact that although some of the event shape variables were very different for signal and background, a simple cut on the distributions did not always take full advantage of these differences.

The method proceeds by giving each candidate event a weight according to the values for each of the event shape variables considered. The justification for the value of the weight assigned to each event is the following. Given an event that has

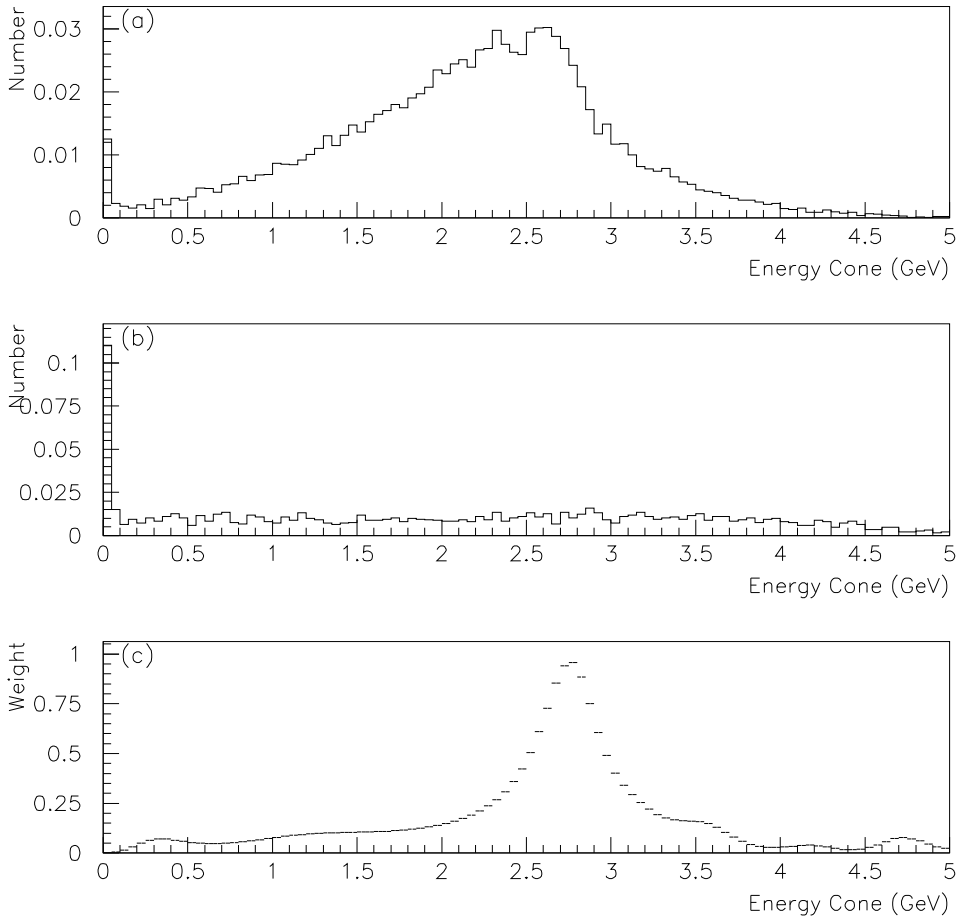

Figure 5.15: Energy cone event shape distribution for signal (a) and for continuum (b). Plot (c) shows the weight given to each energy point.

passed the photon selection procedure and has values x_i for each of the X_i event shape variables measured for that event, there is a certain probability that it is signal and a certain probability that it is background. The probability is described by the Bayesian equation 5.7,

$$P(signal|X_i = x_i) = \frac{P((X_i = x_i)|signal)P(signal)}{P(X_i = x_i)} \tag{5.7}$$

where $P(signal|X_i = x_i)$ is the probability that the event is a signal event, given that the value x_i has been measured for event shape variable X_i. $P(X_i = x_i|signal)$

is the probability of measuring the value x_i for the event shape variable X_i, given that the event is a signal event. $P(signal)$ is the probability of measuring a signal event and $P(X_i = x_i)$ is the probability of measuring an event, either signal or background, with a value of x_i for event shape variable X_i.

The weight given to each event is a reflection of this probability. If the event has a high probability of being signal then the weight assigned to the event is high, the weight given is low in the opposite situation.
The probability of measuring an event with a value in the range x_i to $x_i + \Delta x_i$ for event shape variable X_i is given by equation 5.8, where $n_i(x_i)$ is the number of events with value x_i, N_{total} is a constant normalizing factor and $R_i(x_i)$ is given by equation 5.9.

$$P(X_i = x_i) = \frac{n_i(x_i)_{signal} + n_i(x_i)_{background}}{\int_{-\infty}^{+\infty}(n_i(x_i)_{signal} + n_i(x_i)_{background})dx_i} = \frac{(1 + R_i(x_i))n_i(x_i)_{background}}{N_{total}} \tag{5.8}$$

$$R_i(x_i) = Kr_i(x_i) = \frac{n_i(x_i)_{signal}}{n_i(x_i)_{background}} \tag{5.9}$$

In equation 5.9, $r_i(x_i)$ represents the ratio between the normalized number of signal and background events with value x_i, K is a constant of proportionality representing the ratio between the actual number of signal and background events after the photon selection procedure.

The probability of measuring a value in the range $x_i + \Delta x_i$ given that the event is a signal event is just the normalized number of events present in a histogram of the signal distribution for that particular event shape variable. As the probability of measuring a signal event is a constant, then using equations 5.7, 5.8 and 5.9 the following equation of proportionality can be established,

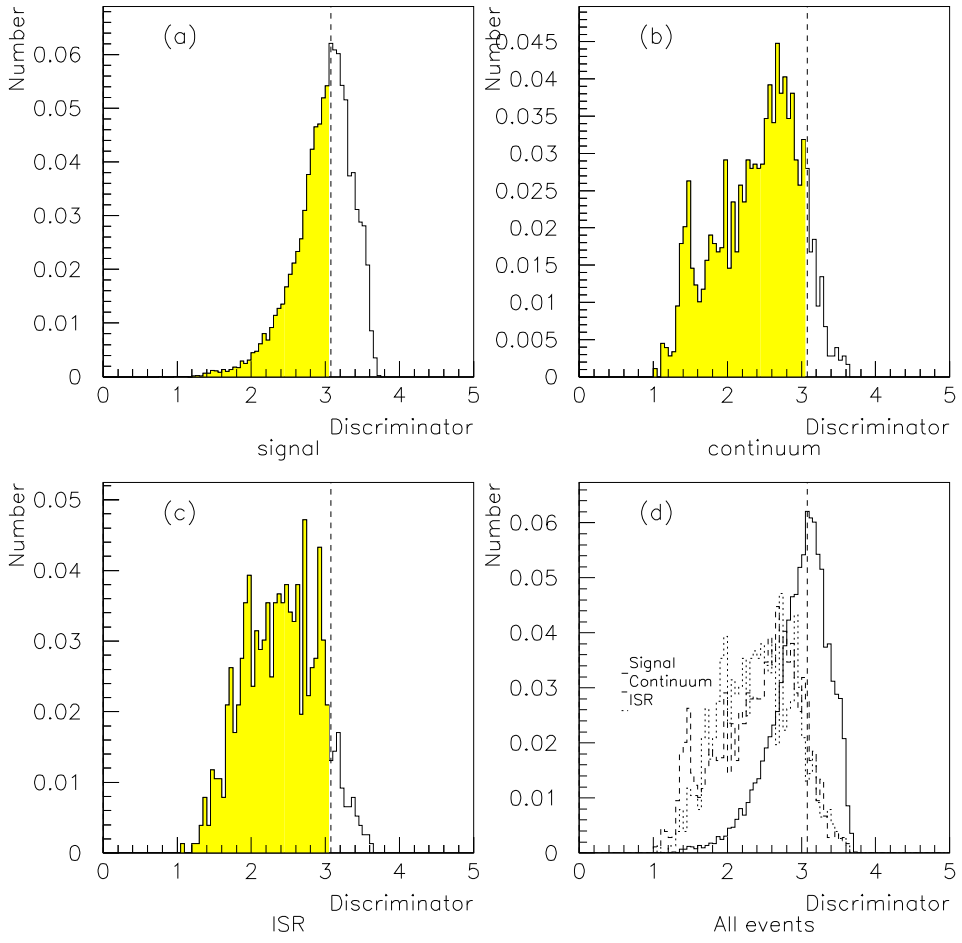

Figure 5.16: Distributions of the combined discriminator for (a) signal (b) generic continuum (c) ISR (d) signal and background events.

$$P(signal|X_i = x_i) \propto \frac{r_i(x_i)}{\alpha + r_i(x_i)} = w_i(x_i) \tag{5.10}$$

where α is equal to $\frac{1}{K}$. This is the point at where the analogy with probabilities breaks down, as α is not known it is set to one. I experimented with various other values for α but found that the weights behaved better using this value. Figure 5.15.(c) plots the weights generated as a function of the event shape variable for the 45^o cone.

The weights associated with each event shape variable are then averaged to form the final combined discriminating variable, given by equation 5.11.

$$D(X_i = x_i) = \sum_i w_i = \sum_i \frac{r_i(x_i)}{1 + r_i(x_i)} \tag{5.11}$$

The distribution of values for the combined discriminating variable for each event

	No. candidates before cut.	No. candidates after cut.	Efficiency.
Signal	22293	10707	0.48
Generic continuum	1787	183	0.11
ISR	763	68	0.89×10^{-1}
Total Background	2550	261	0.10

Table 5.7: Efficiency for combined discriminator analysis.

is plotted in figure 5.16 for (a) signal events, (b) generic Continuum events and (c) ISR events. A single cut was then made to this distribution, the efficiencies are listed in table 5.7.

5.4 Summary.

In this chapter I have shown different techniques that could be applied in an actual $b \to s\gamma$ measurement to reduced the continuum backgrounds. Table 5.8 compares the efficiencies of the different analyses attempted.

The efficiency ratio, which is just the evaluation of 5.3 gives a ranking for the discriminating power of each analysis. The Reconstruction analysis and Combined discriminator analysis include the photon selection efficiencies. From the results it can be seen that the reconstruction analysis provides little benefit over photon selection alone, without further continuum discrimination. However, the combined discriminator analysis does provide significant benefits.

Analysis Type.	Signal efficiency.	Continuum efficiency.	Efficiency ratio.
Photon selection only	0.56	0.13×10^{-1}	5.0
Reconstruction analysis	0.34	0.42×10^{-2}	5.2
Combined discriminator analysis	0.26	0.11×10^{-2}	7.9

Table 5.8: Summary of efficiencies for analyses.

The following calculation, assuming $1fb^{-1}$ of data, gives an idea of the amount of data necessary to perform an actual measurement using the combined discriminator method.

The cross section of $b\overline{b}$ events is $1.05nb$, therefore a total of $1 \times 10^{15} \times 1.05 \times 10^{-9} = 1.05 \times 10^{6}$ $b\overline{b}$ events are produced per fb^{-1}.

Assuming a branching ratio of $\sim 3.0 \times 10^{-4}$ for inclusive $b \to s\gamma$ processes, one would expect approximately 630 inclusive $b \to s\gamma$ events. This includes a factor of 2, which is due to there being two B mesons produced in each $b\overline{b}$ event.

Finally the photon selection and combined discriminator cuts are applied, reducing the number of events to, $0.26 \times 630 = 164$ events.

The cross section for u, d, s, c events at the $\Upsilon(4s)$ resonance is $3.39nb$ from which we can estimate that $1fb^{-1}$ would contain a total of $1 \times 10^{15} \times 3.39 \times 10^{-9} = 3.39 \times 10^{6}$ of continuum events.

After applying the photon selection and combined discriminator cuts the number of events remaining would be $3.39 \times 10^{6} \times 0.11 \times 10^{-2} = 3729$.

Clearly the number of continuum events far exceeds the number of signal events. However using 5.12 we can see that the significance level is $\sim$2.6 σ. With 10 fb^{-1} of data the significance level would be as much as 8.1 σ.

$$significance\ level = \frac{signal}{\sqrt{signal + background}} \tag{5.12}$$

In practice making an actual measurement would also involve the use of a comparable amount of off-resonance data, which allows for the systematic error from the cut efficiencies on continuum events to be dealt with. Using off-resonance data also has the advantage that it removes the systematic error arising from the issue of the reliabilty of Monte-Carlo data.

Conclusions

This brings to a conclusion a body of work which has been undertaken during the development, construction and initial data-taking phase of the BaBar detector. In summary, this thesis has demonstrated, using a Monte-Carlo study, the feasability of making a measurement of the FCNC $b \to s\gamma$, outlining techniques that could be employed in such a measurement. This thesis has also given a detailed description of the EMC FEEs and shown that the electronics can be calibrated to achieve the desired resolution for B Physics studies.

EMC Electronics Calibration.

In the EMC electronics calibration I have shown that the non-linearities in the response of the FEEs channels can be corrected using a 16 parameter fit such that, the contribution from the electronics to the overall EMC resolution is negligible compared to the intrinsic resolution of the CsI crystals. Figure 5.17 compares the energy resolution of a typical electronics channel to the CsI resolution.

Photon Selection.

The photon selection procedure was undertaken as a method of distinguishing signal $b \to s\gamma$ events from background events. This method successfully reduces the number of background events in comparison to the number of signal events, showing itself to be a valid techinque for a $b \to s\gamma$ measurement. Table 5.9 shows the number of signal and background Monte-Carlo events, scaled to represent 1 fb^{-1} of data at the Υ(4s), before and after the photon selection is performed. Where continuum events clearly represent the majority of the background.

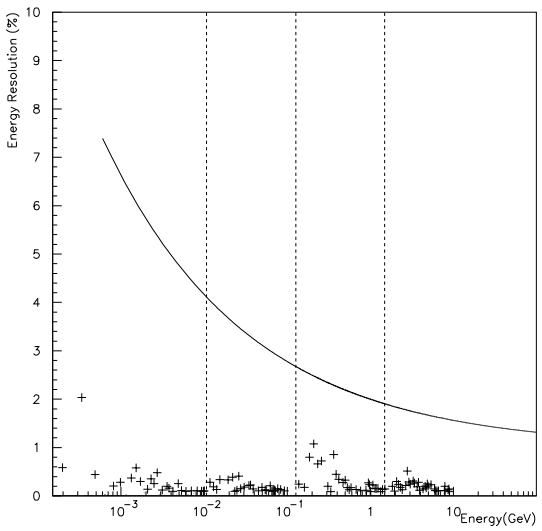

Figure 5.17: Energy resolution contribution from residual non-linearites compared to CsI resolution.

	No. candidates before (fb^{-1}).	No. candidates after (fb^{-1}).
Total signal	630	359
$b\bar{b}$ background	1.05×10^6	252
Total continuum background	3.39×10^6	4.4×10^4

Table 5.9: Approximate number of events per fb^{-1} before and after photon selection.

Figure 5.18 shows the generic background and signal scaled to the proportions produced per 1 fb^{-1} of data at the Υ(4s) (a) before the photon selection procedure and (b) after.

Continuum background suppression.

Further reduction of the continuum background was investigated using two separate methods. A partial reconstruction method that attempts to reconstruct a signal B candidate and a method that characterizes each event with event shape variables combined to form a single discriminating variable. Table 5.10 contrasts the discriminating power of each method combined with the photon selection procedure and the photon selection procedure performed alone.

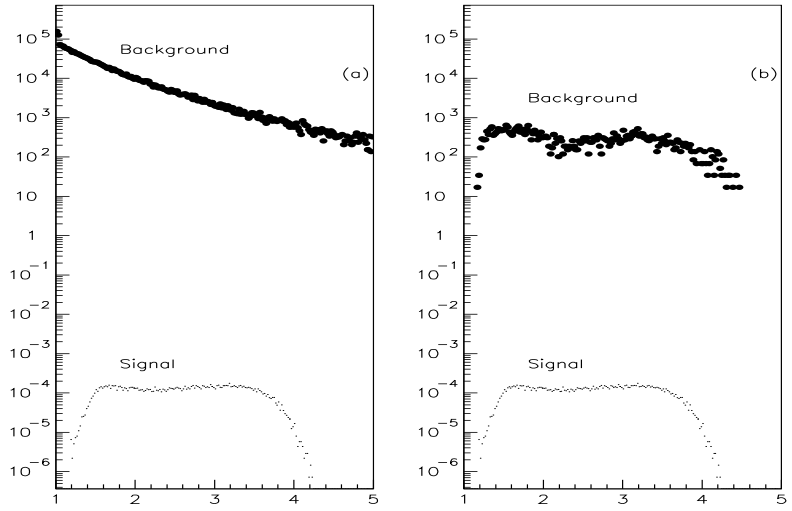

Figure 5.18: Signal and total background per fb^{-1} (a) before and (b) after photon selection procedure.

Analysis type.	Signal efficiency.	Continuum efficiency.	Efficiency ratio.
Photon selection only	0.56	0.13×10^{-1}	5.0
Reconstruction analysis	0.34	0.42×10^{-2}	5.2
Combined discriminator	0.26	0.11×10^{-2}	7.9

Table 5.10: Summary of efficiencies for analyses.

The discriminator method combined with the photon selection procedure proved to be the most powerful of the methods investigated. Table 5.4 shows the number of event before and after the technique is applied, for 1 fb^{-1} at the Υ(4s). Using the maximim number of $b\overline{b}$ Monte-Carlo events that were avaliable for performing this analysis, no $b\overline{b}$ events remained after the applications of these cuts, demonstrating that the continuum background is overwhelmingly the major source of background in this channel.

From the table it is evident that even after the data cuts are applied, the continuum background still dwarves the number of signal $b \to s\gamma$ events. However with 10 fb^{-1}

	No. candidates before (fb^{-1}).	No. candidates after (fb^{-1}).
Total signal	630	164
$b\bar{b}$ background	1.05×10^6	0
Total continuum background	3.39×10^6	3729

Table 5.11: Approximate number of events per fb^{-1} before and after combined discriminator analysis.

of data taken on the Υ(4s) the significance level would be as much as 8.1 σ.

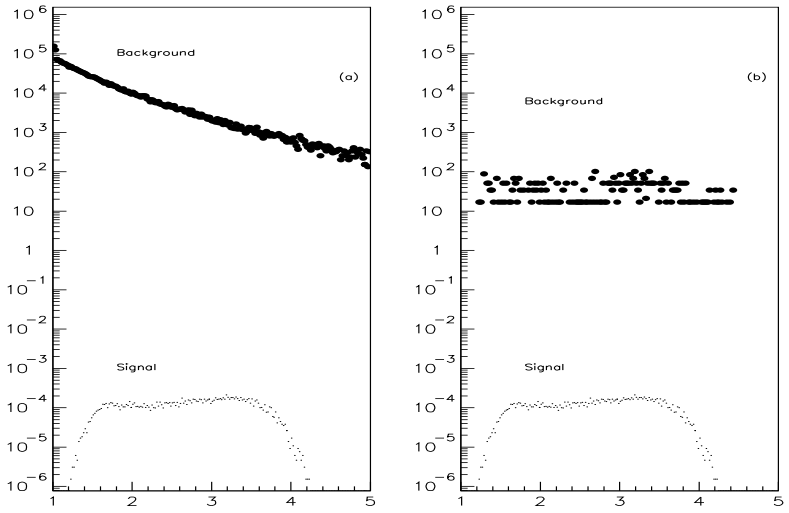

Figure 5.19: Signal and total background per fb^{-1} (a) before and (b) after discriminator method.

Figure 5.19 shows the generic background and signal scaled to the proportions produced per 1 fb^{-1} at the Υ(4s) (a) before the discrimnator and photon selections is applied and (b) after.

Looking to the future.

BaBar and in particular the EMC Calorimeter has now been in operation for almost two years and has already proved successfull with some recent new results, including a measurement of the CP violation parameter $sin(2\beta)$ [23]. A complete measurement

of inclusive $b \to s\gamma$ has still not yet been made at BaBar, however a recent paper has been published [24], that describes an initial study using the sum of exclusive $b \to s\gamma$ modes. All indications are that BaBar will continue producing exciting new results in the near future.

References

[1] F. Halzen and A. D. Martin, "Quarks and Leptons: An Introductory Course in Modern Particle Physics", ISBN 0-471-88741-2 (1984)

[2] C. S. Wu et al, "Experimental Test of Parity Conservation in Beta Decay", Phys. Rev. 105, 1413-1415(L) (1957).

[3] "BaBar Physics Book: Physics at an Asymmetric B factory." SLAC-R-0504, 1998.

[4] G. F. Giudice, "Beyond the Standard Model", hep-ph/9605390, Lectures delivered at the 1995 European School of High-Energy Physics in Dubna, Russia. (1995)

[5] T. Ferbel, "Techniques and concepts of high energy physics X" Proceedings of the Nato Advanced Study Institute on Techniques and Concepts of High Energy Physics 1998, Kluwer Academic, c1999.

[6] S. P. Martin, "A Supersymmetry Primer", hep-ph/9709356.

[7] J. L. Hewitt, "Top Ten Models Constrained by $b \to s\gamma$", hep-ph/9406302, (1994).

[8] T. Cheng, L. Li, "Gauge Theory of Elementary Particle Physics", Oxford Science Publications, ISBN 0-19-851961-3 (1996).

[9] M. Le Bellac, "Quantum and Statistical Field Theory", Oxford Science Publications, ISBN 0-19-853964-9 (1991).

[10] A.Ali & C.Greub, Phys. Lett. B 361, 146 (1995)

[11] A. Ali et al., "Radiative rare B-decays into higher K-resonaces", Phys. Lett. B298, 195 (1993).

[12] Y. Nir, Lectures presented in the 20th SLAC Summer Institute, SLAC-PUB-5874 (1992); Y. Nir and H. R. Quinn, Ann. Rev. Nucl. Part. Sci. 42, 211 (1992).

[13] "Letter of Intent for the Study of CP Violation and Heavy Flavour Physics at PEP-II", SLAC-443 (1994)

[14] BaBar Collaboration, B. Aubert et al., "The BaBar detector", hep-ex/0105044, submitted to Nucl. Instrum. and Methods. (2001)

[15] CLEO Collaboration, S. Ahmed et al., "$b \to s\gamma$ Branching Fraction and CP Asymmetry", hep-ex/9908022, CLEO CONF 99-10. (2000)

[16] ALEPH Collaboration, R. Barate et al., "A measurement of the inclusive $b \to s\gamma$ branching ratio", Phys. Lett. B429, 169 (1998)

[17] R.T.Hamiltion, M.E.Huffer, J.L.White, "The dataflow platform users guide", BaBar Note 385.

[18] BaBar DAQ Group, G. Haller et al., "Electronics Control and Dataflow between the Read-Out Module and the Front-End Electronics Systems", BaBar Note 281.

[19] CLEO Collaboration, S. Ahmed et al., "Search for $\overline{B}^0 \to D^{*0}\gamma$", hex-ex/0001002, CLEO CONF 99-10. (2000)

[20] BaBar Collaboration, B. Aubert et al., "Measurement of Branching Fractions and CP-Violating Asymmetries in Charmless Two-Body Decays into Pions and Kaons.", BABAR-PUB-01/10. (2001)

[21] Particle Data Group, "Review of Particle Physics", Phys. Rev. 12 (2000).

[22] G. Fox and S. Wolfram, Phys. Rev. Lett. 41, 1581 (1978).

[23] BaBar Collaboration, B. Aubert et al., "Measurement of CP-Violating Asymmetries in B^0 decays to CP Eigenstates.", hep-ex/0102030 SLAC-PUB-8777 (2001).

[24] BaBar Collaboration, B. Aubert et al., "Study of $b \to s\gamma$ using the sum of exclusive modes", Submitted to the International Europhysics Conference on High Energy Physics (2001), Budapest, Hungary.

Appendix A: Angular Momentum of K^0's

$K^*(892)$ is the lightest meson produced as K^0's are inaccessible because of conservation of angular momentum. B mesons have $J = 0$, photons have $J = 1$. If B's were point-like objects only K^*'s and K_1's would be produced, however as B mesons have structure, an extra component of orbital angular momentum can be introduced. This intrinsic angular momentum is perpendicular to the plane of motion and dependent on the production separation of the gamma and X_s, see figure 20.

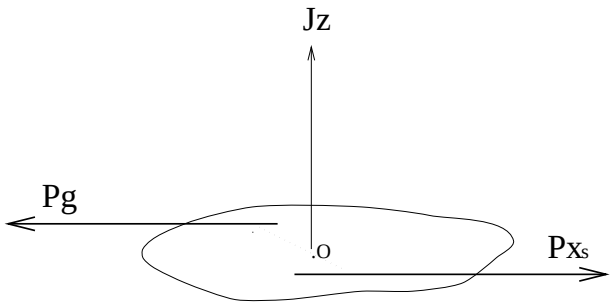

Figure 20: Orbital Angular momentum component due to the B mesons being nonpoint like.

Hence other angular momentum kaon resonanances can be produced. As the photon angular momentum vector is parallel to its momentum vector the momentum vectors form a right angled triangle illustrated in figure 21. The intrinsic angular momentum need to compensate is therefore given by $J = \sqrt{J_{Xs}^2 - 1}$ explaining the fact that $K^*(892)$ is the lightest meson produced in $b \to s\gamma$ as K^0's are inaccessiable as angular momentum can not be conserved.

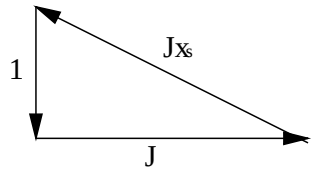

Figure 21: Angular momentum component due to the B mesons being nonpoint like.

Appendix B: Upsilon Resonance Sector.

The Υ resonances are states of the $b\bar{b}$ or bottomunium system. These states are analogous to the positronium states of a bound electron and positron as studied in atomic physics. Infact many of the properties of the bottomonium system can be inferred from the positronium system by exchanging the electron and positron with a heavy quark and anti-quark and replacing the electronic binding to strong interaction binding. The energy level transitions of the bottomonium system are illustrated in figure 22.

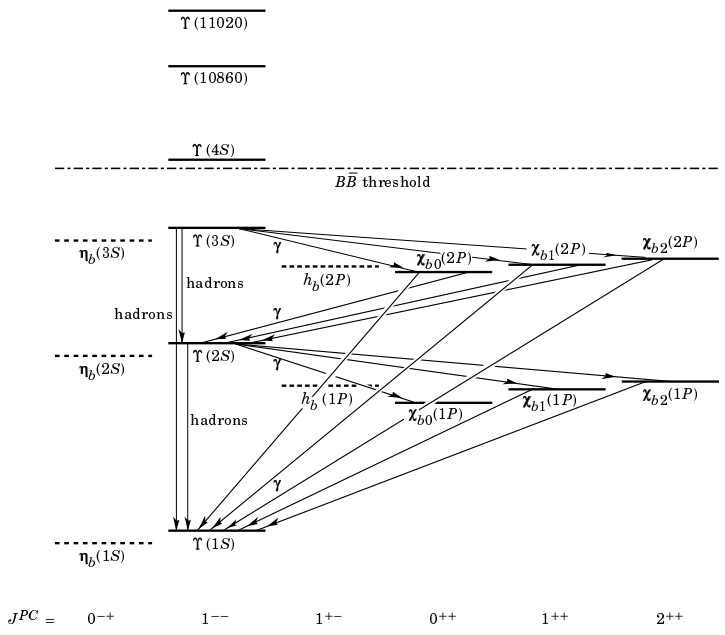

Figure 22: Energy level transitions of the bottomonium system.

The first resonance to be discovered and identified as a bottomonium state was the Υ(1s), the other Υ resonances are radially excited states. The Υ resonance sector is illustrated in figure 23 which shows the e^+e^- cross section at the energies of the Υ resonances. The width of the Υ(4s) resonance is $23.8 \pm 2.2\ MeV$ and is significantly

larger than the widths of the other Υ resonances. The increase in width occurs as the Υ(4s) resonance lies above the threshold for $B\overline{B}$ production. Infact the energy

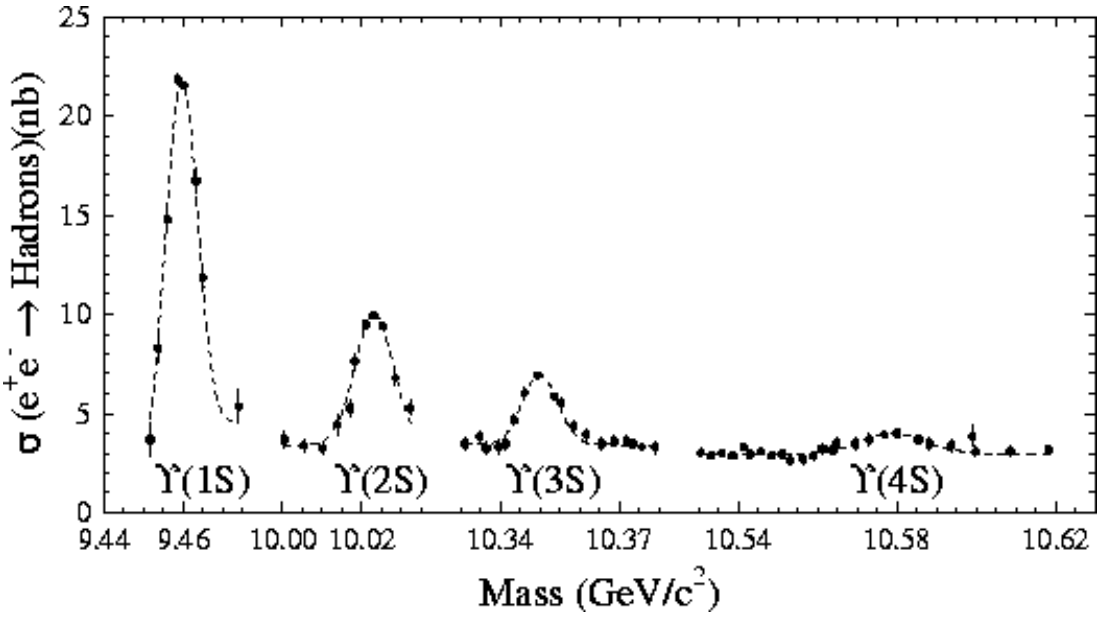

Figure 23: e^+e^- cross section showing the masses of the Υ resonances.

of the Υ(4s) is only 20 MeV above the $B\overline{B}$ production threshold. Consequently there is not sufficient energy for the production of additional particles and the B mesons are produced with very little residual momentum and are almost at rest in the CM system. The $\Upsilon(4s)$ decays to either $B^0\overline{B}^0$ or $B^0\overline{B}^0$ pairs, the heavier B meson states are inaccessible.